



AMERICAN UNIVERSITY OF BEIRUT

CONTROLLED SYNTHESIS AND SIZE DISTRIBUTION  
OF ZEOLITIC IMIDAZOLATE FRAMEWORK CRYSTALS  
VIA THE REACTION-DIFFUSION FRAMEWORK

by  
RITA FRANCIS ZAKHIA DOUAIHY

A thesis  
submitted in partial fulfillment of the requirements  
for the degree of Master of Chemistry  
to the Department of Chemistry  
of the Faculty of Arts and Sciences  
at the American University of Beirut

Beirut, Lebanon  
October 2018

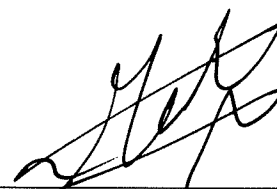
AMERICAN UNIVERSITY OF BEIRUT

CONTROLLED SYNTHESIS AND SIZE DISTRIBUTION  
OF ZEOLITIC IMIDAZOLATE FRAMEWORK CRYSTALS  
VIA THE REACTION-DIFFUSION FRAMEWORK

by  
RITA FRANCIS ZAKHIA DOUAIHY

Approved by:

Dr. Mohamad Hmadeh, Assistant Professor  
Department of Chemistry



Advisor

Dr. Mazen Al Ghoul, Professor  
Department of Chemistry



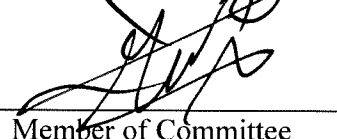
Co-Advisor

Dr. Rabih Sultan, Professor  
Department of Chemistry



Member of Committee

Dr. Pierre Karam, Assistant Professor  
Department of Chemistry



Member of Committee

Date of thesis defense: 29 October 2018

AMERICAN UNIVERSITY OF BEIRUT

THESIS, DISSERTATION, PROJECT RELEASE FORM

Student Name:

ZAKHIA DOUAIHY

Rita

Francis

\_\_\_\_\_  
Last

\_\_\_\_\_  
First

\_\_\_\_\_  
Middle

Master's Thesis

Master's Project

Doctoral Dissertation

I authorize the American University of Beirut to: (a) reproduce hard or electronic copies of my thesis, dissertation, or project; (b) include such copies in the archives and digital repositories of the University; and (c) make freely available such copies to third parties for research or educational purposes.

I authorize the American University of Beirut, to: (a) reproduce hard or electronic copies of it; (b) include such copies in the archives and digital repositories of the University; and (c) make freely available such copies to third parties for research or educational purposes after:

**One --- year from the date of submission of my thesis, dissertation, or project.**

**Two ~~1~~ years from the date of submission of my thesis, dissertation, or project.**

**Three --- years from the date of submission of my thesis, dissertation, or project.**

*Rita Douaihy*  
Signature

*30 October 2018*  
Date

## ACKNOWLEDGMENTS

I take this opportunity to extend my sincere gratitude and appreciation to all those who made this thesis possible. This work would not have been possible without you.

First, I would like to express my deepest gratitude to my advisor Dr. Mohamad Hmadeh and co-advisor Dr. Mazen Al-Ghoul for providing their heartfelt support and guidance at all times. Thank you for giving me invaluable guidance, inspiration and suggestions in my quest for knowledge.

I would like to thank the committee members Dr. Rabih Sultan and Dr. Pierre Karam for their helpful discussions, pertinent notes, comments, and appreciable feedback.

I would like also to extend my thankful acknowledgments to Dr. Mohamad El Roz for offering the opportunity of an internship in his research group at the LCS laboratory in France.

I appreciate and acknowledge the immense technical assistance of the Central Research Science Laboratory (CRSL) members and the staff at the chemistry department at AUB.

I am particularly grateful to Miss Manal Ammar for her assistance and to all my lab colleagues for their fruitful cooperation and interaction.

To my friends at AUB, and at the LCS lab, thank you for your constant encouragement and continuous support. Thank you for the amazing time we spent together and for the memories we have made.

A special word of thanks for my friends who have always been a major source of support when things would get a bit discouraging: Samar, Hamsa, Eliane, Alaa and Christiane. Thank you guys for always being there for me.

I am extremely indebted to my family whose infallible love, care and support has always been my strength. Without their help and faith, I would not have been able to complete much of what I have done.

# AN ABSTRACT OF THE THESIS OF

Rita Francis Zakhia Douaihy for Master of Science  
Major: Chemistry

Title: Controlled Synthesis and Size Distribution of Zeolitic Imidazolate Framework Crystals via the Reaction-Diffusion Framework

Zeolitic imidazolate frameworks (ZIFs), a subclass of metal-organic frameworks (MOFs), have been recently employed in various fields such as gas separation, catalysis, water purification and drug delivery. Their high importance is due to their chemical and thermal stability in addition to the flexibility of their design. Several routes of synthesis were employed to produce these materials. In this thesis, we investigate a new synthesis method where ZIF crystals are produced using the reaction-diffusion framework (RDF) in a hydrogel medium at room temperature. The method is based on the diffusion of an outer solution of the organic linker or mixed linkers into an agar gel containing the inner metal ions Zn (II) where a precipitation reaction takes place leading to the formation of the ZIF crystals. Remarkably, the nonlinear coupling between reaction and diffusion with the nucleation and growth of the crystals results for many ZIF systems in the formation of Liesegang bands with direct spacing. This banding can be further exploited to control the crystal size distribution of the ZIFs along the tubular reactor. The ZIF-8 and ZIF-7 particles are then collected and fully characterized using powder x-ray diffraction (PXRD), scanning electron microscopy (SEM), thermogravimetric analysis (TGA) and Brunauer-Emmett-Teller (BET) analysis. Moreover, the scaling laws of these specific Liesegang system are determined, and their effect on the crystal size distribution is studied. The effect of different parameters such as the concentrations of the reactants, the gel thickness, and the temperature is investigated. Furthermore, cobalt-doped ZIF-8 ( $\text{Co}_x\text{Zn}_{1-x}(\text{HmIm})_2$ , HmIm = 2-methylimidazole) is successfully synthesized using the same framework starting with an initial ionic mixture of Zn (II) and Co (II) in the gel at a fixed composition and HmIm as the outer linker. This system also exhibits periodic precipitation concomitant with variable cobalt-doping percentages among the Liesegang bands.

ACKNOWLEDGEMENTS.....	v
ABSTRACT.....	vi
LIST OF ILLUSTRATIONS.....	xii
LIST OF TABLES.....	xiii
 Chapter	
I. INTRODUCTION.....	1
A. Zeolitic imidazolate frameworks (ZIFs).....	1
1. Historical Background.....	1
2. Synthesis techniques of ZIFs.....	5
a. Solvothermal Synthesis .....	5
b. Hydrothermal Synthesis.....	6
c. Sonochemical Synthesis.....	6
d. Mechanochemical Synthesis.....	7
e. Dry-Gel Conversion (DGC) .....	7
f. Ionothermal Synthesis.....	8
g. Microfluidic Synthesis.....	8
3. Applications of ZIFs.....	9
a. Gas Separation .....	9
b. Adsorption.....	10
c. ZIFs as catalysts.....	11
d. ZIFs in sensing and electrical devices .....	12
e. ZIFs in drug delivery.....	13
B. Reaction-diffusion Framework.....	14
1. Historical Background.....	14
2. Theories governing the Liesegang Banding Phenomenon.....	17
a. Pre-Nucleation Theory .....	17
b. Post-Nucleation Theory.....	19
3. Spacing laws of the Liesegang Banding Phenomenon.....	19
a. The Spacing Law.....	20
b. The Width Law.....	20

c. The Matalon-Packter Law.....	21
C. Aim of the work .....	21
<b>II. MATERIALS AND METHODS</b> .....	<b>23</b>
A. Materials.....	23
B. Preparation of ZIF Crystals.....	23
1. Preparation of ZIF-8.....	23
2. Preparation of ZIF-67.....	24
3. Preparation of Co-doped ZIF-8 and Zn-doped ZIF-67.....	25
4. Preparation of ZIF-7.....	26
C. Characterization of ZIF-8, ZIF-67 and ZIF-7 crystals.....	27
1. Powder X-ray Diffraction (PXRD).....	27
2. Scanning Electron Microscopy Analysis (SEM).....	28
3. Thermogravimetric Analysis (TGA).....	28
4. Nitrogen Adsorption and BET calculations.....	28
5. Atomic Absorption (AA).....	28
<b>III. SYNTHESIS AND CHARACTERIZATION OF ZIF-8, ZIF-67 AND THEIR MIXED METALS DERIVATIVES VIA A REACTION-DIFFUSION FRAMEWORK</b> .....	<b>30</b>
A. Introduction.....	30
B. Results and discussion.....	32
1. Powder X-ray Diffraction of ZIF-8 Crystals.....	32
2. Scanning Electron Microscopy Analysis and Particle Size Distribution of ZIF-8 Crystals.....	33
3. BET surface area of ZIF-8 Crystals.....	35
4. Thermal Stability of ZIF-8 Crystals .....	35
5. Yield of ZIF-8 Crystals.....	36
6. Kinetic study of the particle size evolution.....	37
7. Liesegang Laws.....	39



a. Spacing Law .....	39
b. Width Law.....	40
c. Matalon-Packter Law .....	42
8. Size and Morphology of ZIF-8 Crystals.....	43
a. Effect of inner concentration [ $\text{Zn}^{2+}$ ].....	43
b. Effect of outer concentration [ $\text{HmIm}$ ].....	43
c. Effect of agar percentage .....	44
d. Effect of temperature.....	45
9. Characterization of ZIF-67.....	47
10. Mixture of the Two Metal Ions $\text{Zn}^{2+}$ and $\text{Co}^{2+}$ .....	48
<b>IV. SYNTHESIS AND CHARACTERIZATION OF ZIF-7</b>	<b>53</b>
A. Introduction.....	53
B. Results and discussion.....	54
1. Powder X-ray Diffraction of ZIF-8 Crystals.....	54
2. Scanning Electron Microscopy Analysis and Particle Size Distribution of ZIF-7 Crystals.....	55
3. BET surface area of ZIF-7 Crystals.....	57
4. Thermal Stability of ZIF-7 Crystals .....	57
5. Yield of ZIF-7 Crystals.....	58
6. Effect of the Zinc Source and Solvent.....	58
7. Kinetic study of the particle size evolution.....	59
8. Liesegang Laws.....	60
a. Spacing Law .....	61
b. Width Law.....	62
c. Matalon-Packter Law .....	63
9. Size and Morphology of ZIF-8 Crystals.....	64
a. Effect of inner concentration [ $\text{Zn}^{2+}$ ].....	64
b. Effect of outer concentration [ $\text{HmIm}$ ].....	65
c. Effect of agar percentage .....	66
d. Effect of temperature.....	67

10. Size Law.....	68
<b>V. CONCLUSION AND FUTURE WORK.....</b>	<b>72</b>
A. Conclusion.....	72
B. Future Work.....	74
 Appendix	
Tables.....	76
 <b>REFERENCES.....</b>	<b>85</b>

# ILLUSTRATIONS

Figure	Page
1.	Different lattice structures (middle) with their inorganic SBUs (left) and the organic linkers (right) used in the synthesis of different Metal-Organic frameworks. Reprinted with the permission of ref [9]. Published by Science. .... 2
2.	Crystal structure of various topologies of Zeolitic Imidazolate frameworks (ZIFs). The blue and the pink tetrahedra correspond to the metal ion whereas the yellow spheres are attributed to the space in the cage. Reprinted with permission from ref.[11]. Copyright 2009 American Chemical Society. .... 3
3	.Chemical structure of different organic linkers used in the synthesis of ZIFs Reprinted with permission from ref.[11]. Copyright 2009 American Chemical Society. .... 4
4.	Examples of animate (a-d) and inanimate (e-h) RDF systems at different length scales ( $\mu\text{m}$ , nm and m) . Reprinted with permission from ref. [106]. Copyright 2009 John Wiley and Sons. .... 15
5.	Classic Liesegang rings formed in a silver dichromate system in gelatin Reprinted with permission from ref. [106]. Copyright 2009 John Wiley and Sons..... 16
6.	Computational simulation of the concentrations of a and b, and the ion-product concentration $ab$ in the supersaturation theory of the Liesegang banding. $q^*$ represents the precipitation threshold, $x_n$ the position of the $n^{\text{th}}$ band. Reprinted with permission from ref. [122]. Copyright 2005 Institute for Scientific Information. .... 18
7.	Schematic representation of ZIF-8 synthesis via RDF. .... 24
8.	Schematic representation of ZIF-67 synthesis via RDF. .... 25
9.	Schematic representation of 5% Co-doped ZIF-8 (A) and 5 % Zn-doped ZIF-67 (B) via RDF. .... 26
10.	Schematic representation of ZIF-7 synthesis via RDF. .... 27
11.	(A) The crystal structure of ZIF-8. The blue tetrahedra are formed of Zinc ions, the black spheres represent the carbon atoms and the green spheres represent the nitrogen atoms and (B) the SOD topology. Reprinted with the permission of ref [9]. Copyright 2006, Proceedings of the National Academy of Sciences. .... 30
12.	Crystal structure of Co-doped ZIF-8, Zn: blue, Co: purple, N: green and C: black..... 31
13.	PXRD patterns of the simulated ZIF-8 crystals and the synthesized ZIF-8 via RDF..... 32
14.	(A) SEM images showing polyhedral ZIF-8 particles synthesized via RDF and their size distribution in $\mu\text{m}$ (histograms inset). The scale bar is $2 \mu\text{m}$ and (B) a graph of the particle size growth over 6 consecutive bands. The bands are collected as adjacent regions of 0.5 cm each. .... 34
15.	$\text{N}_2$ adsorption and desorption isotherms of ZIF-8 at 77 K..... 35

16.	Thermogravimetric curve of ZIF-8 under nitrogen atmosphere with a heating rate of 5 °C. min <sup>-1</sup> and a temperature between 30 °C and 1100 °C. ....	36
17.	Preparation of ZIF-8 using the RDF process at different scales in larger volumes. ....	37
18.	PXRD patterns of the simulated ZIF-8 crystals and the synthesized ZIF-8 via RDF after 1 min of diffusion. ....	38
19.	SEM images showing the kinetics of growth of ZIF-8 at different times: (A) 1 minute, (B) 2 minutes, (C) 3 minutes and (D) 5 minutes with zoomed in (inset) image showing the morphologies . The scale bar is 2 μm. ....	38
20.	Plot of the band position $x_n$ versus its number $n$ displaying direct spacing in the ZIF-8 precipitation system at (A) different inner concentrations and (B) different outer concentrations. ....	40
21.	The width $w_n$ of the consecutive bands plotted versus its number $n$ in the ZIF-8 precipitation system at (A) different inner concentrations and (B) different outer concentrations. ....	41
22.	Particle size of ZIF-8 crystals at different inner [Zn <sup>2+</sup> ]. ....	43
23.	Particle size of ZIF-8 crystals at different outer [HmIm]. ....	44
24.	Particle size of ZIF-8 crystals at different agar percentages. ....	45
25.	Particle size of ZIF-8 crystals at different temperatures. ....	46
26.	PXRD patterns of the simulated ZIF-67 and the synthesized one (part 1 and 2) . ....	47
27.	SEM images of ZIF-67 prepared at [Co <sup>2+</sup> ] = 20 mM as an inner solution, [HmIm] = 1 M as an outer solution and 1 % agar gel at 25 ° C. (1) part 1 and (2) part 2. The scale bar is 5 μm. ....	48
28.	PXRD patterns of the simulated ZIF-8 and the 5 % Co-doped ZIF-8. ....	48
29.	PXRD patterns of the simulated ZIF-67 and the 5 % Zn-doped ZIF-67. ....	49
30.	SEM image of 5 % Co doped ZIF-8 prepared at [Zn <sup>2+</sup> /Co <sup>2+</sup> ] = 20 mM as an inner solution, [HmIm] = 1 M as an outer solution and 1 % agar gel at 25 °C. The scale bar is 2 μm. ....	49
31.	SEM images of 5 consecutive bands of the 5 % Zn-doped ZIF-67 prepared at [Zn <sup>2+</sup> /Co <sup>2+</sup> ] = 20 mM as an inner solution, [HmIm] = 1 M as an outer solution and 1 % agar gel at 25 °C. The scale bar is 1 μm. ....	50
32.	N <sub>2</sub> adsorption and desorption isotherm of 5 % Co doped ZIF-8 at 77 K. ....	51
33.	Atomic percentage of cobalt incorporation in ZIF-8 particles measured via AA for different initial ratios of Co <sup>2+</sup> in 5 consecutive bands of the tubes. ....	52
34.	(A) The crystal structure of ZIF-7. The blue tetrahedra represents the ZnN <sub>4</sub> tetrahedra and the yellow sphere represents the space in the ZIF-7 cage (B) with the two structures predicted by the molecular dynamics showing the narrow-pore phase and (C) the large-pore phase . Reprinted with the permission of ref [138]. Copyright 2015 American Chemical Society and with permission of ref [137]. Copyright 2016 Processes. ....	54
35.	PXRD of the simulated ZIF-7 crystals and the synthesized ZIF-7 particles via RDF. ....	55
36.	(A) SEM images showing ZIF-7 particles synthesized via RDF (the scale bar is 2 μm) and (B) a graph of the particle size growth over 5 consecutive bands. ....	56
37.	Thermogravimetric curves of ZIF-7 under nitrogen atmosphere with a heating rate of 5 °C. min <sup>-1</sup> and a temperature between 30 °C and 1100 °C. ....	57

38.	Preparation of ZIF-7 using the RDF process at different scales in larger volumes.....	58
39.	Synthesis of ZIF-7 using different zinc sources (A) nitrate in water, (B) nitrate in water and DMF, (C) chloride in water, (D) chloride in water and DMF, (E) bromide in water, (F) bromide in water and DMF. ....	59
40.	PXRD pattern of ZIF-7 particles at 1 min after the diffusion of the outer electrolyte.....	60
41.	SEM images showing the kinetic of growth of ZIF-7 at different times: (A)1 minute, (B) 3 minutes and (C) 5 minutes with a zoomed in figure of the spheres (in set) .The scale bas is 1 $\mu\text{m}$ .....	60
42.	The position $x_n$ of the consecutive bands plotted versus their number n showing the direct spacing in the ZIF-7 precipitation system for (A) for different $[\text{Zn}^{2+}]$ and (B) different outer $[\text{BenzIm}]$ . ....	62
43.	The width $w_n$ of the consecutive bands plotted versus their number n showing the direct spacing in the ZIF-7 precipitation system (A) for different $[\text{Zn}^{2+}]$ and (B) different outer $[\text{BenzIm}]$ . ....	63
44.	Particle size of ZIF-7 crystals at different inner $[\text{Zn}^{2+}]$ . ....	65
45.	Particle size of ZIF-7 crystals at different outer $[\text{BenzIm}]$ . ....	66
46.	Particle size of ZIF-7 crystals at different agar percentages.....	67
47.	Particle size of ZIF-7 crystals at different temperatures. ....	68
48.	Particle size ( $\mu\text{m}$ ) versus the position of the bands $x_n$ for different inner $[\text{Zn}^{2+}]$ . ....	69
49.	Particle size ( $\mu\text{m}$ ) versus the position of the bands $x_n$ for different outer $[\text{BenzIm}]$ . ....	70
50.	The evolution of the of $\text{CO}_2$ concentration (ppm) versus irradiation time during the photocatalytic decomposition of FAc on ZIF-8, 20 % Co-doped ZIF-8 and ZIF-8 and 20 % Co-doped ZIF-8 as catalyst support for Pt . ....	74
51.	Bar graphs showing the concentrations of $\text{CO}_2$ , $\text{H}_2$ and CO (in ppm) for different samples used. ....	75
S1.	SEM images of the synthesized ZIF-7 particles using different zinc sources ((A): zinc nitrate in water, (B): zinc nitrate in a 1:1 ratio of DMF and water, (C): zinc chloride in water, (D): zinc chloride in a 1:1 ratio of DMF and water, (E): zinc bromide in water and (F): zinc bromide in a 1:1 ratio of DMF and water). ....	80
S2.	PXRD patterns of the synthesized ZIF-7 using different zinc sources.....	80

## TABLES

Table		Page
1.	List of Zeolitic imidazolate frameworks used in the separation of gases from mixtures. ....	10
2.	The spacing coefficient $p$ calculated at different inner ( $[Zn^{2+}]$ ) and outer concentrations ( $[HmIm]$ ) for the ZIF-8 system. ....	39
3.	The width coefficient $q$ calculated at different inner ( $[Zn^{2+}]$ ) and outer concentrations ( $[HmIm]$ ) for the ZIF-8 system. ....	41
4.	The width exponent $\alpha$ for different inner and outer concentrations. ....	41
5.	Values of the functions $G(b_0)$ and $F(b_0)$ for different initial inner concentrations $b_0$ . ....	42
6.	The spacing coefficient $p$ at different inner concentrations ( $[Zn^{2+}]$ ) and different outer concentrations ( $[BenzIm]$ ). ....	61
7.	The width coefficient $q$ at different inner concentrations ( $[Zn^{2+}]$ ) and different outer concentrations ( $[BenzIm]$ ). ....	62
8.	The width exponent $\alpha$ for different inner and outer concentrations. ....	63
9.	Values of the functions $G(b_0)$ and $F(b_0)$ for different initial inner concentrations $b_0$ . ....	64
10.	The exponent $\sigma$ extracted from the slopes of the ln-ln plots of the particle size versus its band position for different inner $[Zn^{2+}]$ . ....	69
11.	The exponent $\sigma$ extracted from the slopes of the ln-ln plots of the particle size versus its band position for different outer $[BenzIm]$ . ....	71
S1.	SEM images showing the growth of ZIF-8 particles at different inner concentrations $[Zn^{2+}]$ and outer $[HmIm] = 1$ M in consecutive bands (1 % Agar, 25°C). The scale bar is 1 $\mu$ m. ....	76
S2.	SEM images showing the growth of ZIF-8 particles at different outer concentrations $[HmIm]$ and inner $[Zn^{2+}] = 20$ mM in consecutive bands (1 % Agar, 25°C). The scale bar is 2 $\mu$ m. ....	77
S3.	SEM images showing the growth of ZIF-8 particles at different agar percentages with constant inner and outer concentrations ( $[Zn^{2+}] = 20$ mM, $[HmIm] = 2$ M) at 25 °C in consecutive bands. The scale bar is 2 $\mu$ m. ....	78
S4.	SEM images showing the growth of ZIF-8 particles at $[Zn^{2+}] = 20$ mM, $[HmIm] = 1.5$ M, at 1 % agar and different temperatures (°C) in consecutive bands. The scale bar is 2 $\mu$ m. ....	79
S5.	SEM images showing the growth of ZIF-7 particles at different inner concentrations $[Zn^{2+}]$ and outer $[BenzIm] = 0.7$ M in consecutive bands (1 % Agar, 25°C). The scale bar is 2 $\mu$ m. ....	81
S6.	SEM images showing the growth of ZIF-7 particles at different outer concentrations $[BenzIm]$ and inner $[Zn^{2+}] = 20$ mM in consecutive bands (1 % Agar, 25°C). The scale bar is 2 $\mu$ m. ....	81

- S7. SEM images showing the growth of ZIF-7 particles at different agar percentages with constant inner and outer concentrations ( $[Zn^{2+}] = 20 \text{ mM}$ ,  $[BenzIm] = 1 \text{ M}$ ) at  $25 \text{ }^\circ\text{C}$  in consecutive bands. The scale bar is  $2 \text{ }\mu\text{m}$  ..... 83
- S8. SEM images showing the growth of ZIF-7 particles at  $[Zn^{2+}] = 20 \text{ mM}$ ,  $[BenzIm] = 1 \text{ M}$ , at 1 % agar and different temperatures ( $^\circ\text{C}$ ) in consecutive bands. The scale bar is  $2 \text{ }\mu\text{m}$ ..... 84

# CHAPTER I

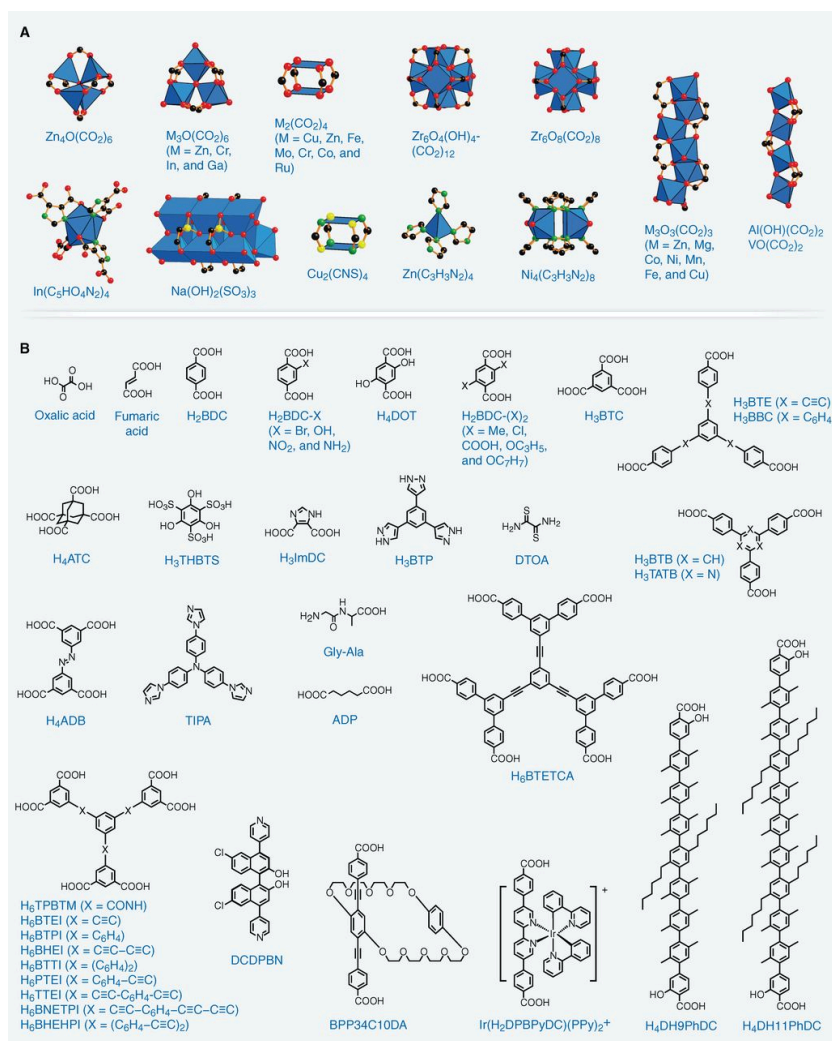
## INTRODUCTION

### A. Zeolitic imidazolate frameworks (ZIFs)

#### 1. *Historical background*

For a long time, porous materials have been applied in different fields due to their intrinsic properties such as high surface areas, large pore volumes and tunable pore sizes [1]. During the last decades, a new class of porous materials has been introduced under the name of metal-organic frameworks (MOFs) by Yaghi *et al.* [2, 3]. MOFs, assembled from metal ions (e.g. zinc, cobalt and copper) and organic linkers (e.g. 1,4-Benzenedicarboxylic acid (BDC), 1,3,5-Benzenetricarboxylic acid (BTC) and 1,3,5-Tris(4-carboxyphenyl)benzene (BTB) , are rapidly developed due to their high versatility [4, 5] which is attributed to the wide range of starting materials (organic linkers and metal ions) from which they can be synthesized. This was achieved by applying the concept of the secondary building units (SBUs) which have well-defined geometries. The wide variety of possible topologies of MOFs are due to the linkage of SBUs (organic and inorganic) of different geometries via strong bonds (Figure 1) [6-9].



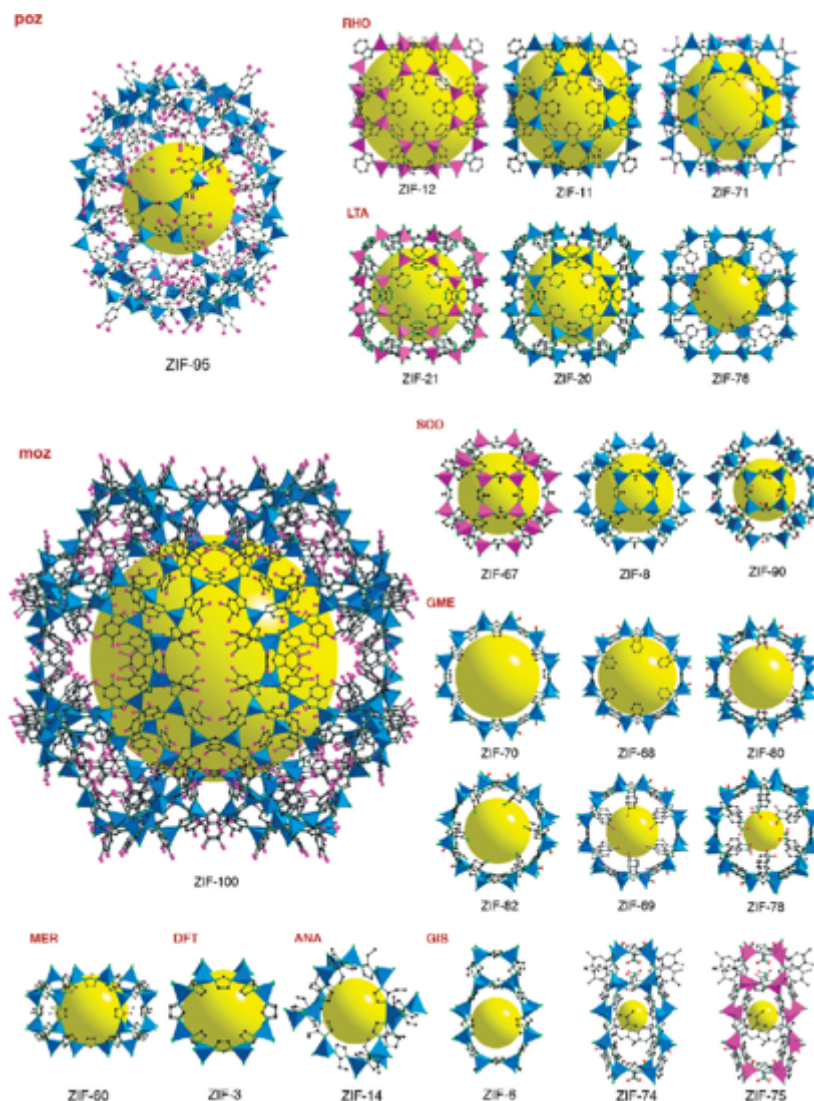


**Figure 1:** Different lattice structures (middle) with their inorganic SBUs (left) and the organic linkers (right) used in the synthesis of different Metal-Organic frameworks. Reprinted with the permission of ref [9]. Published by Science.

Among these hybrid inorganic-organic materials, zeolitic structures were introduced by Yaghi *et al.* as a subclass of MOFs [10-13]. Zeolitic imidazolate frameworks (ZIFs) adopt a similar linkage to that of the aluminosilicate zeolites. The metal centers ( $M^{2+}$ ) are tetrahedrally coordinated to the imidazolate anions forming an angle of  $145^\circ$  similar to the angle between the silicon and oxygen in zeolites [10]. Most of the metal centers are transition metals (e.g. zinc, cobalt and copper) with an empty d orbital receiving an electron from the organic linkers to establish the coordination bond

[14]. ZIFs tend to form new structures, in addition to the traditional zeolite ones [15].

The various representative ZIFs structures are shown in Figure 2 [12].

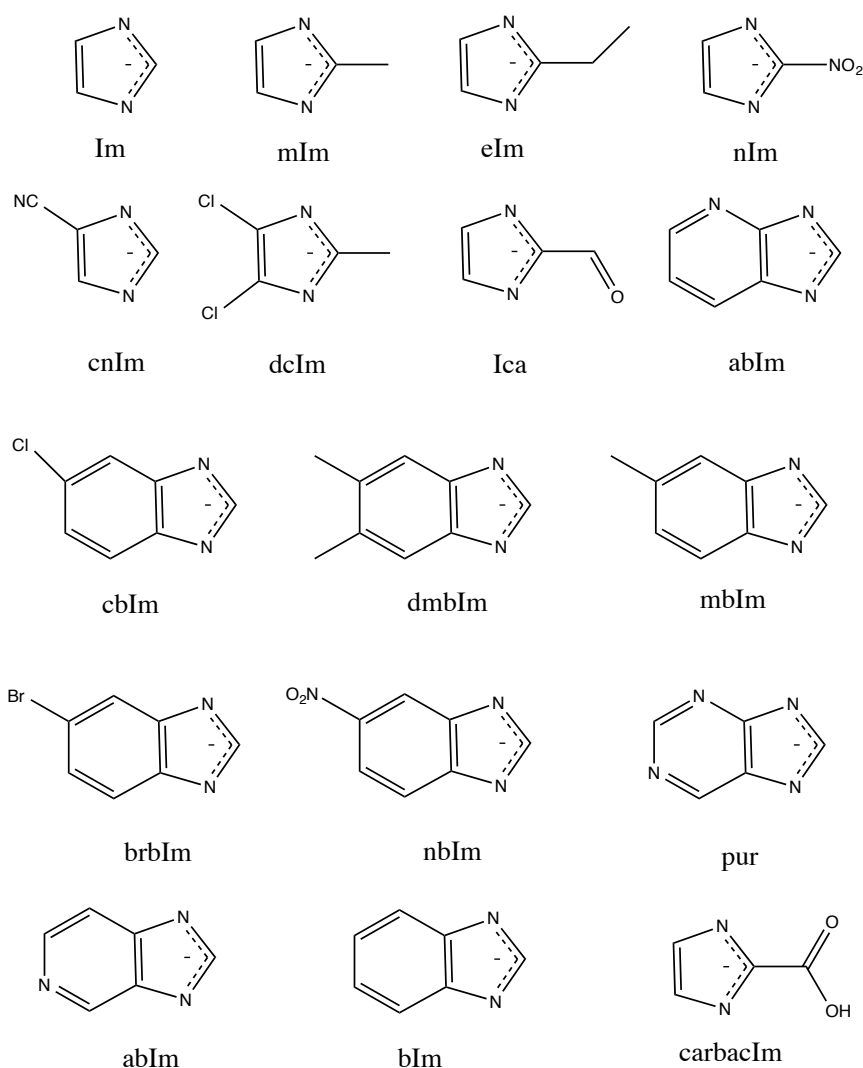


**Figure 2:** Crystal structure of various topologies of Zeolitic Imidazolate frameworks (ZIFs). The blue and the pink tetrahedra correspond to the metal ion whereas the yellow spheres are attributed to the space in the cage. Reprinted with permission from ref.[11]. Copyright 2009 American Chemical Society.

Since ZIFs possess the structural characteristics of both zeolites and MOFs, they display combined advanced properties such as ultra-high surface areas [10], exceptional thermal [10, 16, 17] and chemical [10, 17] stabilities, high crystallinity [10] and abundant functionalities. These properties render ZIFs particles an exceptional use

in different fields including catalysis [16], separation [18], gas storage [19] and drug delivery [20].

Moreover, the importance of ZIFs is not only attributed to their high surface area, but also to the diversity of metal ions and organic linkers that could be used in the synthesis process (Figure 3) [12]. This diversity leads to a wide family of ZIFs having different structures with adapted properties implied in different applications.



**Figure 3:** Chemical structure of different organic linkers used in the synthesis of ZIFs. Reprinted with permission from ref.[11]. Copyright 2009 American Chemical Society.

In some cases, mixed metal ions or mixed organic linkers are incorporated together to form new materials with enhanced properties [21, 22]. A prominent example

of mixed metal system is the Co-doped ZIF-8, where zinc ions are mixed with cobalt ions in the presence of 2-methylimidazole as the organic linker [23]. Recently, it is shown that when doped with cobalt ions, ZIF-8 has improved photocatalytic properties towards the degradation of methylene blue [24]. On the other hand, the use of mixed organic linkers in synthesizing these materials increased the selectivity towards gas separation. ZIF-70 formed of a mixture of imidazole and nitro-imidazole is a conspicuous example of this selectivity [11].

## ***2. Synthesis techniques of ZIFs***

Various techniques were traditionally used to synthesize ZIFs. The synthesis reactions can occur in water or organic solvents where the temperature varies from room temperature up to 200 °C at a time scale from hours to days [23, 25, 26]. These synthesis techniques lead to the formation of powdered ZIFs, after separation from the reaction mixture and the removal of the solvents. Recently, membranes and films of ZIFs are synthesized due to their high importance in some applications, such as gas separation and chemical sensors.

### **a. Solvothermal Synthesis**

Conventionally, ZIF particles were synthesized via the solvothermal technique where the appropriate organic solvent forms the reaction medium. This technique is based on dissolving the organic linker with the metal salt in the appropriate solvent at high temperatures. In some cases, some organic amines are added to the medium. Their role is to induce the deprotonation of the linker and facilitate its coordination to the metal ions [27, 28]. The first ZIFs (termed as ZIF-1 to ZIF-12) were synthesized by

Yaghi et al. in different organic solvents such as N,N-dimethylformamide (DMF), N,N-diethylformamide (DEF) and N-methylpyrrolidone (NMP) [10]. By changing the solvent, different particle sizes can be obtained, in addition to the improvement of some of their properties. For example, ZIF-8 particles synthesized in the presence of methanol at high temperature have smaller size and higher surface area than the ones obtained with DMF [26].

b. Hydrothermal Synthesis

Since organic solvents are expensive and not environmentally friendly, their use has been reduced or completely avoided. The solvothermal method was then replaced by the hydrothermal method. The metal ion and the ligand are dissolved in aqueous solutions in different molar ratios. This technique was first based on mixing the two solutions in an autoclave at high temperature and pressure [25]. Recently, water-based systems at room temperature have been implemented in the synthesis of different ZIFs particles [27, 29].

c. Sonochemical Synthesis

In the sonochemical technique, an ultrasound-molecules interaction is coupled to a cavitation process, in which an interaction between the liquid and the high-energy ultrasound is generated [30]. This will lead to the formation of different pressure areas in the liquid. In the collapsed areas, bubbles known as acoustic cavitation are formed to generate high local temperature and pressure [31]. Compared to the conventional heating for ZIFs preparations, the sonochemical synthesis allows the promotion of nucleation and its dispersion homogeneously [32]. As a result, crystals obtained are

smaller with narrower particle size distribution than the conventionally synthesized materials [26, 33, 34].

#### d. Mechanochemical Synthesis

This technique is based on grinding the metal salt in the presence of an excess amount of the organic linker [35]. The product is obtained by breaking the intramolecular bonds under mechanical forces, followed by a chemical reaction [36]. Recently, mechanochemical technique is replacing other synthesis routes due to their significant potential as a green and efficient strategy for the construction of materials [37]. The synthesis of ZIFs mechanochemically is limited by the use of oxide-based precursors. Beldon *et al.* modified this technique to a so-called liquid-assisted grinding (LAG) or ion- and liquid-assisted grinding (ILAG) to produce ZIFs from a stoichiometric molar ratio (1:2) of ZnO and ligand, such as imidazole, 2-methylimidazole and 2-ethylimidazole at room temperature [38, 39]. They were also able to control its topology by changing the grinding solvents and the salt additives. Moreover, apart from the crystalline ZIFs, amorphous ZIFs can be obtained by ball milling too. Cheetham *et al.* were able to synthesize various amorphous ZIFs by grinding the starting materials [40-42].

#### e. Dry-gel Conversion (DGC)

In this method, a hydrogel containing all sources is converted to a crystalline microporous medium [43]. The DGC has potential advantages including the reduced reactor size, the use of non-organic solvents and the possibility of continuous production [44]. Moreover, shape-controlled porous materials can be obtained from

preshaped gel[45]. Shi *et al.* first applied this technique in the synthesis of ZIF-8 and ZIF-67 in aqueous solution without using any additives. This method differs from other solvothermal syntheses by having a high concentration of the solid phase and an obvious separation of the solid and the liquid phase [46].

f. Ionothermal Synthesis

The ionothermal technique is a new synthesis strategy that has been recently developed to generate ZIF materials [47-49]. It is based on the use of green solvents such as ionic liquids and eutectic mixtures[50]. Ionic liquids are used of their negligible vapor pressure, non-flammability and recyclability [48, 51]. For instance, the reaction occurring via this technique can be performed in open systems. The advantage of using ionic liquids resides in their functionalities that differ from the usual hydrothermal strategies. They act as solvents, charge compensating species and structure directing agents[50]. For example, Martins *et al.* used the ionic liquid 1-ethyl-3-methylimidazolium bis-(trifluoromethyl)sulfonylimide in the synthesis of four different ZIFs [48] whereas Yang *et al.* applied the 1-butyl-3-methyl-imidazolium tetrafluoroborate to produce ZIF-8 particles [49].

g. Microfluidic Synthesis

ZIFs can also be synthesized using a microfluidic method where both the immiscible liquids of the organic linker and the metal ions are injected to a T-junction syringe pumps. Herein, aqueous solution droplets are formed in continuous organic phase. The capsule of the ZIF is formed at the liquid-liquid interface simultaneously as the droplets pass through a hydrophobic tubing. The flow rates of both solutions are

independent and can be adjusted separately. It is noteworthy that this technique is very useful to develop nanosized ZIF particles [52-54].

### ***3. Applications of ZIFs***

The intrinsic properties of ZIFs, such as mimicking the structure of zeolites and porous materials, adjustable functionalities and excellent textural properties, allow ZIF materials to be an important class of crystalline porous materials with versatile applications. Despite their similarities with MOFs, ZIFs tend to be more applied in the process of carbon capturing. This is due to their high thermal and chemical stability allowing their application on wide range of temperature [55]. Moreover, the use of ZIFs ranges from the conventional techniques including adsorption of dyes and contaminants in water [56], gas separation [18] and catalysis [16] to sensing electronic devices and drug delivery [20]. In this section, we will describe briefly the most important applications of ZIFs.

#### **a. Gas separation**

Recently, gas separation is being widely investigated with the increase of the global issues such as natural gas purification, and carbon dioxide capture. Thus, developing a green and energy-efficient method to realize gas separation became urgent. Being a novel class of highly porous materials with similarities to zeolites and other porous materials, ZIFs are considered good candidates in gas separation process. Therefore, ZIF membranes are used in various gas separation applications. Some of these applications are summarized in Table 1. It is clearly shown that ZIFs are widely used in the separation of hydrogen and carbon dioxide. The separation process is



controlled by different structural parameters. Thus, the selectivity can be improved by altering the pore size and functionalities. For example, Li *et al.* succeeded in synthesizing a ZIF-7 membrane highly selective for hydrogen gas. In fact, the pore size of ZIF-7 (0.3 nm) is between the molecule size of H<sub>2</sub> (0.29 nm) and CO<sub>2</sub> (0.33 nm) [57, 58]. In addition, ZIF-8 is considered another important candidate for separating hydrogen molecules from other big molecules [59]. This goes back to the pore size and its hydrophobic nature. Bux *et al.* were able to register a selectivity of a factor of 11.2, higher than the separation by any other porous material [60]. In addition, ZIF-8 is used in the separation of C<sub>2</sub>-C<sub>3</sub> hydrocarbon mixtures such as ethane/propane, ethylene/propylene, ethylene/propane and propylene/propane [61-64].

**Table 1:** List of Zeolitic imidazolate frameworks used in the separation of gases from mixtures.

Material	Gas mixture
ZIF-7	H <sub>2</sub> /CO <sub>2</sub> , H <sub>2</sub> /N <sub>2</sub> , H <sub>2</sub> /CH <sub>4</sub> [57, 65]
ZIF-8	H <sub>2</sub> /CO <sub>2</sub> , H <sub>2</sub> /N <sub>2</sub> , H <sub>2</sub> /CH <sub>4</sub> [66, 67]
ZIF-8	C <sub>2</sub> H <sub>6</sub> /C <sub>3</sub> H <sub>8</sub> , C <sub>2</sub> H <sub>4</sub> /C <sub>3</sub> H <sub>6</sub> , C <sub>2</sub> H <sub>4</sub> /C <sub>3</sub> H <sub>8</sub> [62]
ZIF-78	H <sub>2</sub> /CO <sub>2</sub> [68]
ZIF-9 and hybrid ZIF-67	H <sub>2</sub> /CO <sub>2</sub> [69]
ZIF-69	CO <sub>2</sub> /N <sub>2</sub> , CO <sub>2</sub> /CO, CO <sub>2</sub> /CH <sub>4</sub> [70]
ZIF-95	H <sub>2</sub> /CO <sub>2</sub> [71]

#### b. Adsorption

ZIF materials have been widely employed as adsorbent for water purification. Among the large family of ZIFs used for this purpose, ZIF-8 remains the most used one since it showed high selectivity towards different ions and water contaminants, such as

the arsenic and the p-arsenate [72-74], chromium (VI) ions [75], humic acid [76], phthalic acid [77, 78], diethyl phthalate [77] and benzotriazoles [79]. Moreover, ZIF-8 is highly used in the adsorption of organic dyes from water. For instance, Li *et al.* applied ZIF-8 particles in the adsorption of rhodamine B, methylene blue and methyl orange [56]. The adsorption of methylene blue using ZIF-8 particles is reported to be one of the fast and efficient adsorption ( $q_{max} = 3.1 \text{ mmol.g}^{-1}$ , contact time: 30 min) among other materials such as the activated charcoal ( $q_{max} = 25 \text{ mmol.g}^{-1}$ , contact time: 30 min) and graphene oxide ( $q_{max} = 4.0 - 4.5 \text{ mmol.g}^{-1}$ , contact time: 120 min) [80]. Furthermore, Saliba *et al.* recently studied the adsorption of MB by ZIF-8 and ZIF-67 and their mixed metal derivatives. They showed that the substitution of Zn by Co cations within the ZIF framework enhances the adsorption capacity of the ZIF particles [24]. The mixed metals strategy in ZIFs for adsorption of dyes was also investigated by Thanh *et al.* and Abdi *et al.* By doping ZIF-8 with iron, Thanh *et al.* succeeded in increasing the adsorption capacity of ZIF-8 doped with iron towards the remazol deep black dye (RDB) [81]. Whereas Abdi *et al.* used the amine-modified ZIF-8 for the adsorption of two different anionic dyes: the acid blue 92 (AB92) and direct red 80 (DR80). Upon this modification, the adsorptive capacity of ZIF-8 increased from 250 mg/g to 650 mg/g for AB92 and from 200 mg/g to 500 mg/g for DR80 [82].

### c. ZIFs as catalysts

Zeolites have been also used as catalysts for many industrial processes [83]. However, when synthesizing bulky materials, there are some limitations due to their small pore sizes and surface areas. By synthesizing ZIFs, this challenge was overcome because of the incorporation of the organic linker and the transition metal in the

framework [10]. Both the metal ion and the organic linker are involved in a catalytic reaction. Furthermore, the diversity in the size of the pores provides ZIFs high selectivity and affinity towards the target material [84]. Additionally, the electronic and steric properties of the transition metal sites can be tuned by functionalizing the organic linker leading to an enhancement in the catalytic properties of the pores, which is also considered a major explanation for the use of ZIFs in this field [10]. Different ZIF catalysts were used in many reactions including: transesterification [85], Knoevenagel reaction[86], Friedel-Crafts acylation [87, 88], monoglyceride synthesis [89], synthesis of carbonates[90, 91], oxidation and epoxidation [92-94], and hydrogen production [95]. For example, the transesterification of vegetable oil in methanol has been improved when replacing zinc aluminate, the conventional catalyst, by ZIF-8 particles [85].

#### d. ZIFs in sensing and electronic devices

The exceptional and intrinsic properties of ZIFs such as the tunable pore size, the easy functionalization and the selective adsorptive capacity enable them to be used in sensing and electronic devices. For instance, ZIF-8 was used for the first time as a sensing material when constructing a ZIF-8 -based Fabry-Pérot device. This device serves as a selective sensor for chemical vapors and gases. An exceptional chemical selectivity was reported when the sensor was exposed to the vapor of ethanol-water mixtures in addition to an ethanol-concentration-dependence response [96]. Moreover, ZIF particles were studied as luminescent probes for the detection of metal ions [97] ( $\text{Cu}^{2+}$  and  $\text{Cd}^{2+}$ ) and small molecules [97] such as acetone and a sensing platform for

fluorescence-enhanced detection of nucleic acids having a high selectivity down to a single-base mismatch [98].

Furthermore, these materials are considered as attractive matrices for the biosensor construction, where ZIFs-based electrochemical biosensors for in vivo electrochemical measurement with high selectivity and sensitivity towards glucose were successfully synthesized. ZIF-7, ZIF-8, ZIF-67, ZIF-68 and ZIF-70 served as a matrix respectively for co-immobilizing electrocatalysts methylene green and glucose dehydrogenase on the electrode surface [99].

Additionally, ZIFs are used in electronic devices [100]. Recently, Eslava and co-workers claimed that ZIF-8 can be considered as good insulators in microelectronics. The synthesized ZIF-8 films showed good mechanical properties and had the effective  $\kappa$  value necessary for the chip devices [101].

#### e. ZIFs in drug delivery

ZIF materials are emerging as powerful materials for drug delivery and controlled release of drug molecules [102-104]. This is explained by the excellent porous structures, the exceptional thermal and chemical stabilities and the tunable pore size of the framework.

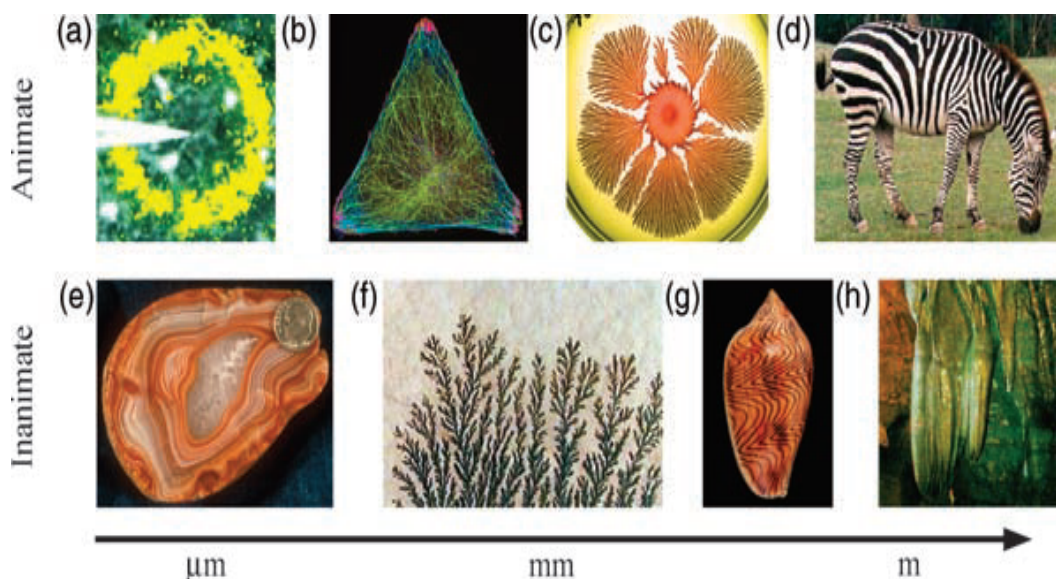
Among the vast family of ZIF, ZIF-8 is considered as a good candidate for the delivery of drugs such as anticancer agents [20]. Sun *et al.* suggested that this framework can be used as a drug delivery vehicle that is dependent on the pH of the solution, since it is highly stable in water and sodium hydroxide solutions, and decomposable in acidic medium [10]. Besides being able to deliver drugs and encapsulate them within their

cage, ZIF-8 particles provide a thermal protection for the drug during high temperature processes [105].

## **B. Reaction-Diffusion Framework**

### ***1. Introduction***

Organized patterns are observed in real life in different fields including chemistry, physics, biology and abundantly geology. They are defined as the appearance of an array of organized structures repeated with defined or undefined symmetries without the intervention of external conditions, and arise far from equilibrium [106]. They affect significantly the animate systems as well as the inanimate systems. For instance, the combination of the nonlinear coupling with the feedback loops is keen to provide a basis for regulatory processes in cells, tissues and organisms (calcium signals, communication between ATP generation (mitochondria) and ATP consumption sites (cell nucleus and membranes). Moreover, the combination of the nonlinear coupling between the reaction and the diffusion may induce chemical oscillations in time and/or in space. On the other hand, extended structures are born from simple and inorganic chemistries by the reaction-diffusion. Very common examples are the iris banding of the agate, the cave stalactites and the dendritic formation on the limestone (Figure 4) [107].

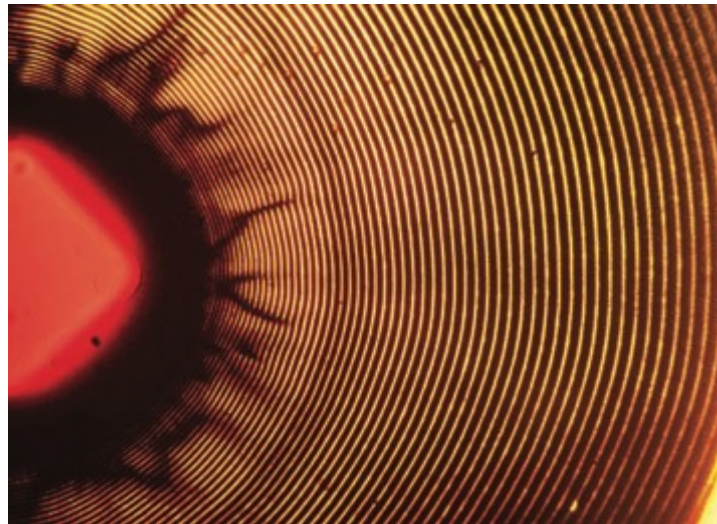


**Figure 4:** Examples of animate (a-d) and inanimate (e-h) RDF systems at different length scales ( $\mu\text{m}$ , nm and m) . Reprinted with permission from ref. [106]. Copyright 2009 John Wiley and Sons.

The reaction-diffusion framework (RDF) is based on the diffusion of two initially separated reactants, where one reactant (outer electrolyte) is poured on top of the second one (inner electrolyte) entrapped into a gel matrix that eliminates the convection process. The difference in the concentrations of the two reactants leads to the establishment of a concentration gradient. A supersaturation wave is then initiated at the gel-solution interface and propagates decreasingly down the reaction tube. While the nucleation dominates at the interface where the supersaturation is the highest, growth predominates further in the tube when the supersaturation is lower. Due to the nonlinear interaction of this diffusing supersaturation with nucleation and crystal growth, the Liesegang instability (described below) resulting in macroscopic periodic precipitation may emerge.

Liesegang instability was first discovered by the German chemist, Raphael Eduard Liesegang in 1896 [108], by accidentally dropping a solution of silver nitrate

( $\text{AgNO}_3$ ) on a thin layer of gelatin containing potassium dichromate ( $\text{K}_2\text{Cr}_2\text{O}_7$ ) [109]. This led to the formation of concentric rings of silver dichromate. The periodic precipitation patterns or the Liesegang instability, formed by moving the front of the chemical reaction, is considered one of the most interesting examples of self-organizing systems far from equilibrium. Liesegang was unable to explain the origin of the formed rings, nonetheless, he knew that it was related to the movement of molecules or ions with respect to one another.



**Figure 5:** Classic Liesegang rings formed in a silver dichromate system in gelatin. Reprinted with permission from ref. [106]. Copyright 2009 John Wiley and Sons.

Since scientists succeeded in recreating the naute-like behavior in a test tube, reaction-diffusion became crucial in modern technology. In fact, the nonlinear coupling of the reaction and diffusion allows the construction of new structures at small scales such as bands with direct spacing [110], bands with revert spacing [111, 112], bands with secondary structures [113], fractals [114] and spots [115]. It starts with the conversion of the components via a chemical reaction and ends with their transportation in space via diffusion. The eminence of the reaction-diffusion framework leans on the

ability to study and control the size and the morphology of the particles within each band. The variation of the concentration of the electrolytes, as well as the gel matrix concentration and the temperature affected the size and the morphology of the MOF-199 [116] and the lanthanum hydroxide particles synthesized via this technique [116, 117].

## ***2. Theories governing the Liesegang banding phenomena***

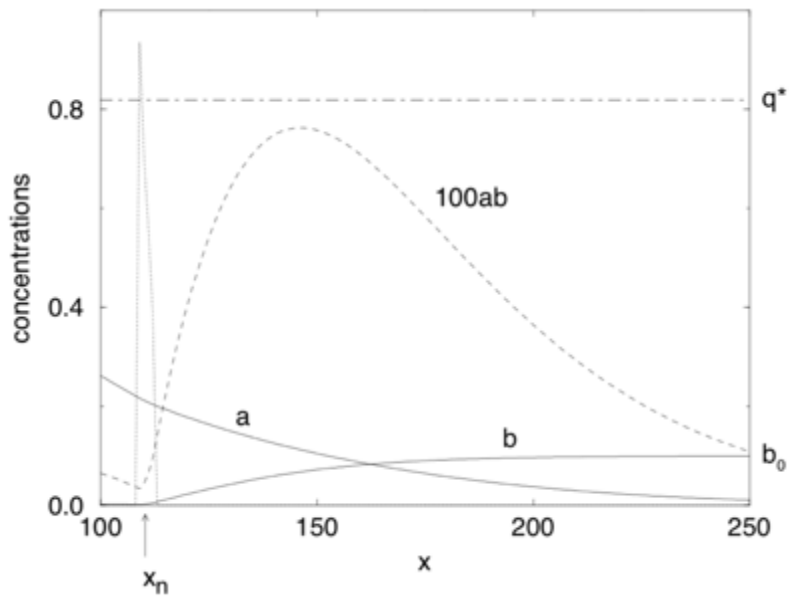
Various studies were carried out to study the mechanism behind the Liesegang banding phenomena. Till now, there's no universal theory that explains every experimental observation regarding this phenomenon. However, the pre-nucleation theory, based on the Ostwald's supersaturation theory [118-121], and the post-nucleation theory [122] based on the Ostwald's ripening were the most discussed theories with several advantages and limitations.

### **a. Pre-nucleation Theory**

The Ostwald supersaturation-nucleation-depletion [107] cycle was first used to describe the phenomenon that happens when the bands are formed. It is based on explaining the periodic precipitation as a non-equilibrium process. The first precipitation bands do not appear immediately upon the diffusion of the outer electrolyte ( $A$ ) into the gel containing the inner electrolyte ( $B$ ), but after the supersaturation of the solution. The nucleation of the precipitate is then initiated and accompanied by a growth of the nucleated particles with a depletion of the electrolytes  $A$  and  $B$  in the surroundings. Therefore, the local concentration product of the reactants  $a(x, t) \times b(x, t)$ , where  $a$  is the concentration of the outer electrolyte ( $A$ ) and  $b$  is the concentration of the inner electrolyte ( $B$ ), decreases in the vicinity of the band and the



nucleation is inhibited. Afterwards, the diffusion of  $A$  continues until it surpasses again the nucleation threshold of precipitation  $q^*$ , or the solubility product ( $K_{sp}$ ), allowing thus the formation of a new band. The repetition of this cycle leads to an alternative precipitation of filled and void domains. A computational simulation in figure explains the formation of the  $n^{\text{th}}$  band with  $a$  and  $b$  the concentrations of the products,  $ab$  their ion-product,  $x_n$  the position of the band  $n$  and  $q^*$  the precipitation threshold [123].



**Figure 6:** Computational simulation of the concentrations of  $a$  and  $b$ , and the ion-product concentration  $ab$  in the supersaturation theory of the Liesegang banding.  $q^*$  represents the precipitation threshold,  $x_n$  the position of the  $n^{\text{th}}$  band. Reprinted with permission from ref. [122]. Copyright 2005 Institute for Scientific Information.

Wagner [124] and Prager [118] tried to improve this theory by different calculations and mathematical formulations, so it agreed at first with the experimental observations. However, its major drawbacks reside in not being able to explain the revert spacing [125] and the pattern formation from an initially uniform dispersion of a precipitate in a gel medium [126] beside its failure in predicting the secondary banding [113].

## b. Post-Nucleation Theory

The post-nucleation theory is established on two mechanisms: the competitive particle growth model (CPG) and the Nucleation and Growth [107]. The first one, known also as the Ostwald ripening, is based on the chemical instability where the obtained sol evolves after diffusion through a competing mechanism between particles of different sizes. Feinn et *al.* argues that in order to decrease the energy of the system, smaller particles are dissolved whereas bigger ones are formed. Moreover, the periodic precipitation was explained as a mechanism of the aggregation of big particles, leaving depleted clear zones in smaller particles in the surrounding regions [123, 124, 126-128].

The second theory is characterized by two thresholds, one for the nucleation and other for the growth. In fact, this model proposes that spatially homogeneous colloidal sets of particles ( $C$ ) are formed after the diffusion of the outer electrolyte ( $A$ ) into the gel containing the inner electrolyte ( $B$ ) and when the local concentration product  $a(x,t) \times b(x,t)$  is greater than the solubility product ( $K_{sp}$ ). These colloidal particles are free to move until their local concentration  $c$  reaches a threshold value  $c^*$ , inducing the nucleation followed by an aggregation into a static precipitate  $P$  until concentration  $c$  drops below the second threshold  $p^*$  [123, 129].

### ***3. Scaling laws of the Liesegang banding phenomenon***

The precipitation pattern of the Liesegang banding phenomenon follows different scaling laws, regardless of the symmetry of the system and the identity of used salts. These laws are defined as the spacing law, the width law and the Matalon-Packter law.

a. The spacing law

The first scaling law that relates the positions  $x_n$  and  $x_{n+1}$  of the consecutive bands  $n$  and  $n + 1$  is known as the spacing law [107, 130]. It was first described by Jablczynski [131] and states that the positions of consecutive bands form a geometrical series as shown in equation (1):

$$\frac{x_{n+1}}{x_n} = 1 + p \quad \text{eq.1}$$

where  $p$ , defined as the spacing coefficient, ranges between 0.05 and 0.4 [123].

In general, the spacing between the consecutive bands increases with the increase of the distance from the interface between the outer electrolyte and the gel. This spacing is known as the direct or the normal spacing. In other cases, the Liesegang systems exhibit a revert spacing where the distance between the consecutive bands decreases as going far from the interface [111, 112].

b. The width law

The relation between the widths of consecutive bands follows the width law [107][107][107][107] stating that the ratio of the widths ( $w$ ) of two consecutive Liesegang bands, defined as  $q$ , is constant. The width values form a geometrical series [132-134]:

$$\frac{w_{n+1}}{w_n} = q \quad \text{eq. 2}$$

Furthermore, in a direct spacing system the width of the band increases with its position in regard to the interface according to the equation (3):

$$\ln w_n = \alpha \ln x_n + \text{constant} \quad \text{eq. 3}$$

where the width exponent  $\alpha$  is greater than 1.

c. The Matalon-Packter law

Matalon and Packter postulated a new law in order to better understand the spacing law. This law describes the relation between the initial concentrations of the inner and the outer electrolytes with the spacing coefficient. They noted that the spacing coefficient  $p$  depends on the initial outer ( $a_0$ ) and inner ( $b_0$ ) concentrations as follows:

$$p = F(b_0) + \frac{G(b_0)}{a_0} \quad \text{eq.4}$$

where  $F$  and  $G$  are either decreasing or increasing functions of  $b_0$  [123, 135].

**C. Aim of the work**

As previously mentioned, the family of Zeolitic Imidazolate frameworks is large due to the different organic linkers and metal ions that can be used, inducing their high importance in different applications. The size and the monodispersity of the particles are very important parameters in many applications such as separation membranes and catalysis; however, conventional synthesis techniques yield polydispersed ZIF particles. The reaction-diffusion framework is considered an interesting alternative technique that overcome the size and dispersity issue. In fact, the nonlinear coupling between reaction and diffusion with nucleation and growth of the crystals allows with ease the control of particle size and its distribution along the tubular reactor. In addition, this method is rapid, efficient, scalable, and environmentally friendly.

Herein, we report the synthesis of two zeolitic imidazolate frameworks (ZIF-8 and ZIF-7) via a reaction diffusion framework at room temperature. The periodic precipitation for both systems occurs in a series of alternative bands separated by precipitate-free zones and obeying the direct spacing Liesegang banding. Different experimental conditions such as the concentrations of the metal ions (inner solution)

and the organic linker (outer solution), the agar gel percentage and the temperature are varied in order to study their effect on the crystal size, the morphology and the stability along with other properties. Therefore, our aim is to exploit the macroscopic scaling laws emerging from the Liesegang instability and couple it to the particle size in order to introduce a new microscopic size law. This law relates the size of the ZIF-7 particles in each band to the position of the band in the tube. Furthermore, by capturing *in situ* the crystal growth, this new method of ZIF synthesis enables the elucidation of the fundamental physico-chemical parameters that govern the crystallization process of ZIF structures.

## CHAPTER II

### MATERIALS AND METHODS

#### A. Materials

Zinc sulfate monohydrate ( $\text{ZnSO}_4 \cdot \text{H}_2\text{O}$ , 99%), zinc acetate dihydrate 97%, 2-methylimidazole 99% and benzimidazole 98% were purchased from Acros Organics, Bacto agar gel from Difco, N-N-dimethyl formamide (DMF) and dichloromethane (DCM) from Fisher chemicals, and cobalt (II) sulfate heptahydrate from BDH Laboratory Supplies. All these reagents were used without further purification.

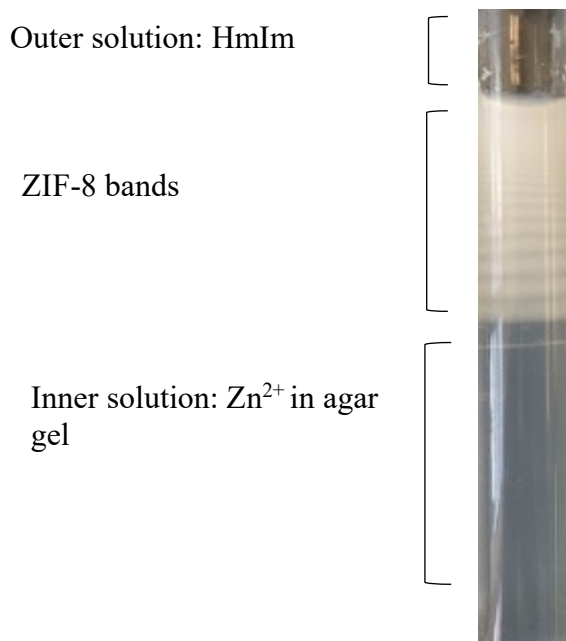
#### B. Preparation of ZIF crystals

Our synthesis technique is based on the diffusion of the organic linker into a gel matrix containing the metal ions. For ZIF-8 and ZIF-7 systems, the metal ions constitute the inner electrolyte, whereas the outer electrolyte is formed of a solution of the organic linker, 2-methylimidazole or benzimidazole. In order to allow diffusion, the concentration of the outer electrolyte is 50 times (more or less) that of the inner electrolyte.

##### 1. Preparation of ZIF-8

An aqueous solution of  $\text{Zn}^{2+}$  ions from zinc sulfate powder is mixed with 1% (w/w) agar powder and heated with continuous stirring. At the complete dissolution of the gel, an equal volume of DMF is added. The homogeneous solution is transferred into a Pyrex test tube and kept at room temperature until gelation. An aqueous solution

of 2-methylimidazole (HmIm) is added on the top of the gel and left to allow the precipitation coupled with the diffusion.

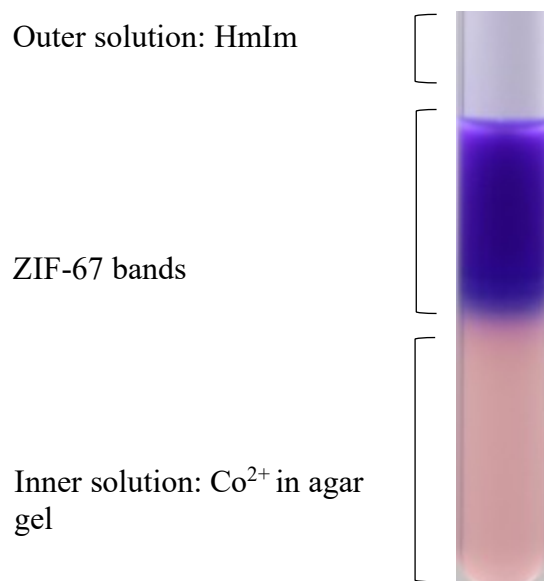


**Figure 7:** Schematic representation of ZIF-8 synthesis via RDF.

After 3 days of diffusion, white bands of pure ZIF-8 are formed. The precipitates are washed in DMF at high temperature to remove the gel and the unreacted species, then with DCM by solvent exchange to clear the pores from DMF, and then dried for 2 hours to be ready for characterization.

## 2. Preparation of ZIF-67

ZIF-67 is prepared similarly to ZIF-8 with the same outer solution of HmIm. However, the inner solution is formed of Co<sup>2+</sup> ions instead of Zn<sup>2+</sup> ions. The purple precipitate is collected and treated in the same manner of the white precipitate of ZIF-8.

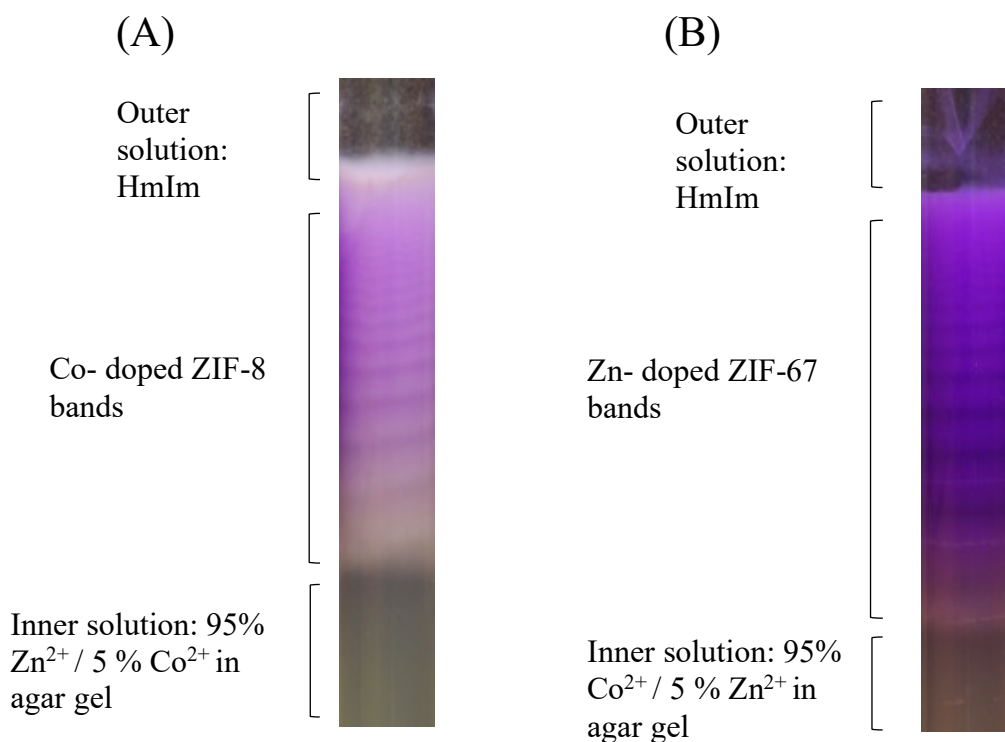


**Figure 8:** Schematic representation of ZIF-67 synthesis via RDF.

### ***3. Preparation of Co-doped ZIF-8 and Zn-doped ZIF-67***

A mixture of different percentages of  $\text{Zn}^{2+}$  ions and  $\text{Co}^{2+}$  ions is used in the inner solution for the preparation of the Co-doped ZIF-8 and the Zn-doped ZIF-67 crystals. For the first one, the percentage of the zinc is higher than that of the cobalt, whereas for the Zn-doped ZIF-67 the cobalt percentage is the highest.



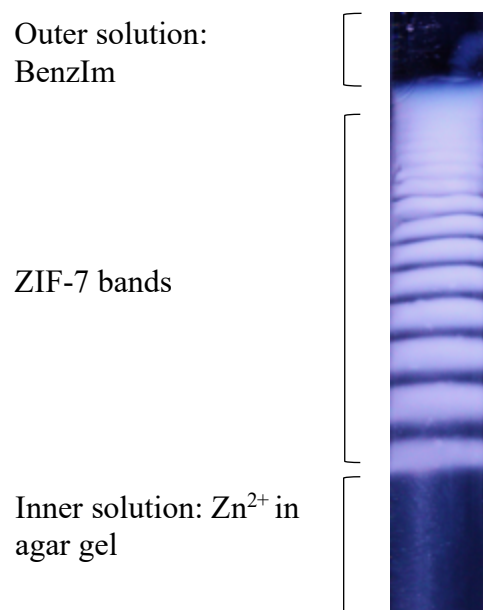


**Figure 9:** Schematic representation of 5% Co-doped ZIF-8 (A) and 5 % Zn-doped ZIF-67 (B) via RDF.

#### 4. Preparation of ZIF-7

Zinc acetate powder is dissolved in water and mixed with 1% (w/w) agar powder to form the gel matrix of the ZIF-7 system. The solution is heated with continuous stirring until the dissolution of the gel. An equal volume of DMF is added and the homogeneous solution is transferred into a Pyrex test tube and kept at room temperature until gelation. A solution of benzimidazole dissolved in an equal volume of DMF and water is added on the top of the gel.

Similar to the ZIF-8 systems, the white precipitates are extracted where individual bands are separated, washed with DMF at high temperature to remove the gel, washed with DCM by solvent exchange and dried for 2 hours to be characterized.



**Figure 10:** Schematic representation of ZIF-7 synthesis via RDF.

### C. Characterization of ZIF-8, ZIF-67 and ZIF-7 crystals

After collecting ZIF crystals, they are subjected to different characterization techniques including Powder X-Ray diffraction, Scanning Electron Microscopy, Thermogravimetric analysis, BET surface area measurements and Atomic Absorption measurements.

#### 1. Powder X-Ray diffraction (PXRD)

Powder X-Ray diffraction (PXRD) is a non-destructive technique allowing the identification of the powder since each sample is characterized by a unique PXRD pattern. It can be used to determine the crystal structure and the size of the particle according to the Scherrer equation.

Powder X-Ray diffraction (PXRD) patterns are recorded on a Bruker D8 advance XRD diffractometer using CuK $\alpha$  radiation ( $\lambda = 1.5406 \text{ \AA}$ ) at 40 kV and 40 mA,

with  $2\theta$  ranging between  $5^\circ$  and  $40^\circ$  at a scanning rate  $0.02^\circ \cdot \text{min}^{-1}$  and a total time of 12 hours.

## ***2. Scanning Electron Microscopy Analysis (SEM)***

The morphology and the size of the particles in each of the extracted bands are investigated using a scanning electron microscope (Tescan Mira), operating at 5 kV; and equipped with Oxford detector for energy dispersive X-ray (EDX) characterization at 15 kV. The samples are coated with a layer of gold prior to SEM. Note that the error bars in the figures represent the standard error on the mean with a number of particles  $n = 100$  particles.

## ***3. Thermogravimetric analysis (TGA)***

Thermogravimetric analyses are carried out on a NETZSCH TG 209F1 Libra TGA209F1D- 0152-L to study the thermal stability of the samples. The analyses are done under nitrogen atmosphere with a heating rate of  $5^\circ\text{C} \cdot \text{min}^{-1}$  and a temperature between  $30^\circ\text{C}$  and  $1100^\circ\text{C}$ .

## ***4. Nitrogen adsorption and BET calculation***

In order to analyze the surface area of the porous material, nitrogen isotherms are carried on using a Micromeritics ASAP 2420 analyzer. The BET surface area is calculated using NOVA 2200e surface area analyzer after degassing the samples for 6 hours at  $80^\circ\text{C}$  under vacuum.

## **5. *Atomic Absorption (AA)***

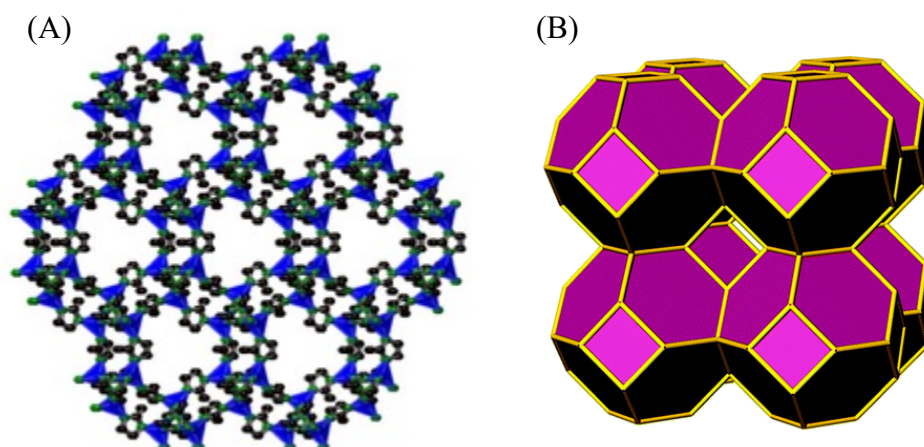
Atomic absorption measurements are recorded using THERMO LABSYSTEMS, SOLAAR atomic absorption spectrophotometer with ASX-510 auto sampler, and SOLAAR data acquisition. After washing the samples, they are dissolved in 1.0 M HCl and examined by means of atomic absorption to determine the exact doping percentage.

## CHAPTER III

# SYNTHESIS AND CHARACTERIZATION OF ZIF-8, ZIF-67 AND THEIR MIXED METALS DERIVATIVES VIA A REACTION-DIFFUSION FRAMEWORK

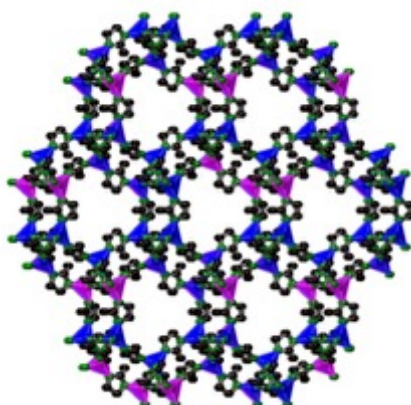
### A. Introduction

Zeolitic imidazolate framework 8 (ZIF-8) was first synthesized by Yaghi *et al.* in 2006 by mixing zinc nitrate tetrahydrate with 2-methylimidazole in N,N-dimethylformamide (DMF) at 140 °C for 24 hours. The zinc ions and the 2-methylimidazolates form a cubic crystal with  $I\bar{4}3m$  as a space group ( $a = 16.991 \text{ \AA}$ ). Each zinc ion is tetrahedrally coordinated to the nitrogen atoms of the imidazolate ring. The crystallographic study of ZIF-8 showed a sodalite (SOD) topology which is truncated octahedron known also as the Kelvin cell. The large pores of the SOD cage are of  $11.6 \text{ \AA}$  and are connected through 6-ring small apertures of  $3.4 \text{ \AA}$  each at  $\langle 111 \rangle$  facets.



**Figure 11:** (A) The crystal structure of ZIF-8. The blue tetrahedra are formed of Zinc ions, the black spheres represent the carbon atoms and the green spheres represent the nitrogen atoms and (B) the SOD topology. Reprinted with the permission of ref [9]. Copyright 2006, Proceedings of the National Academy of Sciences.

ZIF-8 particles show high thermal stability up to 450 °C in ambient conditions in addition to their chemical stability in boiled benzene, methanol and water for a week. The exceptional thermal and chemical stabilities in addition to the high surface area (BET of 1640 m<sup>2</sup>/g) and the pore volume of 0.636 cm<sup>3</sup>/g make ZIF-8 an ideal compound for a wide variety of applications [10]. ZIF-8 was used in various applications such as the storage of hydrogen, methane and capture of carbon dioxide, the separation of liquid mixtures, chemical sensors, drug delivery and photocatalytic degradations. By replacing zinc ions with cobalt ions, a new ZIF is obtained, known as ZIF-67, having the same structure and topology as ZIF-8 [11]. Recently, various studies showed that the synthesis of ZIF crystals based on mixed metals allows an improvement in the properties of the material [24].



**Figure 12:** Crystal structure of Co-doped ZIF-8, Zn: blue, Co: purple, N: green and C: black.

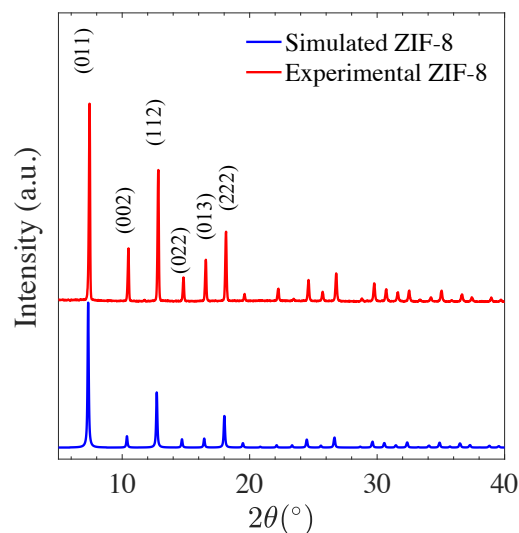
Over the years, the synthesis of ZIF-8 and ZIF-67 crystals was monitored by changing the solvents, the temperature, the pressure and the metal salts, in order to obtain a material with desirable particle size mandatory for the fabrication of nano-devices and their use in different applications. Since the reaction-diffusion framework allows us to control the particle size, in the upcoming section we will discuss the

characterization of the synthesized ZIF-8, ZIF-67 and their solid solution using RDF. Additionally, the study of the effect of the different reaction parameters, including the concentrations of the metal ions and the organic linker solutions, the gel percentage and the temperature, on the size of the particles will be discussed. Moreover, we will investigate the scaling laws emerging from the exhibited Liesegang instability.

## B. Results and Discussion

### 1. Powder X-Ray Diffraction of ZIF-8 crystals

PXRD pattern of the obtained crystals is recorded and compared to the simulated pattern (Figure 13). The sharp peaks observed in the PXRD pattern of the collected white powder synthesized via the RDF perfectly match the main peaks of the simulated pattern of ZIF-8 at  $2\theta$  :  $7.51^\circ$  (011),  $10.49^\circ$  (002),  $12.89^\circ$  (112),  $15.01^\circ$  (022),  $16.61^\circ$  (013), and  $18.26^\circ$  (222). Note that no additional peaks are observed. This indicates the high crystallinity and the purity of the synthesized crystals.

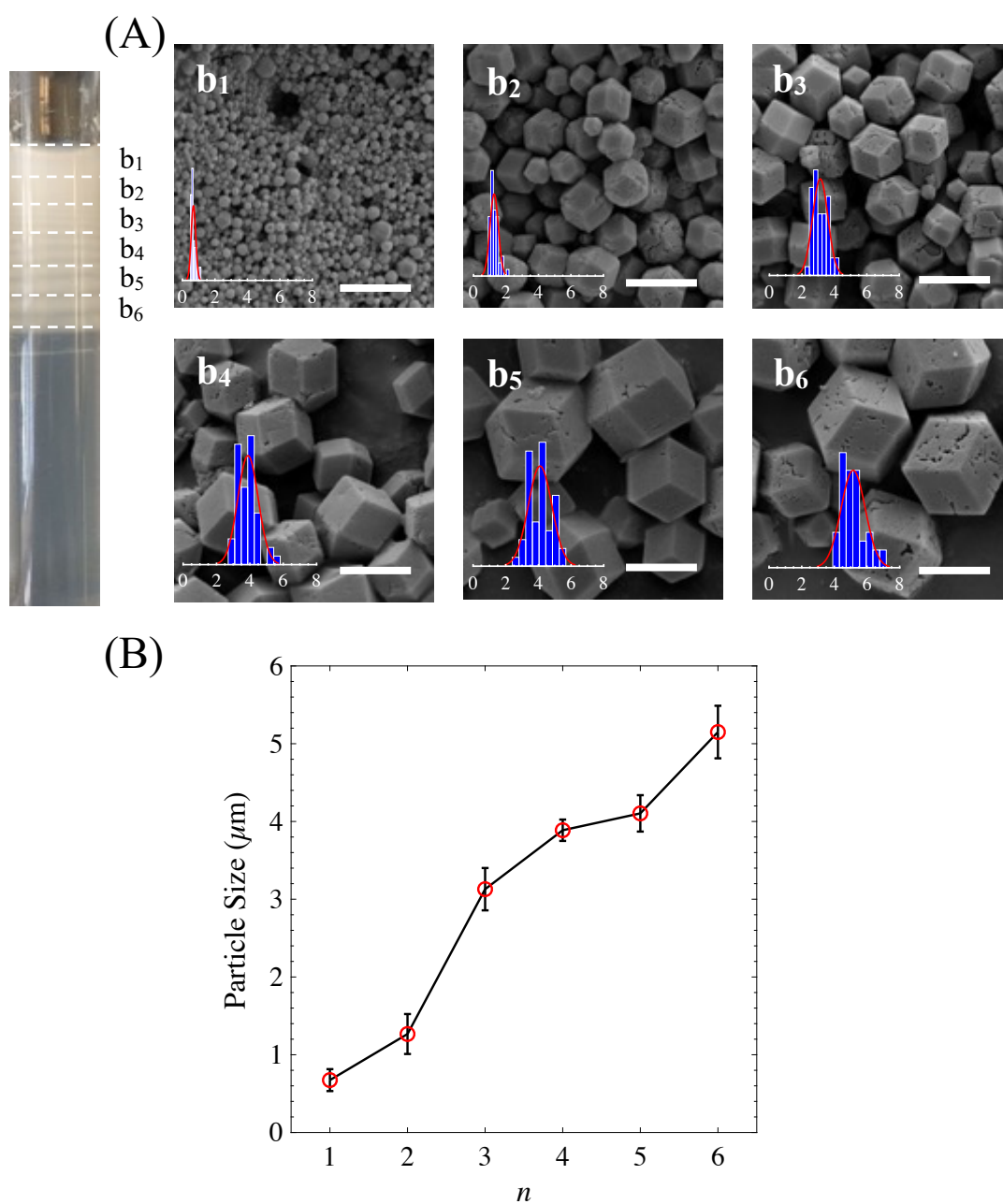


**Figure 13:** PXRD patterns of the simulated ZIF-8 crystals and the synthesized ZIF-8 via RDF.

## ***2. Scanning Electron Microscopy Analysis and Particle Size Distribution of ZIF-8 Crystals***

A tube of an inner  $[\text{Zn}^{2+}] = 20.0 \text{ mM}$ , an outer  $[\text{HmIm}] = 1.0 \text{ M}$ , an agar percentage of 1% is prepared and the precipitation is kept at a temperature of  $25 \text{ }^\circ\text{C}$  was prepared. Six consecutive bands of  $0.5 \text{ cm}$  each are collected and subjected to Scanning Electron Microscopy in order to examine the morphology of the particles. The SEM images reveal sharp edged polyhedra within the bands. Moreover, an increase in the size of these polyhedra within the same tube as we go farther from the gel-outer solution interface. This is characteristic of RDF where at the interface, the nucleation predominates and induces the formation of smaller particles. As we go far from this interface, the growth predominates resulting in the formation of larger particles (Figure 14). For example, in the first band the size of particles is  $\sim 0.8 \text{ }\mu\text{m}$  whereas, at the 6<sup>th</sup> band their size increases to  $\sim 5 \text{ }\mu\text{m}$ .

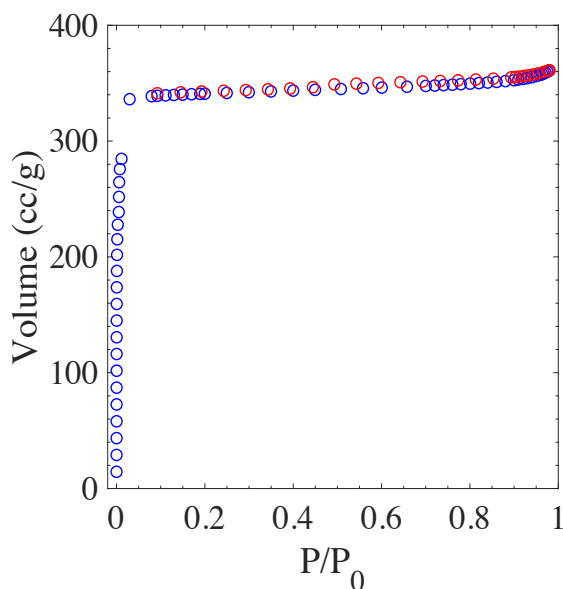




**Figure 14:** (A) SEM images showing polyhedral ZIF-8 particles synthesized via RDF and their size distribution in  $\mu\text{m}$  (histograms inset). The scale bar is  $2 \mu\text{m}$  and (B) a graph of the particle size growth over 6 consecutive bands. The bands are collected as adjacent regions of  $0.5 \text{ cm}$  each.

### 3. BET surface area of ZIF-8 crystals

The BET surface area and the pore volume of the obtained particles are calculated and found to be 1424 m<sup>2</sup>/g (Figure 15) and 0.56 cm<sup>3</sup>/g. These values are in accordance with the reported values in the literature [10]. This indicates that the RDF technique did not affect the textural properties of the ZIF crystal. The N<sub>2</sub> isotherm exhibited by ZIF-8 particles is a Type I isotherm confirming the microporous nature of the particles and depicting a monolayer adsorption on their surface.

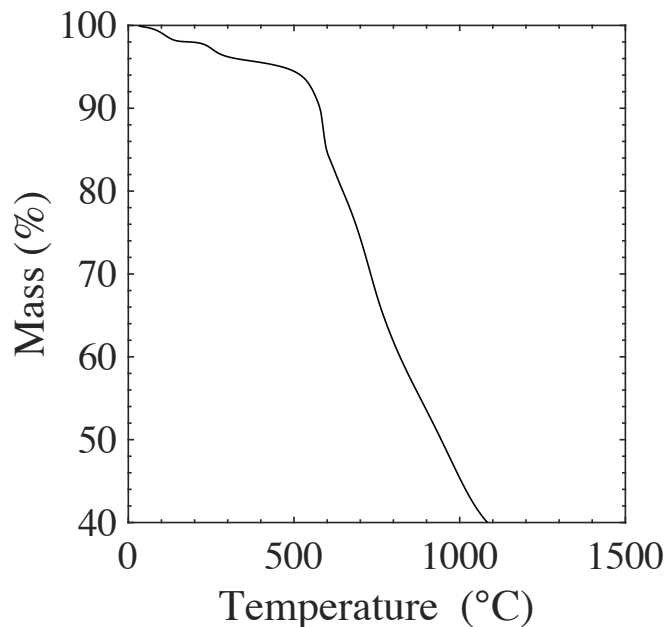


**Figure 15:** N<sub>2</sub> adsorption and desorption isotherms of ZIF-8 at 77 K.

### 4. Thermal stability of ZIF-8 crystals

The thermogravimetric analysis of the synthesized ZIF-8 crystals via the RDF is in accordance with the one reported in the literature, since it is stable at a temperature up to 500 °C. Two minor weight losses (less than 5%) at 100 °C and 200 °C are observed in the TG curve shown in Figure 16. The first one is attributed to the loss of

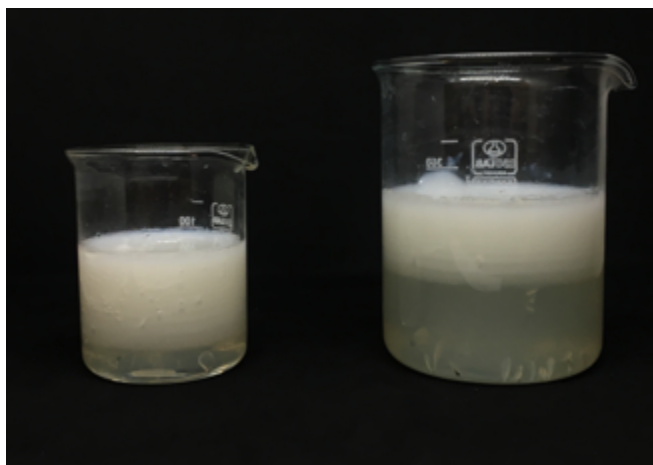
adsorbed water whereas the second one corresponds to the unreacted species and the remaining DMF.



**Figure 16:** Thermogravimetric curve of ZIF-8 under nitrogen atmosphere with a heating rate of  $5\text{ }^{\circ}\text{C}\cdot\text{min}^{-1}$  and a temperature between  $30\text{ }^{\circ}\text{C}$  and  $1100\text{ }^{\circ}\text{C}$ .

### 5. Yield of ZIF-8 crystals via RDF

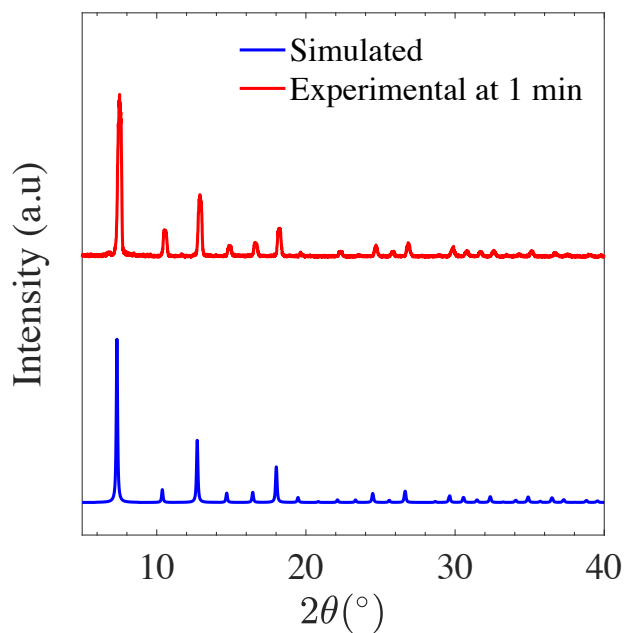
One of the major issues in material synthesis is the scalability. Indeed, it is a challenge to synthesize ZIF crystals in large scale in many of the conventional synthesis approaches. However, using RDF, ZIF-8 crystals are synthesized at different scales ranging from 20 mL in a test tube to reach the 300 mL in a beaker (Figure 17). These scales resulted in consistent crystals with no changes in the morphology or the quality. This is one of the advantages of RDF making it an interesting technique industrially.



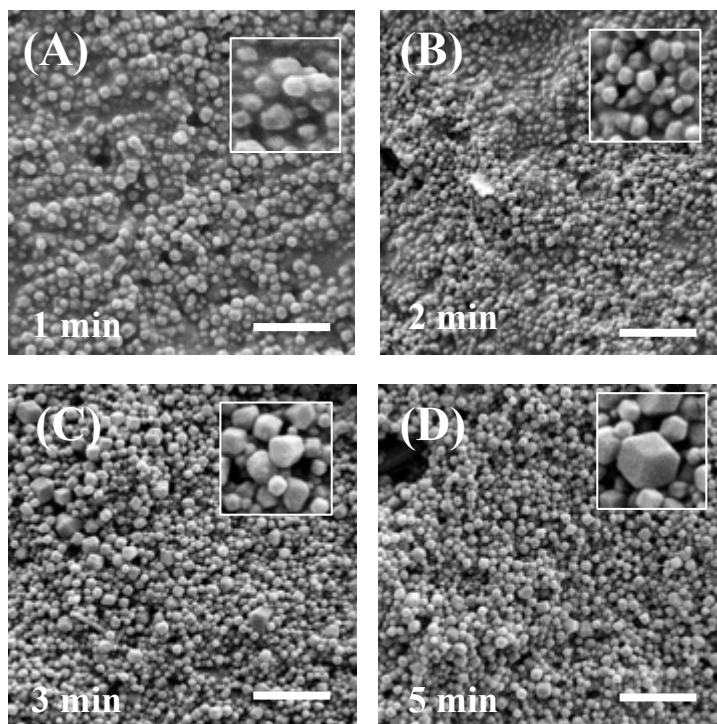
**Figure 17:** Preparation of ZIF-8 using the RDF process at different scales in larger volumes.

#### ***6. Kinetic study of the particle size evolution***

The reaction-diffusion framework (RDF) offers the ability to study the growth and the nucleation of the crystals. For this aim, four identical tubes are prepared with  $[\text{Zn}^{2+}] = 20.0 \text{ mM}$  as an inner solution,  $[\text{HmIm}] = 1.0 \text{ M}$  as an outer solution and 1 % agar gel at  $25 \text{ }^\circ\text{C}$ . The reaction is stopped by discarding the outer solution after a fixed period of time: 1 minute, 2 minutes, 3 minutes and 5 minutes of diffusion/reaction, then the white precipitates are collected from each tube. For the first minute of diffusion, a PXRD is carried out to identify the white powder (Figure 18). The morphology and the size of the particles are examined using the SEM (Figure 19) where at the first minute spherical ZIF-8 particles are formed. The transition from spheres to polyhedra is observed at the third minute. This indicates that the rate of formation of polyhedral ZIF-8 is quite fast unlike the slow rate of formation observed in the solvothermal technique where ZIF-8 particles appear after 24 hours [26].



**Figure 18:** PXRD patterns of the simulated ZIF-8 crystals and the synthesized ZIF-8 via RDF after 1 min of diffusion.



**Figure 19:** SEM images showing the kinetics of growth of ZIF-8 at different times: (A) 1 minute, (B) 2 minutes, (C) 3 minutes and (D) 5 minutes with zoomed in (inset) image showing the morphologies. The scale bar is  $2 \mu\text{m}$ .

## 7. Liesegang laws

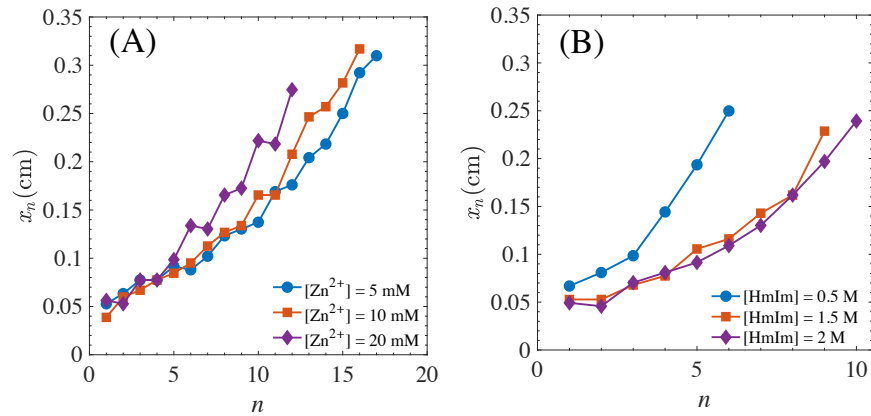
The different scaling laws characteristic of the Liesegang banding phenomenon described in Chapter 1 are investigated in this section. The measurements of the position ( $x_n$ ) and the width ( $w_n$ ) of each band are carried out using Adobe Photoshop.

### a. Spacing Law

The effect of the concentrations of the metal ions and the organic linker on the spacing of the Liesegang bands in this system is studied. Figure 20 shows the plot of the band position  $x_n$  versus the band number  $n$  for different inner  $[\text{Zn}^{2+}]$  and outer  $[\text{HmIm}]$  indicating a direct spacing system. The reported values of the spacing coefficient  $p$  (eq. 1) is extracted from the slopes of the linear plots of  $x_{n+1}$  versus  $x_n$ . For this system,  $p$  ranges from 0.11 to 0.15 (Table 2). For different inner  $[\text{Zn}^{2+}]$  and constant outer  $[\text{HmIm}]=1.0$  M, the spacing coefficient increases with the increase of the inner concentration. On the other hand, for different outer concentrations and constant inner  $[\text{Zn}^{2+}]$ , the spacing coefficient decreases with the increase of the outer concentration as in most of the cases [123]. Note that the near-overlap of the orange and violet curves in Figure 20. (B) is due to the closeness of the outer electrolyte concentrations.

**Table 2:** The spacing coefficient  $p$  calculated at different inner ( $[\text{Zn}^{2+}]$ ) and outer concentrations ( $[\text{HmIm}]$ ) for the ZIF-8 system.

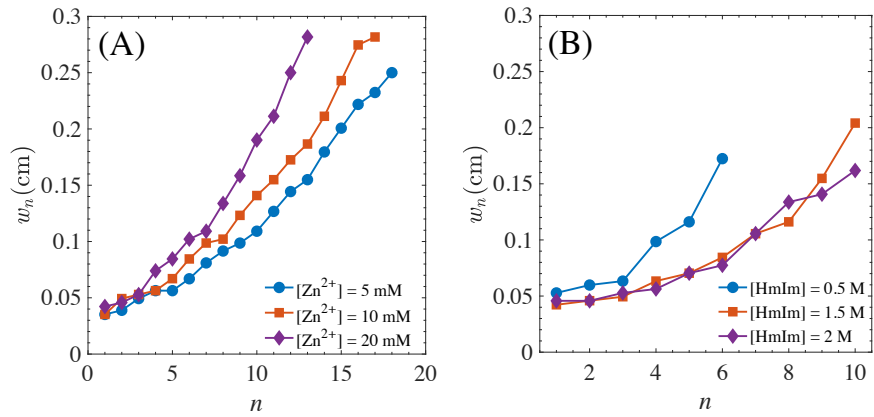
$p$			
Inner concentrations ( $[\text{Zn}^{2+}]$ )		Outer concentrations ( $[\text{HmIm}]$ )	
5 mM	0.114(6)	0.5 M	0.327(2)
10 mM	0.128(7)	1.5 M	0.203(3)
20 mM	0.153(4)	2 M	0.206(8)



**Figure 20:** Plot of the band position  $x_n$  versus its number  $n$  displaying direct spacing in the ZIF-8 precipitation system at (A) different inner concentrations and (B) different outer concentrations.

b. Width Law

The width  $w_n$  of each band is also measured and plotted versus its number  $n$  for different inner  $[Zn^{2+}]$  and outer  $[HmIm]$  (Figure 21). Furthermore, the width coefficient  $q$  is calculated as the slope of the plot of  $w_{n+1}$  versus  $w_n$ . The values of  $q$  reported in Table 3 follow the same trend as the spacing coefficient  $p$ . Hence,  $q$  essentially increases with the increase of the inner concentration at fixed outer  $[HmIm] = 1.0$  M and decreases with the increase of the outer concentration at fixed inner  $[Zn^{2+}] = 20.0$  mM. Note that the near-overlap of the orange and violet curves in Figure 21 (B) is due to the closeness of the outer electrolyte concentrations.



**Figure 21:** The width  $w_n$  of the consecutive bands plotted versus their number  $n$  in the ZIF-8 precipitation system at (A) different inner concentrations and (B) different outer concentrations.

**Table 3:** The width coefficient  $q$  calculated at different inner ( $[Zn^{2+}]$ ) and outer concentrations ( $[HmIm]$ ) for the ZIF-8 system.

$q$			
Inner concentrations ( $[Zn^{2+}]$ )		Outer concentrations ( $[HmIm]$ )	
5 mM	1.065 (6)	0.5 M	1.568 (4)
10 mM	1.061 (5)	1.5 M	1.375 (3)
20 mM	1.130 (3)	2 M	1.133 (6)

Moreover, the ln-ln plots of the width of each band  $w_n$  versus its position  $x_n$  exhibit linear correlation with values of the exponent  $\alpha$  (eq. 3) extracted as slopes from these plots (Table 4).

**Table 4:** The width exponent  $\alpha$  for different inner and outer concentrations.

	Inner concentrations ( $[Zn^{2+}]$ )			Outer concentrations ( $[HmIm]$ )		
	5 mM	10 mM	20 mM	0.5 M	1.5 M	2 M
$\alpha$	1.10 (6)	1.10 (9)	1.50 (9)	1.70 (6)	1.30 (6)	1.30 (8)
$R^2$	0.992	0.994	0.993	0.994	0.990	0.995



c. Matalon-Packter law

The Matalon-Packter law is also investigated for the ZIF-8 system.  $F(b_0)$  defined as the y-intercept function of the  $p$  versus  $(\frac{1}{a_0})$  is essentially an increasing function of  $b_0$  and  $G(b_0)$ , defined as the slope of this curve is also an increasing function of  $b_0$ .

**Table 5:** Values of the functions  $G(b_0)$  and  $F(b_0)$  for different initial inner concentrations  $b_0$ .

$b_0 = [\text{Zn}^{2+}]$	$G(b_0)$	$F(b_0)$
5 mM	0.030 (4)	0.116 (5)
10 mM	0.022 (5)	0.153 (8)
20 mM	0.075 (4)	0.186 (5)
30 mM	0.072 (7)	0.201(2)

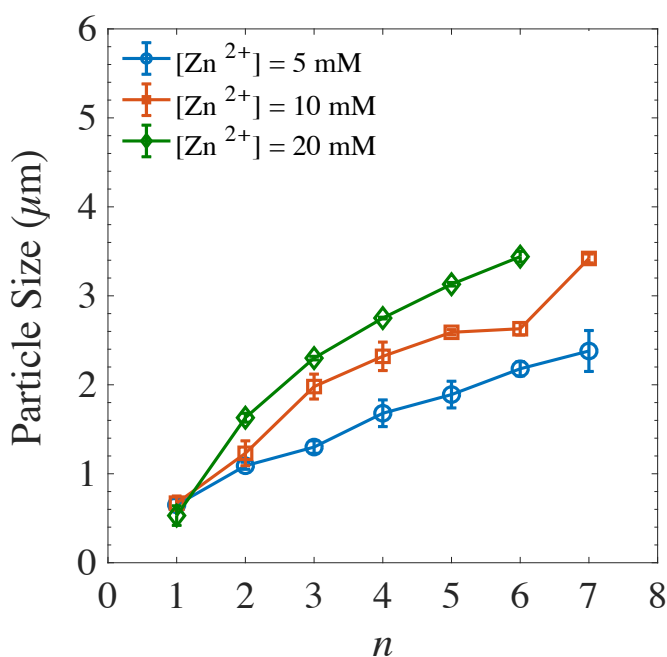
**8. Size and Morphology of ZIF-8 Crystals**

Among the various advantages of the RDF, the control of the particle size is considered the most important one, since the size of the particles is essential in many applications. Different experimental parameters including the concentrations of the metal ions and the organic linker, the agar percentage and the temperature are changed in order to study their effect on the size and the morphology of ZIF-8 crystals.

a. Effect of the inner concentration  $[\text{Zn}^{2+}]$

In order to study the effect of metal ion concentration, ZIF-8 crystals are synthesized with three different  $[\text{Zn}^{2+}]$  (5.0 mM, 10.0 mM and 20.0 mM) at room temperature (temp = 25 °C) with 1 M as the concentration of the organic linker [HmIm] and 1 % as the agar percentage. The bands are collected as adjacent regions of 0.5 cm width. It is shown in Figure 22 that upon the measurements using SEM, the average

particle size of the obtained ZIF-8 crystals increases with the increase of the inner  $[\text{Zn}^{2+}]$ . For example, at 3 cm from the interface, for the lowest inner concentration ( $[\text{Zn}^{2+}] = 5.0 \text{ mM}$ ) the average particle size is  $\sim 2 \mu\text{m}$  whereas at the highest concentration ( $[\text{Zn}^{2+}] = 20.0 \text{ mM}$ ) the average particle size is  $\sim 4.4 \mu\text{m}$ . This trend is a characteristic of the reaction-diffusion where the increase of the inner concentration will lead to an increase in the initial supersaturation gradient. Moreover, it is noteworthy that with the increase of the inner concentration, the morphology of the crystals does not change. The morphology of the particles in each band is recorded using the SEM and shown in Table S1.

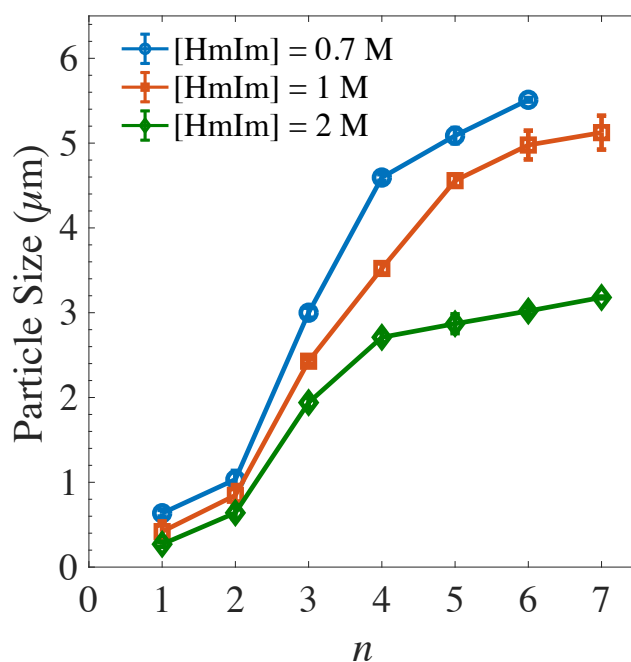


**Figure 22:** Particle size of ZIF-8 crystals at different inner  $[\text{Zn}^{2+}]$ .

b. Effect of the outer concentration  $[\text{HmIm}]$

The concentration of the organic linker is varied using three different values (0.7 M, 1.0 M and 2.0 M) whereas the concentration of the inner solution, the agar percentage and the temperature are kept constant at  $[\text{Zn}^{2+}] = 20.0 \text{ mM}$ , 1 % agar and 25

°C for the three different outer concentrations, respectively. The average particle size is shown in Figure 23 where smaller particles are obtained at higher outer [HmIm]. For the highest outer concentration ([HmIm] = 2.0 M), at 3 cm from the interface, particles of ~2.8  $\mu\text{m}$  are obtained whereas at the lowest concentration ([HmIm] = 0.7 M) polyhedra of ~5.6  $\mu\text{m}$  are formed. This is due to the supersaturation gradient, where for high outer concentrations the supersaturation gradient decreases leading to a decrease in the particle size. Furthermore, the morphology of the particles recorded using SEM is reported in Table S2 where as we go far from the interface simultaneously with the increase of their sizes, the surface of the particles becomes gradually rich in cavities.

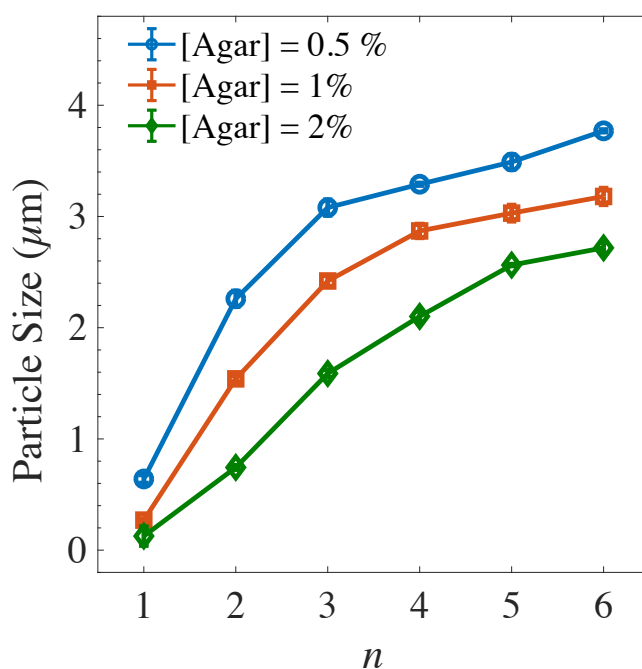


**Figure 23:** Particle size of ZIF-8 crystals at different outer [HmIm].

c. Effect of the Agar percentage

The concentration of the agar plays a major role in the nucleation and growth of the particles. For fixed inner and outer concentrations ( $[\text{Zn}^{2+}] = 20.0 \text{ mM}$  and

[HmIm]=1.0 M, respectively) and temperature (25 °C), different percentages of agar are used (0.5 %, 1 %, 1.5 % and 2 %). When the percentage of agar increases, the average pore size of the agar decreases, which leads to an increase in the number of nucleation sites, resulting in a decrease in the average particle size (Figure 24) [136]. The average particle size at the 4<sup>th</sup> band for 0.5 % agar is ~3.2 μm, it decreases to ~2.8 μm at 1 % agar and reaches ~2 μm at 2 % agar. The SEM images in Table S3 show a formation of polyhedra shaped crystals in all the bands and at different agar percentages with an augmentation of the cavities when the bands are at further positions from the interface.

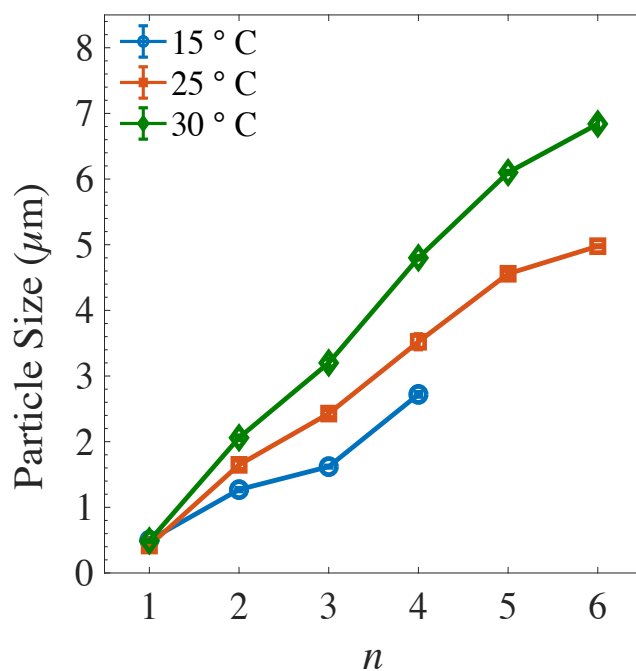


**Figure 24:** Particle size of ZIF-8 crystals at different agar percentages.

d. Effect of temperature

ZIF-8 crystals are synthesized at different temperatures (15 °C, 25 °C and 30 °C) while keeping the concentrations of the inner electrolyte, the outer electrolyte and the agar constant ([Zn<sup>2+</sup>] = 20.0 mM, [HmIm] = 1.5 M and 1 % agar, respectively). The

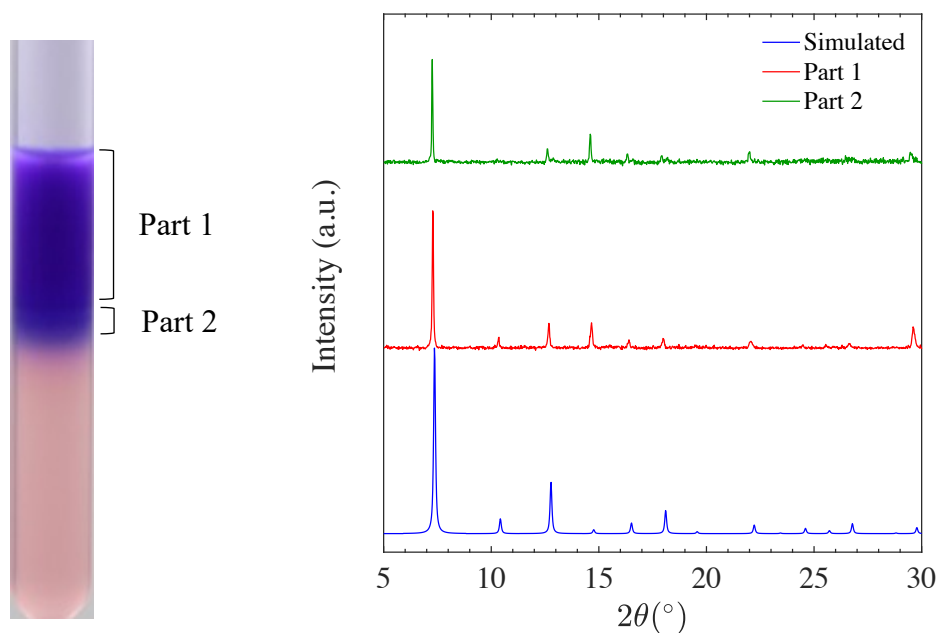
increase of the temperature is accompanied by an increase in the average size of the particles as shown in Figure 25. This trend is due to the increase of the rate of crystal growth leading to an increase in the particle size. This is clearly observed at the lowest temperature (15 °C) where only four bands (2 cm) are obtained for the same period of reaction time. However, at 30 °C six bands (3 cm) are obtained with the biggest particles (~7  $\mu\text{m}$  in the last band) compared to ~2.5  $\mu\text{m}$  at 15 °C. The SEM images of the three different tubes are represented in Table S4 showing no changes in the morphology of the particles.



**Figure 25:** Particle size of ZIF-8 crystals at different temperatures.

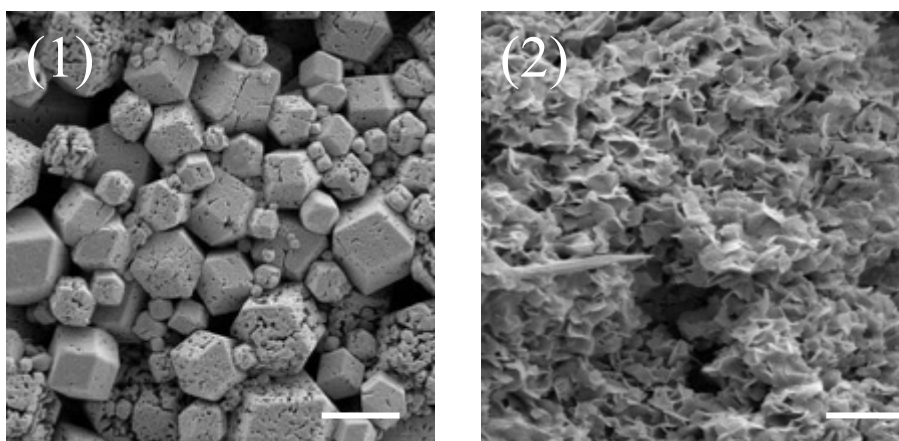
## 9. Characterization of ZIF-67

The two purple precipitates (Figure 7) obtained when replacing zinc ions by cobalt ions are subjected to PXRD for the identification. The PXRD patterns of both parts reveal that the purple powders are formed of ZIF-67 particles. Figure 26 shows no additional peaks nor differences between the simulated PXRD of ZIF-67 and the synthesized one.



**Figure 26:** PXRD patterns of the simulated ZIF-67 and the synthesized one (part 1 and 2).

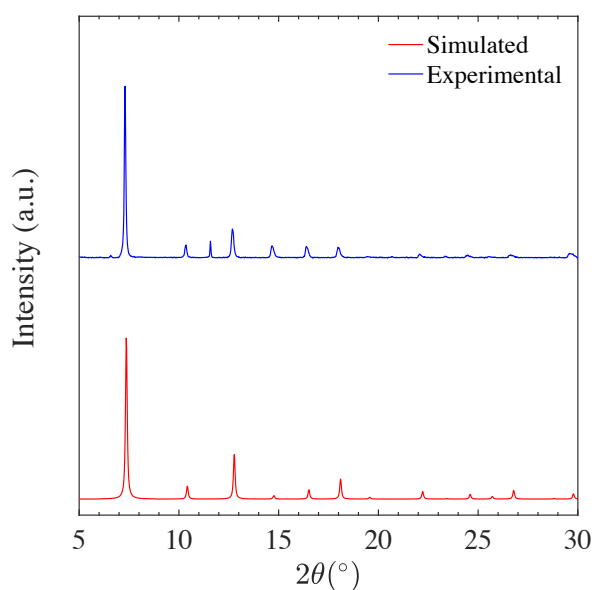
However, two different morphologies are observed when the powders are examined using the SEM. For the upper part of the tube, designated as part 1, polyhedral particles of  $\sim 5 \mu\text{m}$  diameter are formed, while the lower part, referred as part 2 is formed of sheets-like particles of similar size (Figure 27). Both morphologies are in accordance with the one found in literature [137].



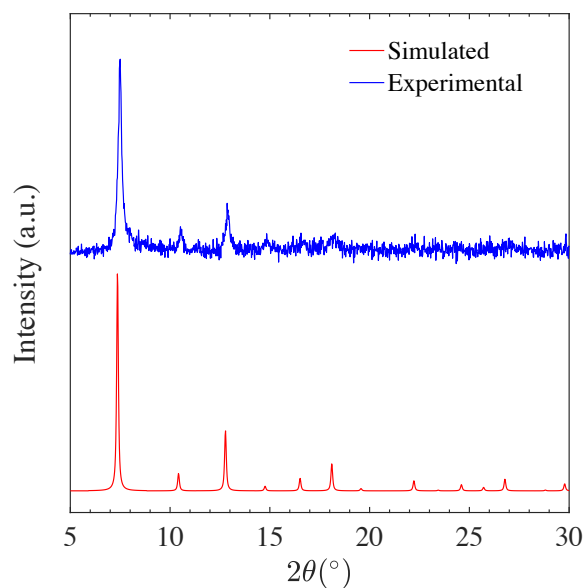
**Figure 27:** SEM images of ZIF-67 prepared at  $[\text{Co}^{2+}] = 20 \text{ mM}$  as an inner solution,  $[\text{HmIm}] = 1 \text{ M}$  as an outer solution and 1 % agar gel at  $25 \text{ }^\circ \text{C}$ . (1) part 1 and (2) part 2. The scale bar is  $5 \text{ }\mu\text{m}$ .

### 10. Mixture of the Two Metal Ions: $\text{Zn}^{2+}$ and $\text{Co}^{2+}$

Similar to all of the synthesized powders, the ones formed of mixed metal ions are subjected to PXRD. The PXRD patterns for the preparations of 5 % Co and 5 % Zn initial inner solutions revealed that the powders are formed of ZIF-8 and ZIF-67 respectively (Figure 28 and Figure 29).

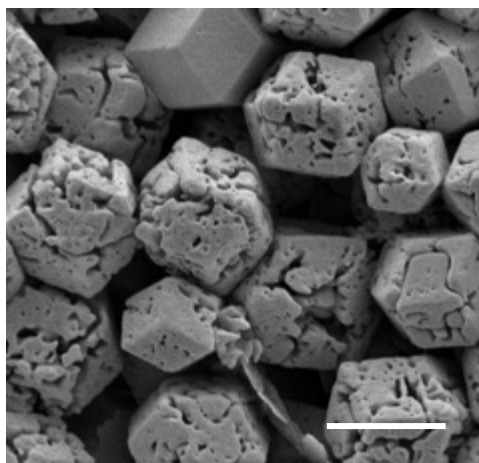


**Figure 28:** PXRD patterns of the simulated ZIF-8 and the 5 % Co-doped ZIF-8.



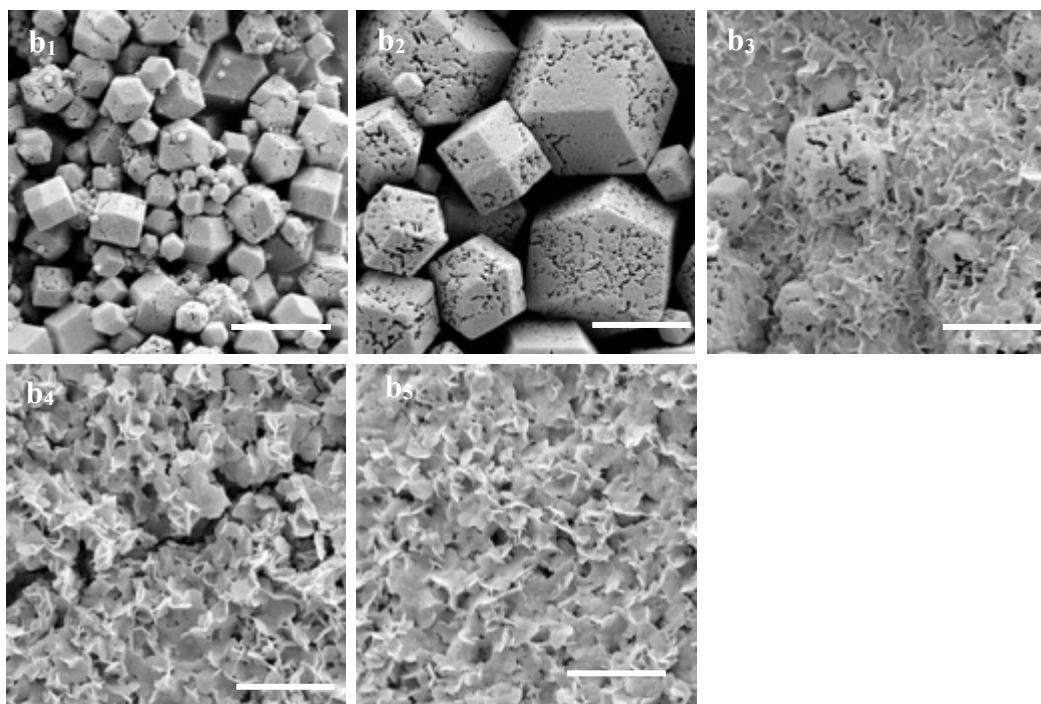
**Figure 29:** PXRD patterns of the simulated ZIF-67 and the 5 % Zn-doped ZIF-67.

The SEM images for the 5 % Co-doped ZIF-8 show polyhedral particles (Figure 30). Moreover, for the 5 % Zn-doped ZIF-67, the first two bands near the interface, taken as consecutive regions of 0.5 cm each, are formed as polyhedra of  $\sim 1 \mu\text{m}$ . However, the following consecutive three bands are formed of sheet-like particles of similar size (Figure 31). This morphology is similarly observed with the pure ZIF-67 as mentioned previously.



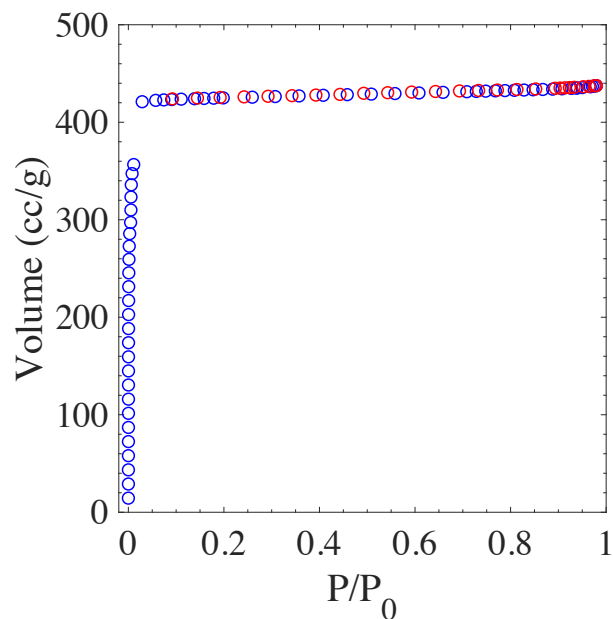
**Figure 30:** SEM image of 5 % Co doped ZIF-8 prepared at  $[\text{Zn}^{2+}/\text{Co}^{2+}] = 20 \text{ mM}$  as an inner solution,  $[\text{HmIm}] = 1 \text{ M}$  as an outer solution and 1 % agar gel at 25 °C. The scale bar is 2  $\mu\text{m}$ .





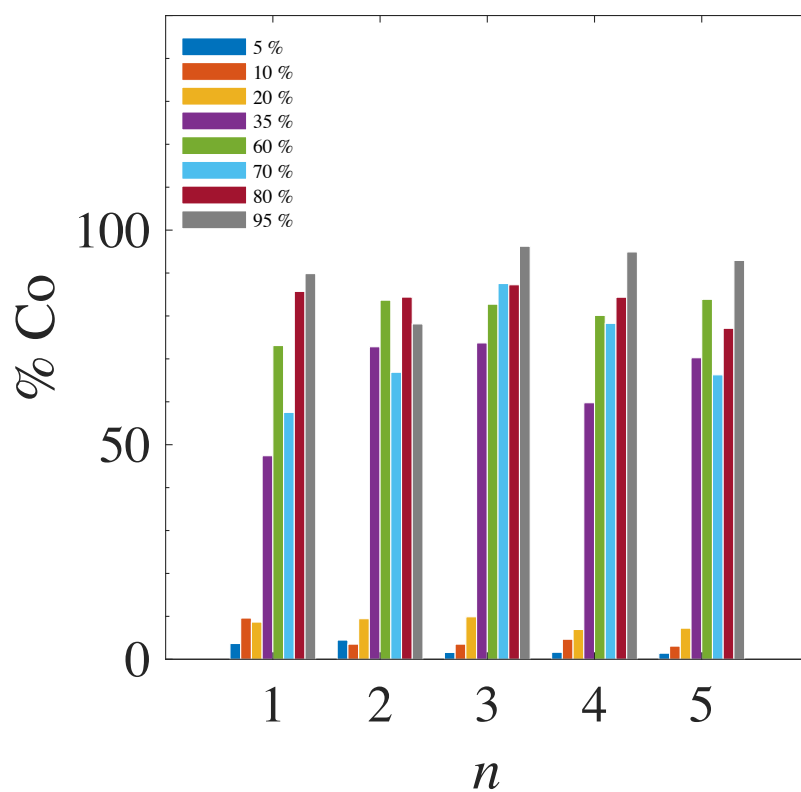
**Figure 31:** SEM images of 5 consecutive bands of the 5 % Zn-doped ZIF-67 prepared at  $[Zn^{2+}/Co^{2+}] = 20$  mM as an inner solution,  $[HmIm] = 1$  M as an outer solution and 1 % agar gel at 25 °C. The scale bar is 1  $\mu$ m.

The similarities in the PXRD patterns as well as the morphology and the size of the particles examined by SEM explain why doping the initial solution with a different metal will not induce any morphological or structural changes within the particles. Nevertheless, it might induce improvements in some of its properties. This is proved by the increase in the value of the BET surface area (ca. 1778  $m^2/g$ ) of the 5 % Co doped ZIF-8 compared to the one of the pure ZIF-8 (ca.1424  $m^2/g$ ). The  $N_2$  isotherms of 5 % Co doped ZIF-8 shown in Figure 32 is a Type I isotherm like the one of ZIF-8.



**Figure 32:** N<sub>2</sub> adsorption and desorption isotherm of 5 % Co doped ZIF-8 at 77 K.

In order to determine the final metal composition in each band, atomic absorption analysis is conducted. The AA measurements of five consecutive bands in each tube having different percentages of cobalt revealed that the cobalt cations are equally distributed along the tube. For example, for the 20 % Co doped ZIF-8 the final percentage of cobalt fluctuates between 7 % and 10 %. In most of the tubes, the percentage of cobalt incorporated in the ZIF particles is close to the initial prepared percentages, with no significant differences between the consecutive bands (Figure 33).



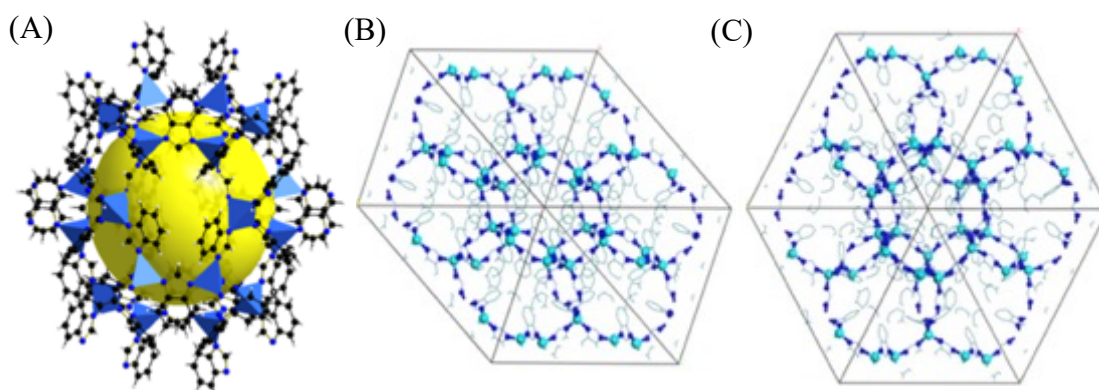
**Figure 33:** Atomic percentage of cobalt incorporation in ZIF-8 particles measured via AA for different initial ratios of  $\text{Co}^{2+}$  in 5 consecutive bands of the tubes.

## CHAPTER IV

### SYNTHESIS AND CHARACTERIZATION OF ZIF-7 VIA THE REACTION-DIFFUSION FRAMEWORK

#### A. Introduction

Zeolitic imidazolate framework-7 (ZIF-7) is another well studied ZIF material. First discovered by Park et al, ZIF-7 is formed by the coordination of the zinc ions ( $\text{Zn}^{2+}$ ) with the benzimidazolate linker [10]. Each zinc ion is tetrahedrally coordinated by four nitrogen atoms from the benzimidazolate building block. The first attempt to synthesize ZIF-7 crystals was done solvothermally in DMF at 130 °C [138]. Unlike ZIF-8, ZIF-7 exhibits a rhombohedral sodalite topology with two distinctive six-membered rings and one type of four-membered ring. The six-membered rings of the structure form two types of cavities identified as the preferred adsorption sites for the guest molecules (Figure 34) [139, 140]. Moreover, ZIF-7 has smaller pore windows (2.9 Å). Therefore, ZIF-7 is considered an important material in the separation process of a mixture of gases [141, 142]. In addition, ZIF-7 is considered the only ZIF with ZIF-9 that exhibits a phase change from its narrow-pore (np) phase to a large-pore (lp) phase upon heating in the absence of any guest molecules (Figure 34)[139].



**Figure 34:** (A) The crystal structure of ZIF-7. The blue tetrahedra represents the  $ZnN_4$  tetrahedra and the yellow sphere represents the space in the ZIF-7 cage with the two structures predicted by the molecular dynamics showing (B) the narrow-pore phase and (C) the large-pore phase. Reprinted with the permission of ref [138]. Copyright 2015 American Chemical Society and with permission of ref [137]. Copyright 2016 Processes.

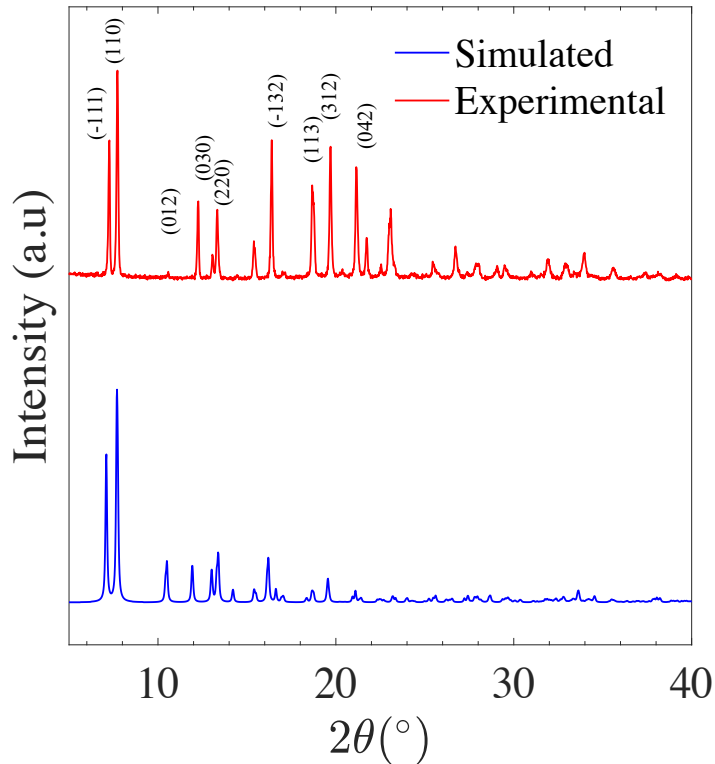
Like other ZIFs, ZIF-7 was synthesized by the traditional synthesis techniques including the solvothermal technique, the microwave assisted technique and many others. In the upcoming section, we will discuss the successful synthesis of ZIF-7 particles at room temperature using RDF. The characterization of the obtained powder using PXRD, SEM, BET and TGA will be also discussed. Finally, we will investigate the effect of different reaction parameters (zinc ions concentrations, benzimidazole concentration, agar percentages and temperature) on the size of the particles in addition to the various laws emerging from the Liesegang instability.

## B. Results and Discussion

### 1. Powder X-Ray Diffraction of ZIF-7 Crystals

The white precipitate is collected, washed and dried to be identified using the PXRD. The recorded patterns are compared to the calculated from the crystal structure (Figure 35). The perfect match of the locations of the main peaks at  $2\theta$ :  $7.14^\circ$  (-111),

7.68° (110), 12.07° (012), 13.33° (030), 15.41° (220), 16.27° (-132), 18.55° (113), 19.61° (312), 21.09° (042) and 22.91° (-243) indicates the high crystallinity and the phase purity of our ZIF-7 crystals.



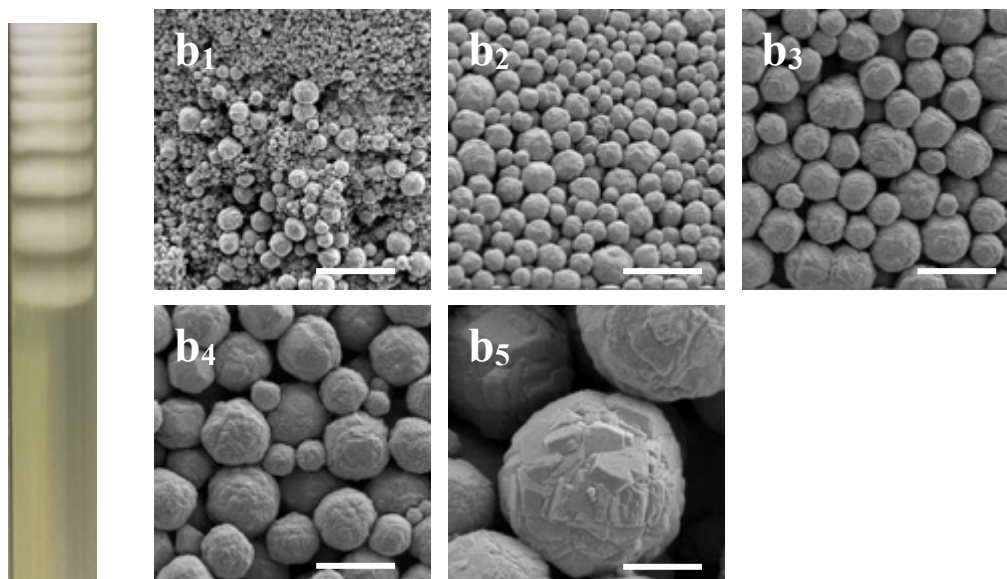
**Figure 35:** PXRD of the simulated ZIF-7 crystals and the synthesized ZIF-7 particles via RDF.

## 2. *Scanning Electron Microscopy Analysis and Particle Size Distribution of ZIF-7 Crystals.*

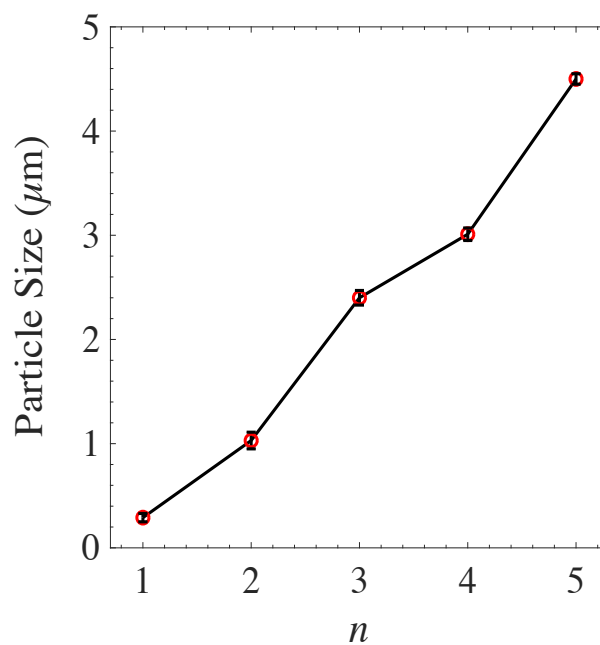
Contrarily to the Liesegang of the ZIF-8 system, the Liesegang banding phenomenon is well resolved in the ZIF-7 system, so the bands are separated individually. Five consecutive bands are separated from the same tube and the morphology of the ZIF-7 particles in each band is examined using the SEM (Figure 36). Spherical particles of an ascendant size are obtained as the position of the band is farther from interface along the tubular reactor (between 200 nm in the first band and 5

$\mu\text{m}$  in the fifth band). A similar trend of the ZIF-8 growth, which is characteristic of this synthesis technique is obtained for the ZIF-7 system.

(A)



(B)



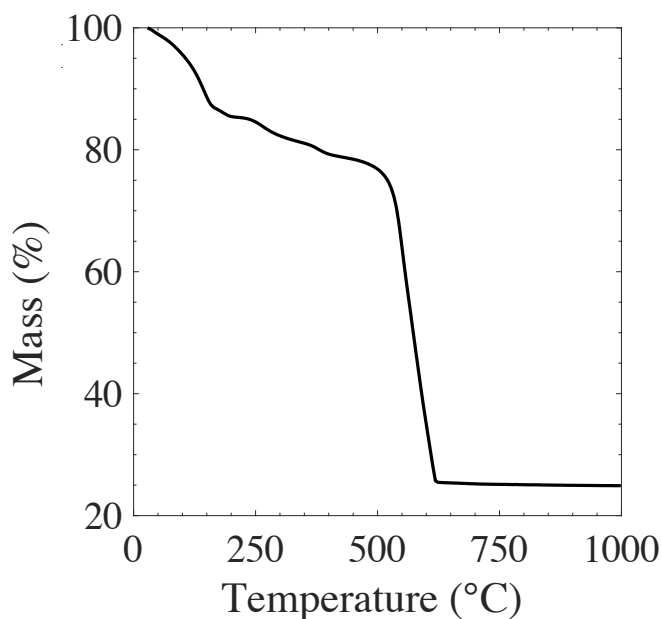
**Figure 36:** (A) SEM images showing ZIF-7 particles synthesized via RDF (the scale bar is 2  $\mu\text{m}$ ) and (B) a graph of the particle size growth over 5 consecutive bands.

### 3. BET Surface Area of ZIF-7 Crystals

In order to determine the surface area of ZIF-7 particles, N<sub>2</sub> uptake isotherm was measured at 77K. As expected, negligible amount of N<sub>2</sub> was adsorbed by ZIF-7 particles and the calculated surface area was found to be less than 10 m<sup>2</sup>/g. This is due to benzene rings located at the pore opening of ZIF-7 structure. This was also observed by Thompson *et al.* [143] where they proved that the inclusion of benzimidazole rings in the framework leads to a dramatic decrease in its surface area compared to ZIF-8.

### 4. Thermal Stability of ZIF-7 Crystals

The thermal stability of ZIF-7 is examined using the thermogravimetric analysis (TGA). The TGA curve in Figure 37 shows that the sample is stable up to 500 °C. Three major losses are observed in the curve. The first at 100 °C is attributed to the loss of adsorbed water, whereas the second one at 200 °C corresponds to the unreacted species and the remaining DMF in the pores and the destruction of the framework starts at 500 °C.

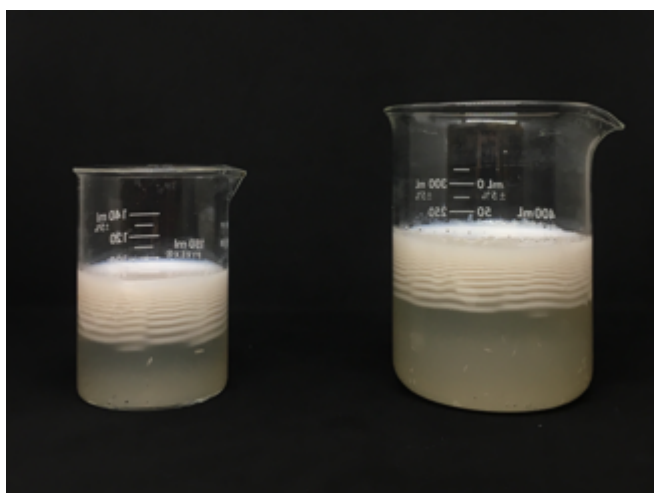


**Figure 37:** Thermogravimetric curves of ZIF-7 under nitrogen atmosphere with a heating rate of 5 °C. min<sup>-1</sup> and a temperature between 30 °C and 1000 °C.



### 5. Yield of ZIF-7 Crystals via RDF

ZIF-7 crystals are synthesized in large scales in addition to the synthesis in the test tubes. The similar Liesegang phenomenon is observed when going from a 15 mL solution in a test tube to a 300 mL beaker (Figure 38). Moreover, the structural and morphological features of the particles are preserved. This important result shows that RDF technique could be potentially used at the industrial level to produce large scale of ZIF materials.

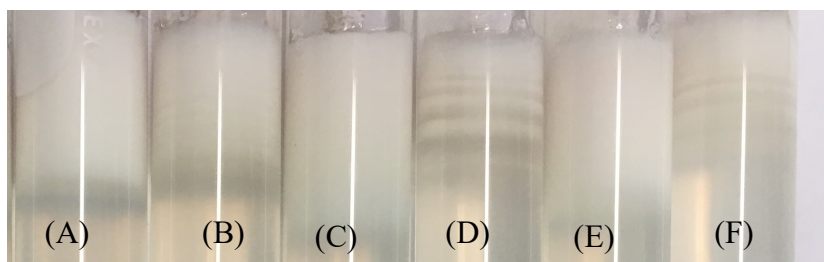


**Figure 38:** Preparation of ZIF-7 using the RDF process at different scales in larger volumes.

### 6. Effect of the Zinc Source and Solvent

Common zinc sources (zinc nitrate, bromide and chloride) are tested for the synthesis of ZIF-7 particles (Figure 39). Additionally, the reactions are performed in the absence and in the presence of DMF in the inner solution. However, in all cases, the organic linker in the outer solution is dissolved in an equivalent volume of water and DMF (1:1). By removing the DMF from the inner solution, our aim is to reach an environmentally friendly technique.

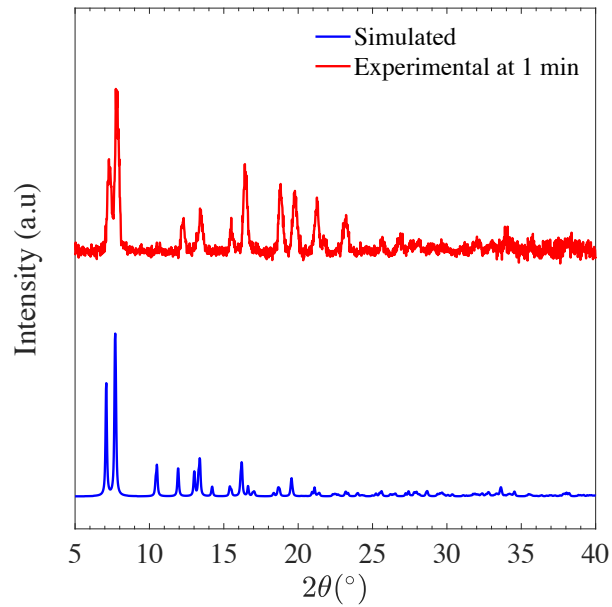
Interestingly, white precipitate is formed in all the tubes. It is collected and prepared for characterization and identification using the PXRD and SEM. The structural analysis of the powder reveals the formation of pure ZIF-7 in all tubes. Moreover, the morphology is not affected by these different experimental conditions (Figure S1 and S2 in the appendix). Nevertheless, Liesegang banding is only observed when the chloride and the bromide salts are used in the presence of DMF.



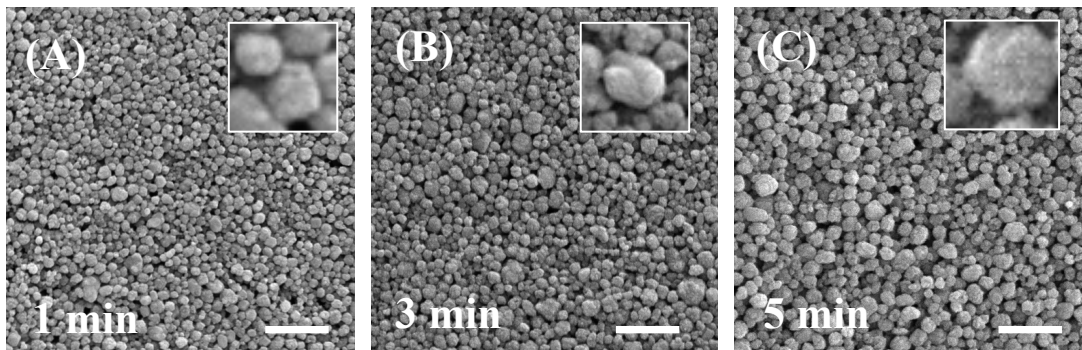
**Figure 39:** Synthesis of ZIF-7 using different zinc sources (A) nitrate in water, (B) nitrate in water and DMF, (C) chloride in water, (D) chloride in water and DMF, (E) bromide in water, (F) bromide in water and DMF.

### 7. *Kinetic Study on the Particle Size Evolution*

To follow the evolution of the nucleation and growth of ZIF-7 particles at a specific time, four identical tubes are prepared with  $[Zn^{2+}] = 20.0$  mM as an inner solution,  $[BenzIm] = 1.0$  M as an outer solution and 1 % agar gel at 25 ° C. After discarding the outer solution at a specific time (1 minute, 3 minutes and 5 minutes), the white precipitates are collected and prepared for characterization using PXRD and morphological examination using SEM. The PXRD patterns reveals that these white precipitates are formed of ZIF-7 particles (Figure 40). Moreover, the SEM micrographs in Figure 41 show that spheroids of 100 nm are obtained from the first minute to reach 500 nm after 5 minutes.



**Figure 40:** PXR D pattern of ZIF-7 particles at 1 min after the diffusion of the outer electrolyte.



**Figure 41:** SEM images showing the kinetic of growth of ZIF-7 at different times: (A) 1 minute, (B) 3 minutes and (C) 5 minutes with a zoomed in figure of the spheres (inset) .The scale bas is 1  $\mu\text{m}$ .

## 8. Liesegang laws

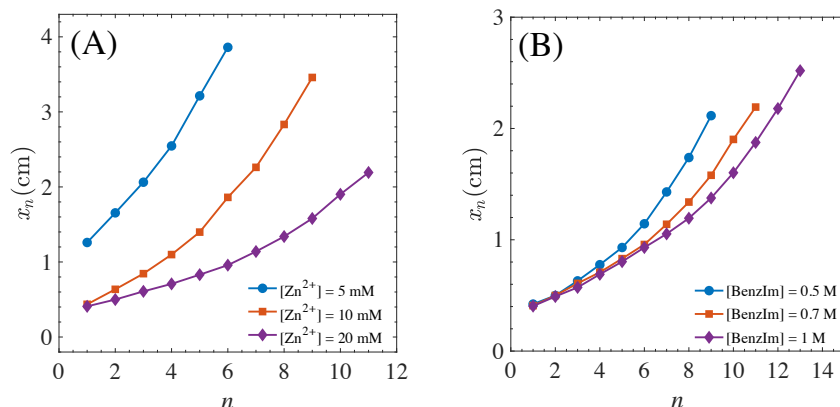
Using the Adobe Photoshop program, the positions  $x_n$  and the widths  $w_n$  of each band  $n$  are measured to verify the scaling laws governing the Liesegang banding phenomenon.

a. Spacing Law

The concentrations of the zinc ions and the benzimidazole solutions are changed to study their effect on the spacing of the consecutive bands for this system. The position  $x_n$  of each band for different inner and outer concentrations separately are plotted versus the band number  $n$  (Figure 42). These graphs show a direct spacing in the Liesegang phenomenon appearing in the ZIF-7 system. The reported values of the spacing coefficient  $p$  (eq. 1) are extracted from the slopes of the linear plots of  $x_{n+1}$  versus  $x_n$  and shown in Table 6. For different inner concentrations and constant outer concentration (0.7 M),  $p$  ranges between 0.16 and 0.18 with no trend following the increase of the inner concentrations. However, with the increase of the outer concentrations with constant inner concentration (20.0 mM)  $p$  decreases from 0.22 to 0.16.

**Table 6:** The spacing coefficient  $p$  at different inner concentrations ( $[\text{Zn}^{2+}]$ ) and different outer concentrations ( $[\text{BenzIm}]$ ).

$p$			
Inner concentrations $[\text{Zn}^{2+}]$		Outer concentrations $[\text{BenzIm}]$	
5 mM	0.155 (2)	0.5 M	0.219 (4)
10 mM	0.188 (4)	0.7 M	0.163 (7)
20 mM	0.163 (5)	1 M	0.154 (9)



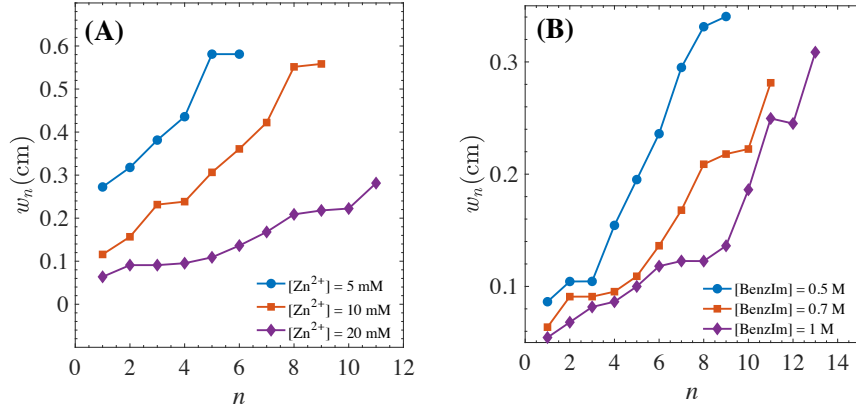
**Figure 42:** The position  $x_n$  of the consecutive bands plotted versus their number  $n$  showing the direct spacing in the ZIF-7 precipitation system for (A) for different  $[Zn^{2+}]$  and (B) different outer  $[BenzIm]$ .

b. Width Law

The width  $w_n$  of each band is also measured at different inner and outer concentrations. The width  $w_n$  of each band is plotted versus its number  $n$  (Figure 43) and the width coefficient  $q$  is calculated as the slope of the plots  $w_{n+1}$  versus  $w_n$ . The values of  $q$  are represented in Table 7. It is intriguing to realize that for different inner concentrations and a fixed outer concentration of 0.7 M,  $q$  decreases with the increase of the inner concentration, thus opposing the trend observed for ZIF-8. Whereas for different outer concentrations and a fixed inner of 20.0 mM, no clear trend is observed. Moreover, the ln-ln plots of the band width  $w_n$  versus its position  $x_n$  are plotted and the values of the slope  $\alpha$  are represented in Table 8.

**Table 7:** The width coefficient  $q$  at different inner concentrations ( $[Zn^{2+}]$ ) and different outer concentrations ( $[BenzIm]$ ).

$q$			
Inner concentrations $[Zn^{2+}]$		Outer concentrations $[BenzIm]$	
5 mM	1.523 (6)	0.5 M	1.125 (4)
10 mM	1.191 (7)	0.7 M	0.986 (8)
20 mM	0.986 (4)	1 M	1.370 (6)



**Figure 43:** The width  $w_n$  of the consecutive bands plotted versus their number  $n$  showing the direct spacing in the ZIF-7 precipitation system (A) for different  $[\text{Zn}^{2+}]$  and (B) different outer  $[\text{BenzIm}]$ .

**Table 8:** The width exponent  $\alpha$  for different inner and outer concentrations.

	Inner concentrations $[\text{Zn}^{2+}]$			Outer concentrations $[\text{BenzIm}]$		
	5 mM	10 mM	20 mM	0.5 M	0.7 M	1 M
$\alpha$	0.741 (3)	0.774 (2)	0.867(4)	0.946 (5)	0.853 (5)	0.781 (9)
$R^2$	0.975	0.985	0.966	0.968	0.955	0.965

c. Matalon-Packter law

The spacing coefficient  $p$  is plotted versus the inverse of the outer concentrations ( $\frac{1}{a_0}$ ) for three different inner concentrations  $b_0$ . According to the Matalon-Packter law, the  $F(b_0)$  and  $G(b_0)$  functions are calculated as the y-intercept and the slope of the plot, respectively. The corresponding values of  $G(b_0)$  and  $F(b_0)$  presented in Table 9 show that the first one is a decreasing function of  $b_0$  whereas the second one is an increasing function of  $b_0$ .

**Table 9:** Values of the functions  $G(b_0)$  and  $F(b_0)$  for different initial inner concentrations  $b_0$ .

$b_0 = [\text{Zn}^{2+}]$	$G(b_0)$	$F(b_0)$
5 mM	0.084 (1)	0.056 (3)
10 mM	0.028 (4)	0.148 (7)
30 mM	0.029 (4)	0.169 (6)

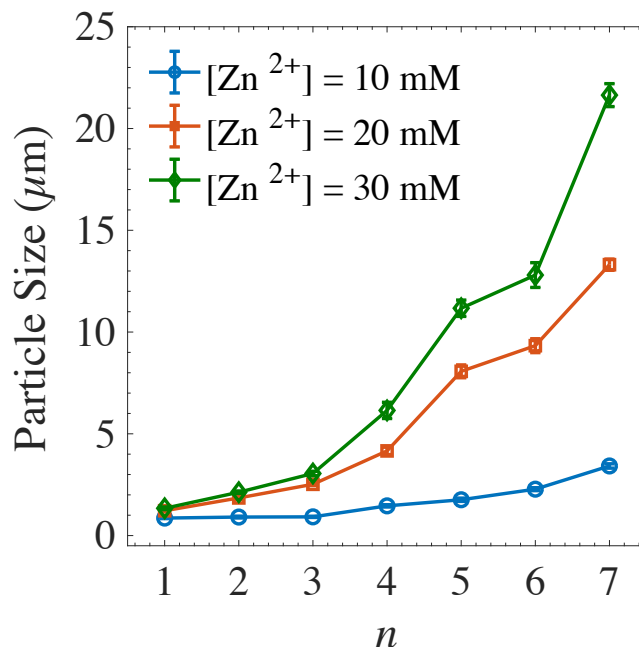
### 9. Size and Morphology of ZIF-7 Crystals

The control of particle size and morphologies is very important and challenging in material synthesis and applications. The conventional synthesis techniques lack from the ability to control the size of the particles synthesized. However, the Reaction-Diffusion framework allows us this control by varying different experimental conditions including the inner and the outer concentrations, the gel thickness and the temperature.

#### a. Effect of the inner concentration $[\text{Zn}^{2+}]$

The effect of the concentration of the zinc ions on the size of the particles is studied where for fixed agar percentage (1%), fixed outer concentration ( $[\text{BenzIm}] = 0.7$  M) and at a fixed temperature (25 °C), three tubes are prepared with three different inner concentrations  $[\text{Zn}^{2+}]$ . The SEM images (Table S5) of the crystals extracted from consecutive bands of the three different tubes show that the increase in the zinc ions concentrations is accompanied with an increase in the particle size (Figure 44). For example, for  $[\text{Zn}^{2+}] = 10.0$  mM at the fourth band, the particles are of 1.5  $\mu\text{m}$ . Whereas for  $[\text{Zn}^{2+}] = 20.0$  mM, the average diameter of the particles in the same band is  $\sim 4$   $\mu\text{m}$  and reach  $\sim 6$   $\mu\text{m}$  for  $[\text{Zn}^{2+}] = 30.0$  mM. This trend is explained by the increase of the

supersaturation with the increase of the inner concentration, yielding bigger particles with higher inner concentrations.



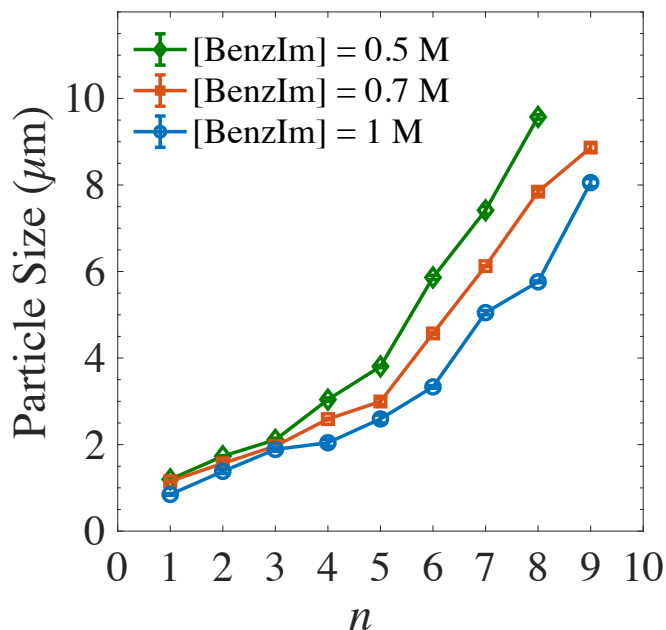
**Figure 44:** Particle size of ZIF-7 crystals at different inner [Zn<sup>2+</sup>].

b. Effect of the outer concentration [BenzIm]

The size of the ZIF-7 particles is also affected by the concentration of the organic linker for the same concentration of zinc ions [Zn<sup>2+</sup>] (the same agar percentage (1 %) and at the same temperature (25 °C)). Figure 45 shows that the particles are smaller when the concentration of the benzimidazole solution increases at fixed inner concentration. For example, for a concentration of 0.5 M, the average diameter of the particles at the 5<sup>th</sup> band is ~ 4 µm. For 0.7 M of benzimidazole, the average diameter of particles in the 5<sup>th</sup> band is ~3 µm. However, for 1.0 M of benzimidazole, the average diameter in the same band is ~2 µm. This trend is due to the decrease of the supersaturation gradient with the increase in the outer concentration at fixed inner



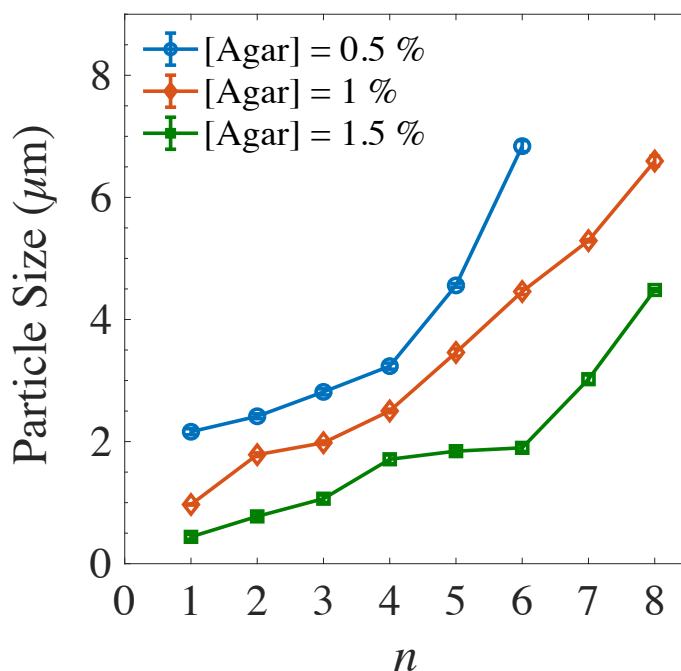
concentration. The SEM images of the different consecutive bands of each tube at different outer concentrations are reported in Table S6 in the appendix.



**Figure 45:** Particle size of ZIF-7 crystals at different outer [BenzIm].

c. Effect of the Agar percentage

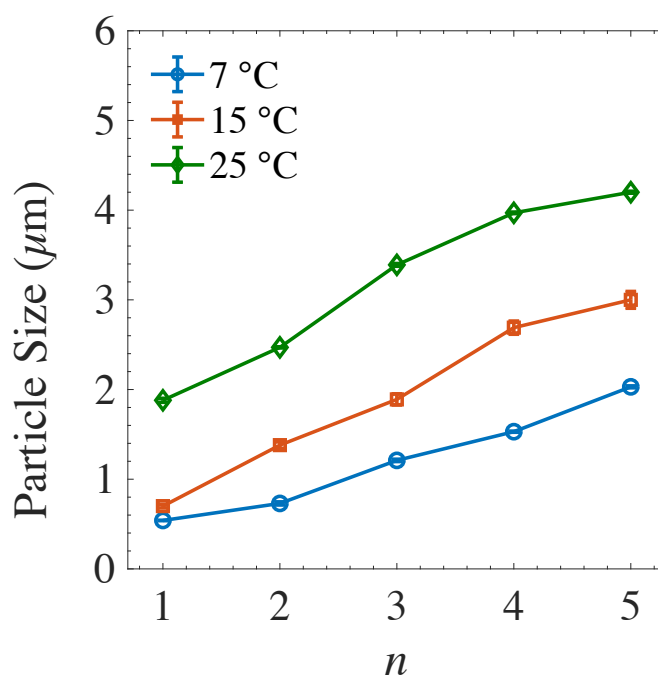
For fixed inner and outer concentrations,  $[Zn^{2+}] = 20.0$  mM and  $[BenzIm] = 1.0$  M respectively and at a constant temperature (temp = 25 °C), the percentage of agar is changed to study its effect on the particle size. Figure 46 shows that the increase in the agar percentage induces a decrease in the particle size within the same tubular reactor. For example, at 0.5 % the particles at the fifth bands are of 4.5 μm, at 1 % the size decreases to 3 μm and reaches 1.5 μm at 1.5 % of agar in the same bands. This trend might be due to the decrease of the average pore size of the agar followed by an increase in the nucleation sites. The SEM images of the consecutive bands for three different agar percentages are shown in Table S7.



**Figure 46:** Particle size of ZIF-7 crystals at different agar percentages.

d. Effect of Temperature

The effect of the temperature on the size of ZIF-7 particles is also investigated. Three different tubes with fixed inner concentration ( $[Zn^{2+}] = 20.0 \text{ mM}$ ), outer concentration ( $[BenzIm] = 1.0 \text{ M}$ ) and agar percentage (1 %) are prepared at three different temperatures ( $7 \text{ }^\circ\text{C}$ ,  $15 \text{ }^\circ\text{C}$  and  $25 \text{ }^\circ\text{C}$ ). The average particle size increases with the increase of the temperature as shown in Figure 47. When the temperature increases, the rate of crystal growth increases too, thus leading to an increase in the particle size. For example, at  $7 \text{ }^\circ\text{C}$  at the third band, particles of  $1.2 \text{ }\mu\text{m}$  are obtained and at  $15 \text{ }^\circ\text{C}$ , particles of  $1.8 \text{ }\mu\text{m}$  whereas at  $25 \text{ }^\circ\text{C}$  and at the same band particles of  $3.4 \text{ }\mu\text{m}$  are formed. Moreover, the SEM images shown in Table S8 demonstrate that the morphology of the particles is not affected by the temperature.



**Figure 47:** Particle size of ZIF-7 crystals at different temperatures.

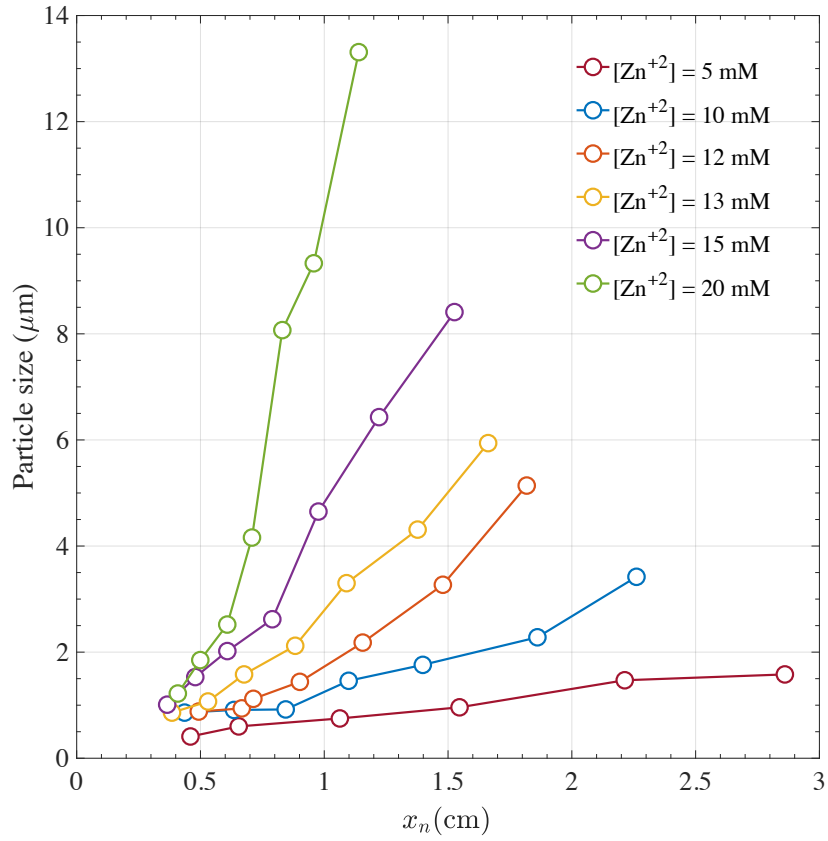
Finally, we can conclude that the concentration of the inner electrolyte has the most important effect on the particle size. In fact, the biggest particles are obtained when the concentration of the zinc ions reached 30 mM.

### 10. Size law

A new law relating the size of the particles in each band ( $s_n$ ) to its position ( $x_n$ ) is introduced. Six tubes with different inner concentrations ranging from 5 mM to 20 mM are prepared with a constant outer concentration of 0.7 M and the consecutive bands are extracted and washed to measure their particle size. The average particle size in each band is plotted versus the band position in Figure 48. The obtained plots clearly show an increase of the particle size  $s_n$  as a function of the position of the band  $x_n$  which can be fitted as a power law:

$$s_n \sim x_n^\sigma$$

where the exponent  $\sigma$  is extracted from the ln-ln plots of  $s_n$  versus  $x_n$ . Furthermore,  $\sigma$  increases with the inner concentration  $[\text{Zn}^{2+}]$  as shown in Table 10.

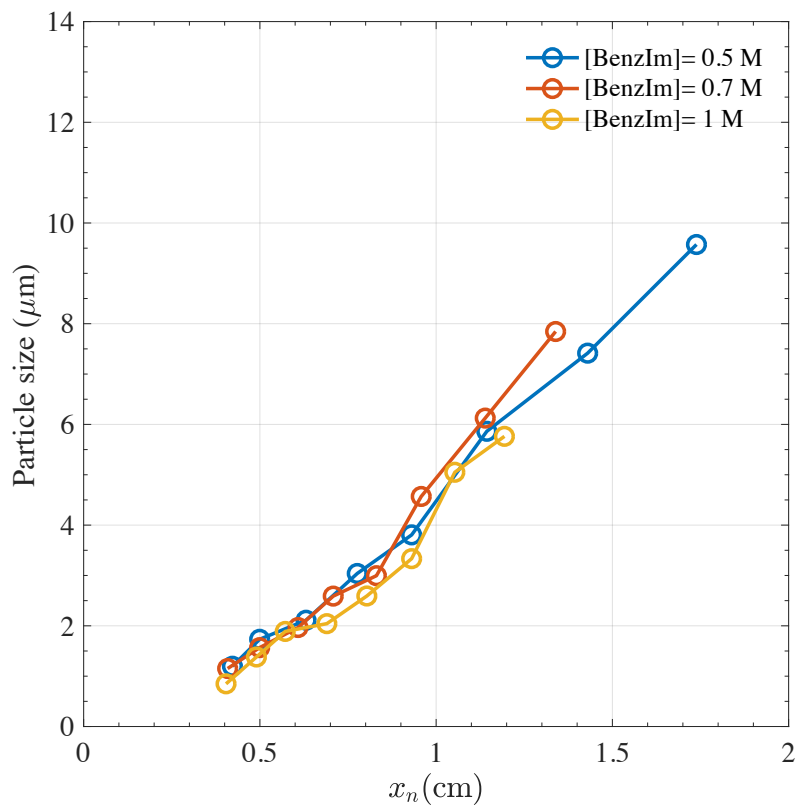


**Figure 48:** Particle size ( $\mu\text{m}$ ) versus the position of the bands  $x_n$  for different inner  $[\text{Zn}^{2+}]$ .

**Table 10:** The exponent  $\sigma$  extracted from the slopes of the ln-ln plots of the particle size versus its band position for different inner  $[\text{Zn}^{2+}]$ .

Inner $[\text{Zn}^{2+}]$						
	5 mM	10 mM	12 mM	13 mM	15 mM	20 mM
$\sigma$	0.73	0.85	1.41	1.37	1.51	2.46

Moreover, this law is also studied for different outer concentrations. Three different tubes of different outer concentrations ( $[\text{BenzIm}]$ ) of 0.5 M, 0.7 M and 1.0 M at constant inner concentration ( $[\text{Zn}^{2+}] = 20.0 \text{ mM}$ ) and 1 % agar are prepared. Similarly, the consecutive bands are collected after measuring their position  $x_n$ , and the average particle size  $s_n$  in each band is thereafter measured. The plots of  $s_n$  versus  $x_n$  are shown in Figure 49. Particularly, an overlap of the plots is observed for different outer concentrations ( $[\text{BenzIm}]$ ) at a constant inner concentration ( $[\text{Zn}^{2+}]$ ). The power exponents extracted from the ln-ln plots of  $s_n$  versus  $x_n$  do not show any significant change as a function of the outer concentration  $[\text{BenzIm}]$ . This is probably due to the fact that the outer concentration is in excess and what determines the final size is the limiting inner concentration.



**Figure 49:** Particle size ( $\mu\text{m}$ ) versus the position of the bands  $x_n$  for different outer  $[\text{BenzIm}]$ .

**Table 11:** The exponent  $\sigma$  extracted from the slopes of the ln-ln plots of the particle size versus its band position for different outer [BenzIm].

Outer [BenzIm]			
	0.5 M	0.7 M	1 M
$\sigma$	1.46	1.64	1.67

This size law is a direct consequence of the competition between the nonlinear rates of nucleation and growth of crystals resulting from a changing supersaturation gradient along the tube.

## CHAPTER V

### CONCLUSION AND FUTURE WORK

#### A. Conclusion

In this work, a novel method is used for the synthesis of zeolitic imidazolate frameworks (ZIFs). This method is based on the diffusion of an outer solution into an agar gel containing the inner solution where a precipitation reaction takes place leading to the formation of the ZIF crystals. This method is applied for the most studied ZIFs, ZIF-8, ZIF-7 and ZIF-67. The first one is formed of the tetrahedral coordination of the 2-methylimidazolate with zinc ions, whereas for ZIF-7, the 2-methylimidazolate rings are substituted by the benzimidazolate rings. However, ZIF-67 is formed of the coordination of cobalt ions with 2-methylimidazole. Remarkably, the non-linear coupling between the reaction and the diffusion with the nucleation and growth of the crystals results in the formation of Liesegang bands with direct spacing. This banding phenomenon is based on the formation of a series of alternating bands separated by precipitate free-zones. The alternative bands, formed of the crystals, are extracted and characterized using PXRD, SEM, BET and TGA.

The reaction-diffusion framework (RDF) allows us to control the size of the particles within the same tubular reactor. Different particle sizes are obtained within the same tube in each band of the Liesegang system. For this aim, different reaction parameters, including the concentration of the zinc ions, the concentrations of the organic linker, the agar percentage and the temperature, were changed for both systems to study their effect on the particle size and the morphology. Additionally, this

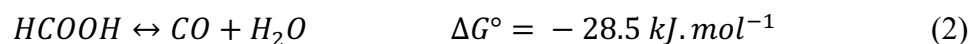
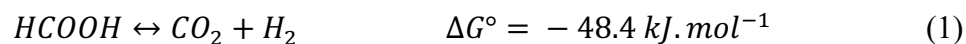
technique is applicable for big scales where ZIFs are obtained in large yields. By using the gel matrix, the kinetic of the growing particles is slowed down. Thus, we are able to monitor the transition from nuclei to complete crystals at different time scales.

Moreover, the scaling laws of this specific Liesegang system in ZIF-8 and ZIF-7, including the spacing law, the width law and the Matalon-Packter law, are determined, and their effect on the crystal size distribution is studied, in addition to the introduction of a new size law.

Furthermore, mixed metals ZIFs were also synthesized using RDF in a controlled manner. Different ratios of cobalt and zinc ions are used for the synthesis of Co-doped ZIF-8. The exact doping percentage in each band is determined using atomic absorption (AA).

## **B. Future Work**

After synthesizing the ZIF particles using this novel technique, a preliminary study was done in order to use them as a photocatalyst support of formic acid under UV-Vis irradiation (LC8 spot light Hamamatsu, L10852, 200 W) and in dark. The photo-decomposition of formic acid (FAc) leads to the formation of carbon dioxide or carbon monoxide, according to the two pathways:



Hydrogen is considered one of the most promising clean energy carriers.

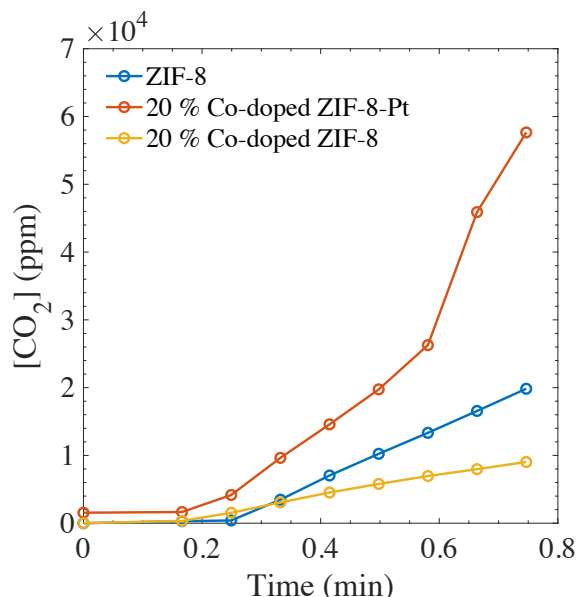
However, its use as carbon-free fuel source lacks from appropriate storage techniques



Recently, formic acid (HCOOH, FAc), a by-product of many chemical processes, is widely used for the production of hydrogen since it is nontoxic, liquid at room temperature and has high gravimetric (4.4 wt %) and volumetric (53.4 g/L) H<sub>2</sub> capacity making it a very promising liquid hydrogen carrier [144, 145].

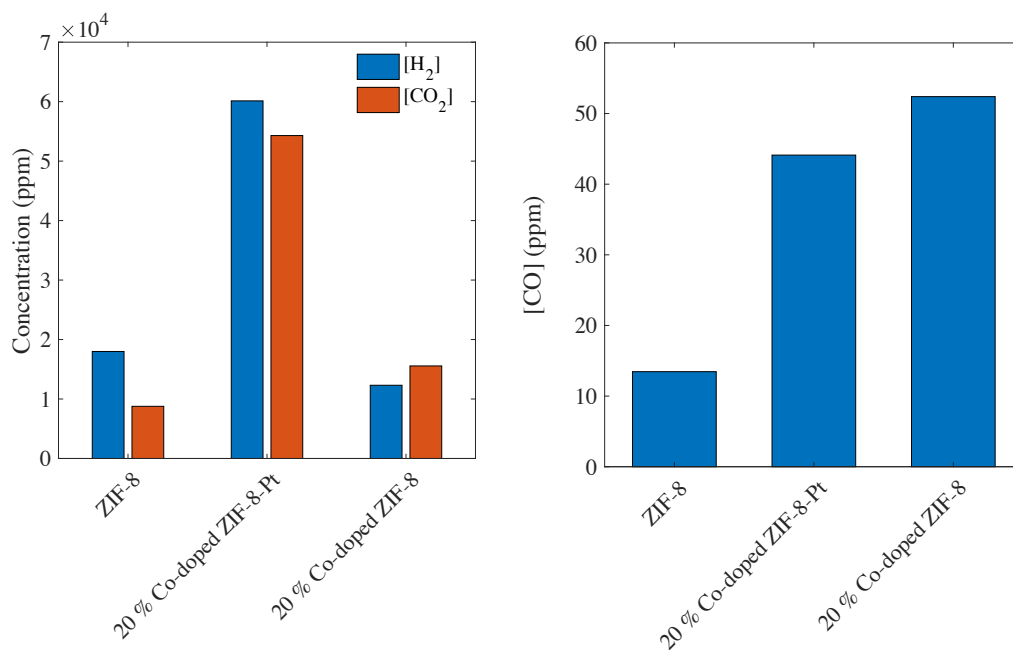
The CO<sub>2</sub> and CO evolutions during the photocatalytic splitting of FAc is monitored in real-time using a new in-situ FTIR reactor, while the amount of produced H<sub>2</sub> is determined using Gas Chromatography (GC).

The first results show that 20 % Co-doped ZIF-8 is more efficient than ZIF-8 holding the Pt metal. This indicates that doping with cobalt has a positive effect on the enhancement of the photocatalytic properties of ZIF-8 under this irradiation condition. This can be attributed to the higher visible light absorption by the doped version. Moreover, Pt plays an unfavorable role in the photocatalytic splitting of FAc as demonstrated in Figure 50. When the Pt is present the concentration of CO<sub>2</sub> decreases for the 20 % Co-doped ZIF-8.



**Figure 50:** The evolution of the of CO<sub>2</sub> concentration (ppm) versus irradiation time during the photocatalytic decomposition of FAc on ZIF-8, 20 % Co-doped ZIF-8 and 20 % Co-doped ZIF-8 as catalyst support for Pt .

The concentrations of CO<sub>2</sub>, H<sub>2</sub> and CO calculated for the four used samples are shown in Figure 51. The low amount of CO indicates that the photo-decomposition of formic acid in the presence of ZIF-8 and 20 % Co-doped ZIF-8 is directed towards the pathway (1).



**Figure 51:** Bar graphs showing the concentrations of CO<sub>2</sub>, H<sub>2</sub> and CO (in ppm) for different samples used.

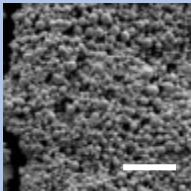
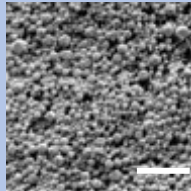
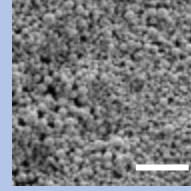
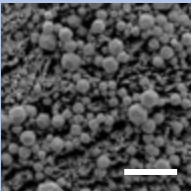
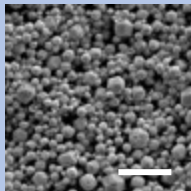
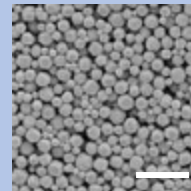
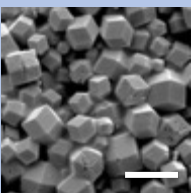
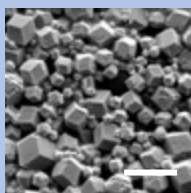
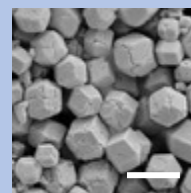
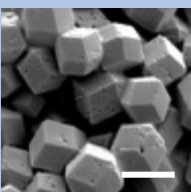
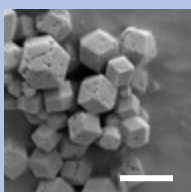
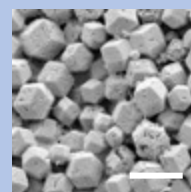
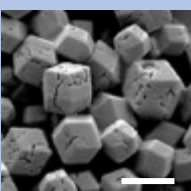
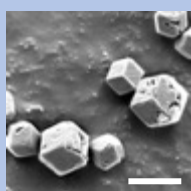
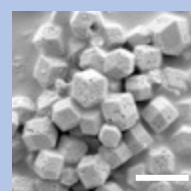
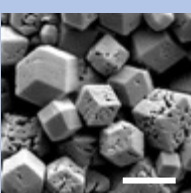
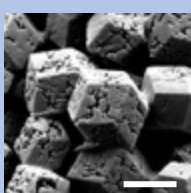
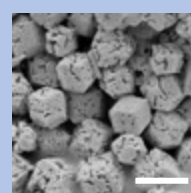
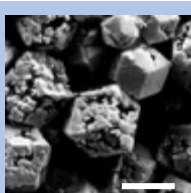
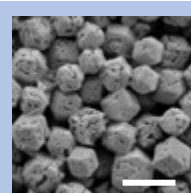
According to these preliminary results, more experiments will be carried out by changing various experimental conditions including the type of irradiation and the duration of irradiation along with other conditions.

## APPENDIX

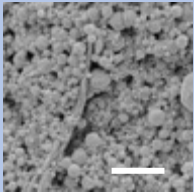
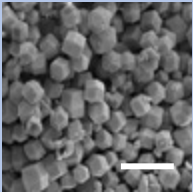
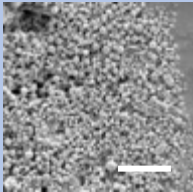
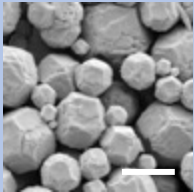
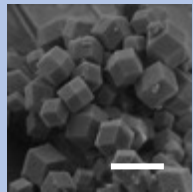
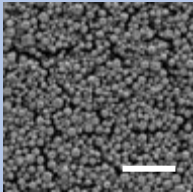
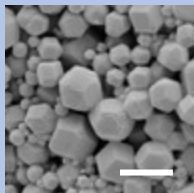
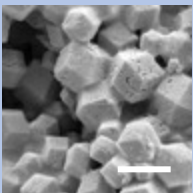
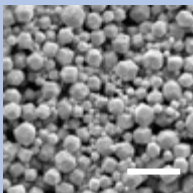
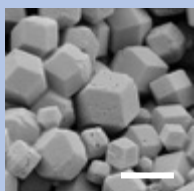
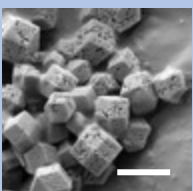
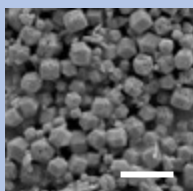
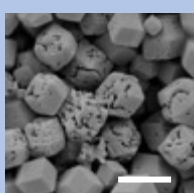
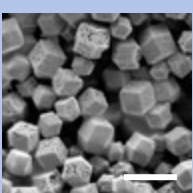
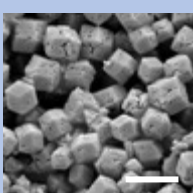
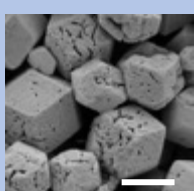
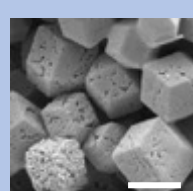
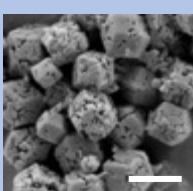
**Table S1:** SEM images showing the growth of ZIF-8 particles at different inner concentrations  $[\text{Zn}^{2+}]$  and outer  $[\text{HmIm}] = 1 \text{ M}$  in consecutive bands (1 % Agar, 25 °C). The scale bar is 1  $\mu\text{m}$ .

$[\text{Zn}^{2+}]$	5 mM	10 mM	20 mM
Band 1			
Band 2			
Band 3			
Band 4			
Band 5			
Band 6			
Band 7			

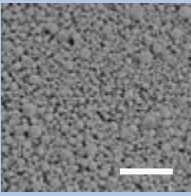
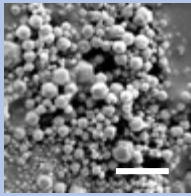
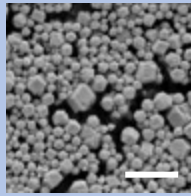
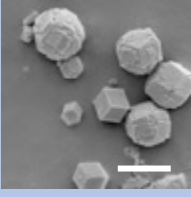
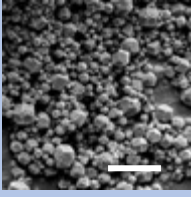
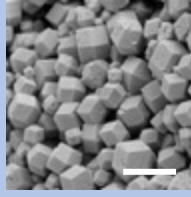
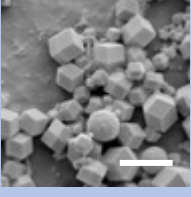
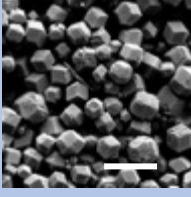
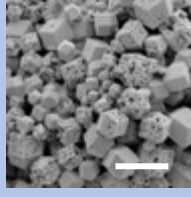
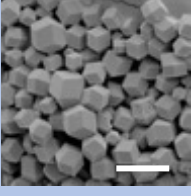
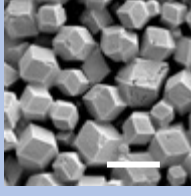
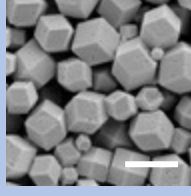
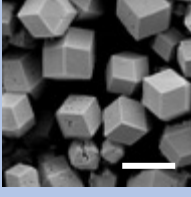
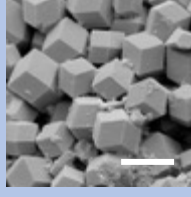
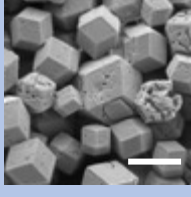
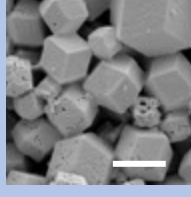
**Table S2:** SEM images showing the growth of ZIF-8 particles at different outer concentrations [HmIm] and inner  $[Zn^{+}] = 20$  mM in consecutive bands (1 % Agar, 25 °C). The scale bar is 2  $\mu$ m.

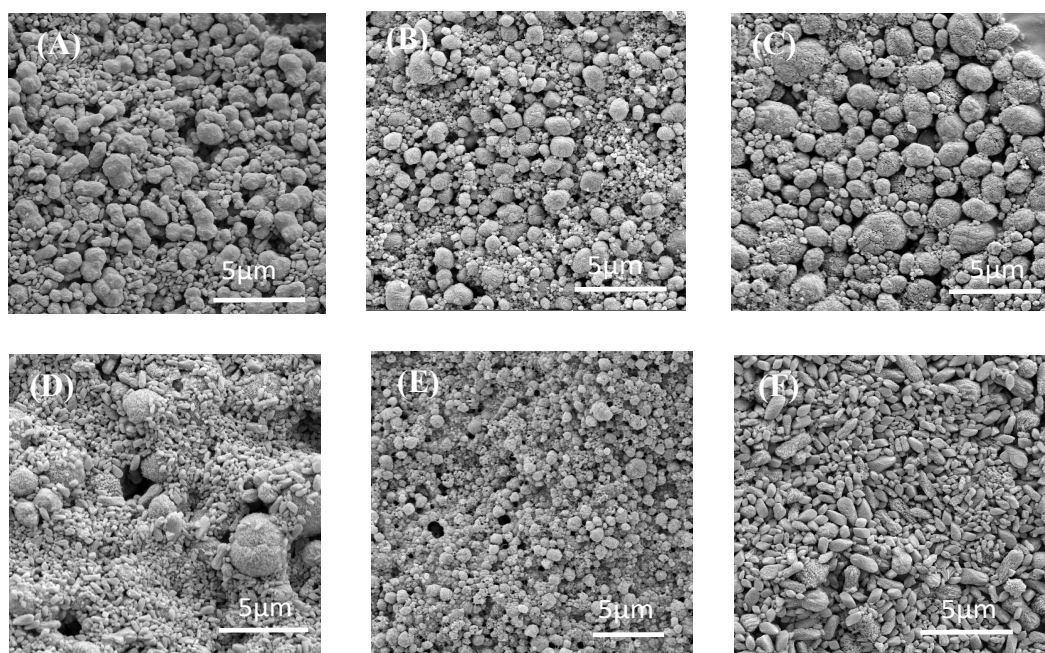
[HmIm]	0.7 M	1 M	2 M
Band 1			
Band 2			
Band 3			
Band 4			
Band 5			
Band 6			
Band 7			

**Table S3:** SEM images showing the growth of ZIF-8 particles at different agar percentages with constant inner and outer concentrations ( $[Zn^{2+}] = 20 \text{ mM}$ ,  $[HmIm] = 2 \text{ M}$ ) at  $25 \text{ }^\circ\text{C}$  in consecutive bands. The scale bar is  $2 \text{ }\mu\text{m}$ .

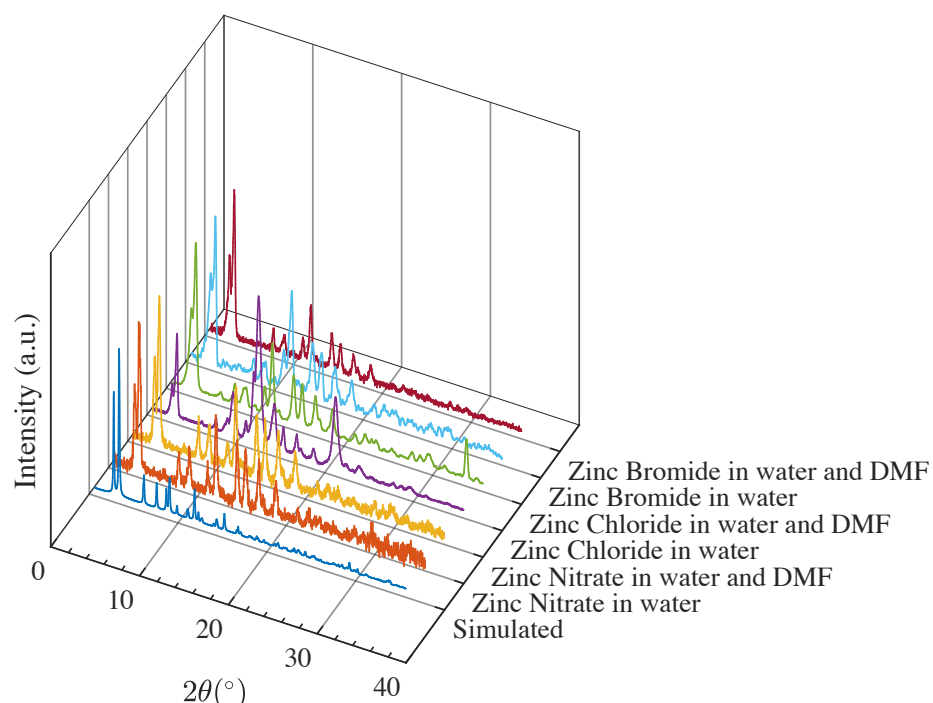
Agar Percentage	0.5 %	1 %	2 %
Band 1			
Band 2			
Band 3			
Band 4			
Band 5			
Band 6			

**Table S4:** SEM images showing the growth of ZIF-8 particles at  $[Zn^{2+}] = 20 \text{ mM}$ ,  $[HmIm] = 1.5 \text{ M}$ , at 1 % agar and different temperatures ( $^{\circ}\text{C}$ ) in consecutive bands. The scale bar is  $2 \mu\text{m}$ .

Temperature	15 $^{\circ}\text{C}$	25 $^{\circ}\text{C}$	30 $^{\circ}\text{C}$
Band 1			
Band 2			
Band 3			
Band 4			
Band 5			
Band 6			

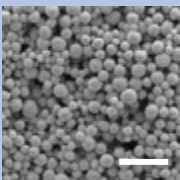
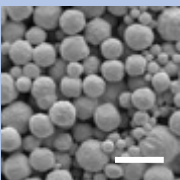
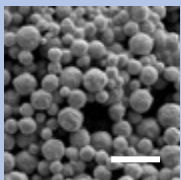
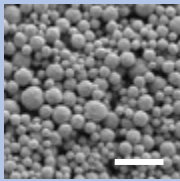
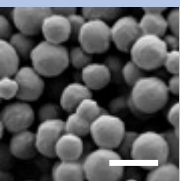
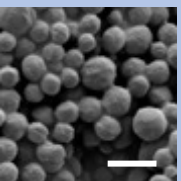
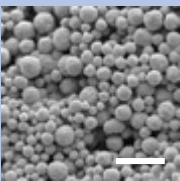
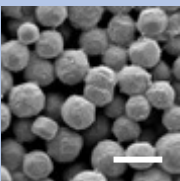
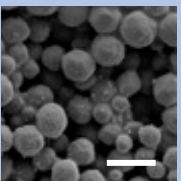
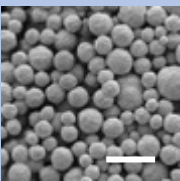
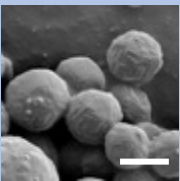
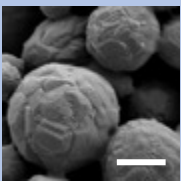
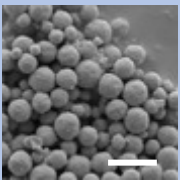

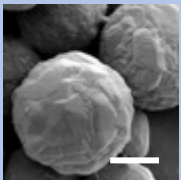
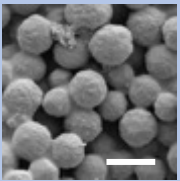
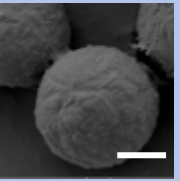
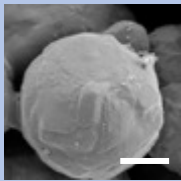
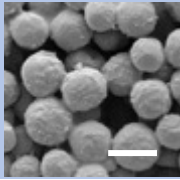
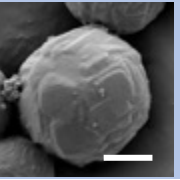
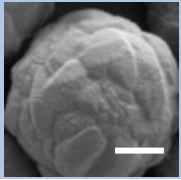


**Figure S1:** SEM images of the synthesized ZIF-7 particles using different zinc sources ((A): zinc nitrate in water, (B): zinc nitrate in a 1:1 ratio of DMF and water, (C): zinc chloride in water, (D): zinc chloride in a 1:1 ratio of DMF and water, (E): zinc bromide in water and (F): zinc bromide in a 1:1 ratio of DMF and water).



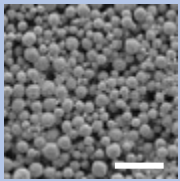
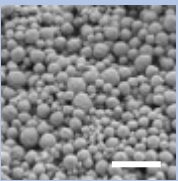
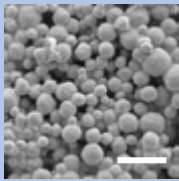
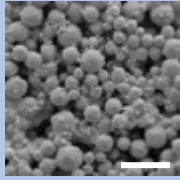
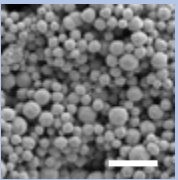
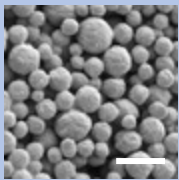
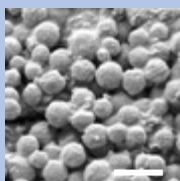
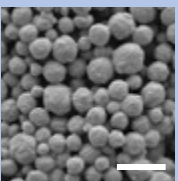
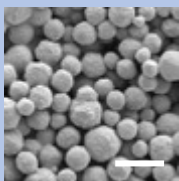
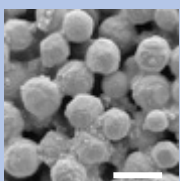
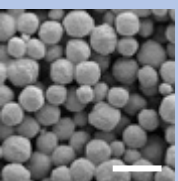
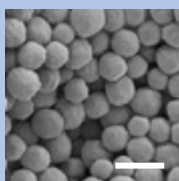
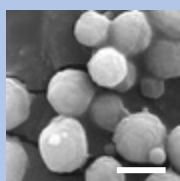
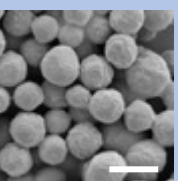
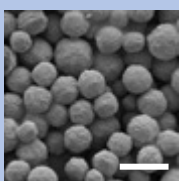
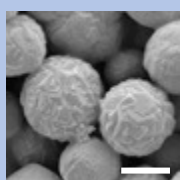
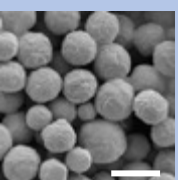
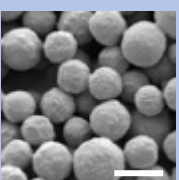
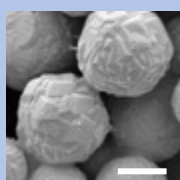
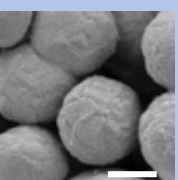
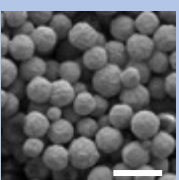
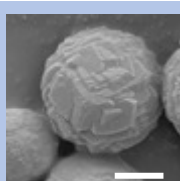
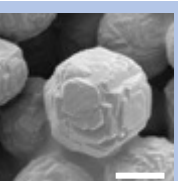
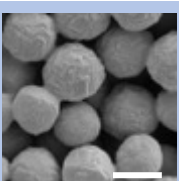
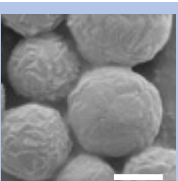
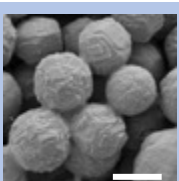
**Figure S2:** PXRD patterns of the synthesized ZIF-7 using different zinc sources.

**Table S5:** SEM images showing the growth of ZIF-7 particles at different inner concentrations  $[\text{Zn}^{2+}]$  and outer  $[\text{BenzIm}] = 0.7 \text{ M}$  in consecutive bands (1 % Agar, 25 °C). The scale bar is 2  $\mu\text{m}$ .

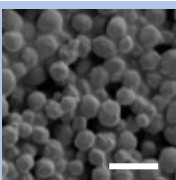
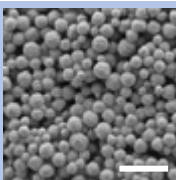
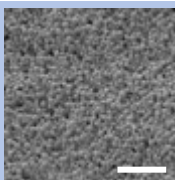
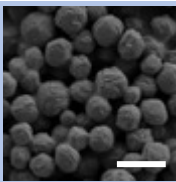
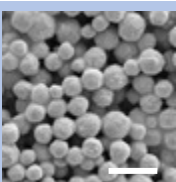
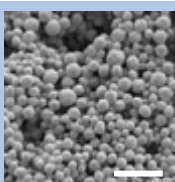
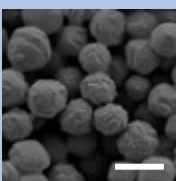
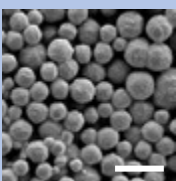
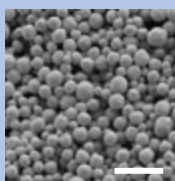
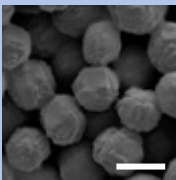
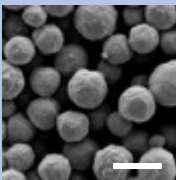
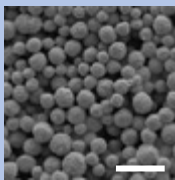
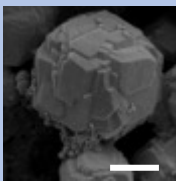
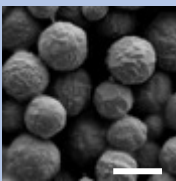
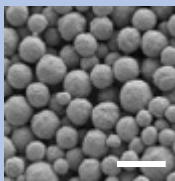
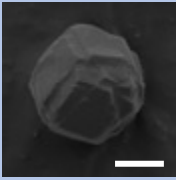
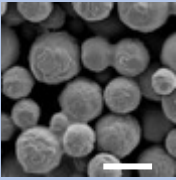
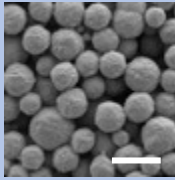
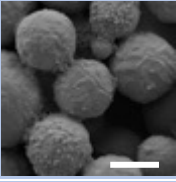
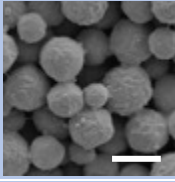
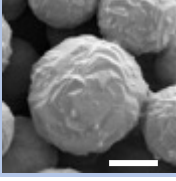
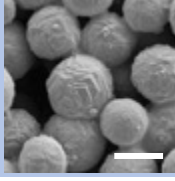
$[\text{Zn}^{2+}]$	10 mM	20 mM	30 mM
Band 1			
Band 2			
Band 3			
Band 4			
Band 5			
Band 6			
Band 7			

**Table S6:** SEM images showing the growth of ZIF-7 particles at different outer concentrations  $[\text{BenzIm}]$  and inner  $[\text{Zn}^{2+}] = 20 \text{ mM}$  in consecutive bands (1 % Agar, 25 °C). The scale bar is 2  $\mu\text{m}$ .

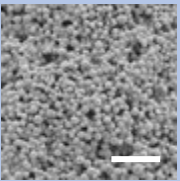
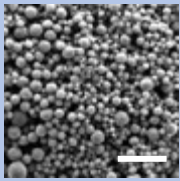
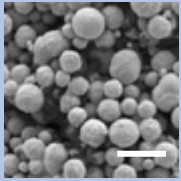
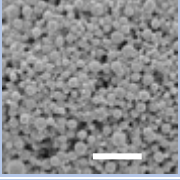
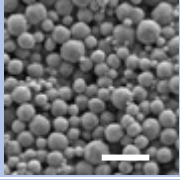
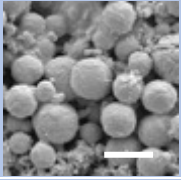
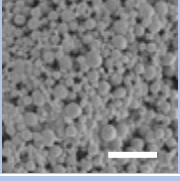
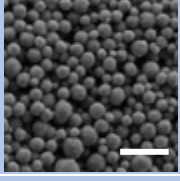

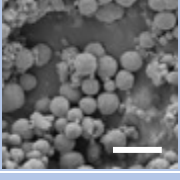
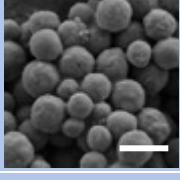
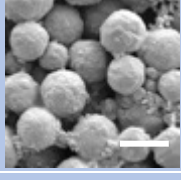
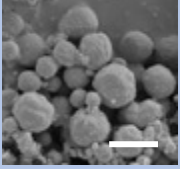
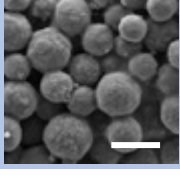
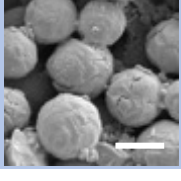


[BenzIm]	0.5 M	0.7 M	1 M
Band 1			
Band 2			
Band 3			
Band 4			
Band 5			
Band 6			
Band 7			
Band 8			
Band 9			

**Table S7:** SEM images showing the growth of ZIF-7 particles at different agar percentages with constant inner and outer concentrations ( $[Zn^{2+}] = 20 \text{ mM}$ ,  $[BenzIm] = 1 \text{ M}$ ) at  $25 \text{ }^\circ\text{C}$  in consecutive bands. The scale bar is  $2 \text{ }\mu\text{m}$

Agar Percentage	0.5 %	1 %	1.5 %
Band 1			
Band 2			
Band 3			
Band 4			
Band 5			
Band 6			
Band 7			
Band 8			

**Table S8:** SEM images showing the growth of ZIF-7 particles at  $[Zn^{2+}] = 20 \text{ mM}$ ,  $[BenzIm] = 1 \text{ M}$ , at 1 % agar and different temperatures ( $^{\circ}\text{C}$ ) in consecutive bands. The scale bar is  $2 \mu\text{m}$ .

Temperature	7 °C	15 °C	25 °C
Band 1			
Band 2			
Band 3			
Band 4			
Band 5			

## REFERENCES

1. Davis, M.E., *Ordered porous materials for emerging applications*. Nature, 2002. **417**(6891): p. 813.
2. Yaghi, O.M., G. Li, and H. Li, *Selective binding and removal of guests in a microporous metal–organic framework*. Nature, 1995. **378**(6558): p. 703.
3. Li, H., et al., *Design and synthesis of an exceptionally stable and highly porous metal-organic framework*. nature, 1999. **402**(6759): p. 276.
4. Férey, G., et al., *Crystallized frameworks with giant pores: are there limits to the possible?* Accounts of chemical research, 2005. **38**(4): p. 217-225.
5. Cheetham, A.K., C. Rao, and R.K. Feller, *Structural diversity and chemical trends in hybrid inorganic–organic framework materials*. Chemical communications, 2006(46): p. 4780-4795.
6. O’Keeffe, M., et al., *The reticular chemistry structure resource (RCSR) database of, and symbols for, crystal nets*. Accounts of chemical research, 2008. **41**(12): p. 1782-1789.
7. Yaghi, O.M., et al., *Reticular synthesis and the design of new materials*. Nature, 2003. **423**(6941): p. 705.
8. Deria, P., et al., *Beyond post-synthesis modification: evolution of metal–organic frameworks via building block replacement*. Chemical Society Reviews, 2014. **43**(16): p. 5896-5912.
9. Furukawa, H., et al., *The chemistry and applications of metal-organic frameworks*. Science, 2013. **341**(6149): p. 1230444.
10. Park, K.S., et al., *Exceptional chemical and thermal stability of zeolitic imidazolate frameworks*. Proceedings of the National Academy of Sciences, 2006. **103**(27): p. 10186-10191.
11. Banerjee, R., et al., *High-throughput synthesis of zeolitic imidazolate frameworks and application to CO<sub>2</sub> capture*. Science, 2008. **319**(5865): p. 939-943.
12. Phan, A., et al., *Synthesis, structure, and carbon dioxide capture properties of zeolitic imidazolate frameworks*. Acc. Chem. Res, 2010. **43**(1): p. 58-67.
13. Chen, B., et al., *Zeolitic imidazolate framework materials: recent progress in synthesis and applications*. Journal of Materials Chemistry A, 2014. **2**(40): p. 16811-16831.
14. Macchioni, A., *Ion pairing in transition-metal organometallic chemistry*. Chemical reviews, 2005. **105**(6): p. 2039-2074.
15. Wang, B., et al., *Colossal cages in zeolitic imidazolate frameworks as selective carbon dioxide reservoirs*. Nature, 2008. **453**(7192): p. 207.
16. Tran, U.P., K.K. Le, and N.T. Phan, *Expanding applications of metal–organic frameworks: zeolite imidazolate framework ZIF-8 as an efficient heterogeneous catalyst for the knoevenagel reaction*. Acs Catalysis, 2011. **1**(2): p. 120-127.

17. Venna, S.R. and M.A. Carreon, *Highly permeable zeolite imidazolate framework-8 membranes for CO<sub>2</sub>/CH<sub>4</sub> separation*. Journal of the American Chemical Society, 2009. **132**(1): p. 76-78.
18. Hayashi, H., et al., *Zeolite A imidazolate frameworks*. Nature materials, 2007. **6**(7): p. 501.
19. Wang, F., et al., *A new approach towards tetrahedral imidazolate frameworks for high and selective CO<sub>2</sub> uptake*. Chemical Communications, 2011. **47**(20): p. 5828-5830.
20. Sun, C.-Y., et al., *Zeolitic imidazolate framework-8 as efficient pH-sensitive drug delivery vehicle*. Dalton Transactions, 2012. **41**(23): p. 6906-6909.
21. Schejn, A., et al., *Cu<sup>2+</sup>-doped zeolitic imidazolate frameworks (ZIF-8): efficient and stable catalysts for cycloadditions and condensation reactions*. Catalysis Science & Technology, 2015. **5**(3): p. 1829-1839.
22. Zaręba, J.K., M. Nyk, and M. Samoć, *Co/ZIF-8 heterometallic nanoparticles: control of nanocrystal size and properties by a mixed-metal approach*. Crystal Growth & Design, 2016. **16**(11): p. 6419-6425.
23. Kaur, G., et al., *Room-temperature synthesis of bimetallic Co–Zn based zeolitic imidazolate frameworks in water for enhanced CO<sub>2</sub> and H<sub>2</sub> uptakes*. Journal of Materials Chemistry A, 2016. **4**(39): p. 14932-14938.
24. Saliba, D., et al., *Crystal Growth of ZIF-8, ZIF-67 and their Mixed Metal Derivatives*. Journal of the American Chemical Society, 2018.
25. Qian, J., F. Sun, and L. Qin, *Hydrothermal synthesis of zeolitic imidazolate framework-67 (ZIF-67) nanocrystals*. Materials Letters, 2012. **82**: p. 220-223.
26. Lee, Y.-R., et al., *ZIF-8: A comparison of synthesis methods*. Chemical Engineering Journal, 2015. **271**: p. 276-280.
27. Gross, A.F., E. Sherman, and J.J. Vajo, *Aqueous room temperature synthesis of cobalt and zinc sodalite zeolitic imidizolate frameworks*. Dalton transactions, 2012. **41**(18): p. 5458-5460.
28. Ban, Y., et al., *Solvothermal synthesis of mixed-ligand metal–organic framework ZIF-78 with controllable size and morphology*. Microporous and Mesoporous Materials, 2013. **173**: p. 29-36.
29. Pan, Y., et al., *Rapid synthesis of zeolitic imidazolate framework-8 (ZIF-8) nanocrystals in an aqueous system*. Chemical communications, 2011. **47**(7): p. 2071-2073.
30. Dharmarathna, S., et al., *Direct sonochemical synthesis of manganese octahedral molecular sieve (OMS-2) nanomaterials using cosolvent systems, their characterization, and catalytic applications*. Chemistry of Materials, 2012. **24**(4): p. 705-712.
31. Suslick, K.S., T. Hyeon, and M. Fang, *Nanostructured materials generated by high-intensity ultrasound: sonochemical synthesis and catalytic studies*. Chemistry of Materials, 1996. **8**(8): p. 2172-2179.
32. Son, W.-J., et al., *Sonochemical synthesis of MOF-5*. Chemical Communications, 2008(47): p. 6336-6338.
33. Seoane, B., et al., *Sonocrystallization of zeolitic imidazolate frameworks (ZIF-7, ZIF-8, ZIF-11 and ZIF-20)*. CrystEngComm, 2012. **14**(9): p. 3103-3107.
34. Cho, H.-Y., et al., *High yield 1-L scale synthesis of ZIF-8 via a sonochemical route*. Microporous and Mesoporous Materials, 2013. **169**: p. 180-184.

35. Fernández-Bertrán, J., et al., *Characterization of mechanochemically synthesized imidazoles of Ag<sup>+</sup> 1, Zn<sup>+</sup> 2, Cd<sup>+</sup> 2, and Hg<sup>+</sup> 2: Solid state reactivity of nd10 cations*. Journal of Physics and Chemistry of Solids, 2006. **67**(8): p. 1612-1617.
36. Klimakow, M., et al., *Mechanochemical synthesis of metal– organic frameworks: a fast and facile approach toward quantitative yields and high specific surface areas*. Chemistry of Materials, 2010. **22**(18): p. 5216-5221.
37. Schlesinger, M., et al., *Evaluation of synthetic methods for microporous metal– organic frameworks exemplified by the competitive formation of [Cu<sub>2</sub> (btc) 3 (H<sub>2</sub>O) 3] and [Cu<sub>2</sub> (btc)(OH)(H<sub>2</sub>O)]*. Microporous and Mesoporous Materials, 2010. **132**(1-2): p. 121-127.
38. Beldon, P.J., et al., *Rapid Room-Temperature Synthesis of Zeolitic Imidazolate Frameworks by Using Mechanochemistry*. Angewandte Chemie International Edition, 2010. **49**(50): p. 9640-9643.
39. Friščić, T., et al., *The role of solvent in mechanochemical and sonochemical cocrystal formation: a solubility-based approach for predicting cocrystallisation outcome*. CrystEngComm, 2009. **11**(3): p. 418-426.
40. Bennett, T.D., et al., *Ball-Milling-Induced Amorphization of Zeolitic Imidazolate Frameworks (ZIFs) for the Irreversible Trapping of Iodine*. Chemistry-A European Journal, 2013. **19**(22): p. 7049-7055.
41. Cao, S., et al., *Amorphization of the prototypical zeolitic imidazolate framework ZIF-8 by ball-milling*. Chemical Communications, 2012. **48**(63): p. 7805-7807.
42. Bennett, T.D., et al., *Facile mechanosynthesis of amorphous zeolitic imidazolate frameworks*. Journal of the American Chemical Society, 2011. **133**(37): p. 14546-14549.
43. Ahmed, I., et al., *Synthesis of a metal–organic framework, iron-benzenetricarboxylate, from dry gels in the absence of acid and salt*. Crystal Growth & Design, 2012. **12**(12): p. 5878-5881.
44. Matsukata, M., et al., *Conversion of dry gel to microporous crystals in gas phase*. Topics in Catalysis, 1999. **9**(1-2): p. 77-92.
45. Goergen, S., et al., *Shape controlled zeolite EU-1 (EUO) catalysts: Dry gel conversion type synthesis, characterization and formation mechanisms*. Microporous and Mesoporous Materials, 2009. **126**(3): p. 283-290.
46. Shi, Q., et al., *Synthesis of ZIF-8 and ZIF-67 by Steam-Assisted Conversion and an Investigation of Their Tribological Behaviors*. Angewandte Chemie International Edition, 2011. **50**(3): p. 672-675.
47. Parnham, E.R. and R.E. Morris, *Ionothermal synthesis of zeolites, metal– organic frameworks, and inorganic–organic hybrids*. Accounts of Chemical Research, 2007. **40**(10): p. 1005-1013.
48. Martins, G.A., et al., *The use of ionic liquids in the synthesis of zinc imidazolate frameworks*. Dalton Transactions, 2010. **39**(7): p. 1758-1762.
49. Yang, L. and H. Lu, *Microwave-assisted Ionothermal Synthesis and Characterization of Zeolitic Imidazolate Framework-8*. Chinese Journal of Chemistry, 2012. **30**(5): p. 1040-1044.
50. Cooper, E.R., et al., *Ionic liquids and eutectic mixtures as solvent and template in synthesis of zeolite analogues*. Nature, 2004. **430**(7003): p. 1012.

51. Letcher, T.M. and N. Deenadayalu, *Ternary liquid–liquid equilibria for mixtures of 1-methyl-3-octyl-imidazolium chloride+ benzene+ an alkane at T= 298.2 K and 1 atm*. The Journal of Chemical Thermodynamics, 2003. **35**(1): p. 67-76.
52. Bhattacharjee, S., et al., *Zeolitic imidazolate frameworks: synthesis, functionalization, and catalytic/adsorption applications*. Catalysis Surveys from Asia, 2014. **18**(4): p. 101-127.
53. Abou-Hassan, A., O. Sandre, and V. Cabuil, *Microfluidics in inorganic chemistry*. Angewandte Chemie International Edition, 2010. **49**(36): p. 6268-6286.
54. Yamamoto, D., et al., *Synthesis and adsorption properties of ZIF-8 nanoparticles using a micromixer*. Chemical engineering journal, 2013. **227**: p. 145-150.
55. Basnayake, S.A., et al., *Carbonate-based zeolitic imidazolate framework for highly selective CO<sub>2</sub> capture*. Inorganic chemistry, 2015. **54**(4): p. 1816-1821.
56. Li, Y., et al., *Synthesis of ZIF-8 and ZIF-67 using mixed-base and their dye adsorption*. Microporous and Mesoporous Materials, 2016. **234**: p. 287-292.
57. Li, Y.S., et al., *Inside cover: Molecular sieve membrane: Supported metal–organic framework with high hydrogen selectivity (Angew. Chem. Int. Ed. 3/2010)*. Angewandte Chemie International Edition, 2010. **49**(3): p. 464-464.
58. Xiang, L., et al., *Amino-Functionalized ZIF-7 Nanocrystals: Improved Intrinsic Separation Ability and Interfacial Compatibility in Mixed-Matrix Membranes for CO<sub>2</sub>/CH<sub>4</sub> Separation*. Advanced Materials, 2017. **29**(32).
59. Yao, J. and H. Wang, *Zeolitic imidazolate framework composite membranes and thin films: synthesis and applications*. Chemical Society Reviews, 2014. **43**(13): p. 4470-4493.
60. Bux, H., et al., *Zeolitic imidazolate framework membrane with molecular sieving properties by microwave-assisted solvothermal synthesis*. Journal of the American Chemical Society, 2009. **131**(44): p. 16000-16001.
61. Pan, Y., et al., *Effective separation of propylene/propane binary mixtures by ZIF-8 membranes*. Journal of membrane science, 2012. **390**: p. 93-98.
62. Pan, Y. and Z. Lai, *Sharp separation of C<sub>2</sub>/C<sub>3</sub> hydrocarbon mixtures by zeolitic imidazolate framework-8 (ZIF-8) membranes synthesized in aqueous solutions*. Chemical Communications, 2011. **47**(37): p. 10275-10277.
63. Liu, D., et al., *Gas transport properties and propylene/propane separation characteristics of ZIF-8 membranes*. Journal of Membrane Science, 2014. **451**: p. 85-93.
64. Hara, N., et al., *Diffusive separation of propylene/propane with ZIF-8 membranes*. Journal of Membrane Science, 2014. **450**: p. 215-223.
65. Li, Y., et al., *Zeolitic imidazolate framework ZIF-7 based molecular sieve membrane for hydrogen separation*. Journal of Membrane Science, 2010. **354**(1-2): p. 48-54.
66. Cacho-Bailo, F., et al., *ZIF-8 continuous membrane on porous polysulfone for hydrogen separation*. Journal of Membrane Science, 2014. **464**: p. 119-126.
67. Tao, K., C. Kong, and L. Chen, *High performance ZIF-8 molecular sieve membrane on hollow ceramic fiber via crystallizing-rubbing seed deposition*. Chemical engineering journal, 2013. **220**: p. 1-5.

68. Dong, X., et al., *Synthesis of zeolitic imidazolate framework-78 molecular-sieve membrane: defect formation and elimination*. Journal of Materials Chemistry, 2012. **22**(36): p. 19222-19227.
69. Zhang, C., et al., *A hybrid zeolitic imidazolate framework membrane by mixed-linker synthesis for efficient CO<sub>2</sub> capture*. Chemical Communications, 2013. **49**(6): p. 600-602.
70. Liu, Y., et al., *Synthesis and characterization of ZIF-69 membranes and separation for CO<sub>2</sub>/CO mixture*. Journal of Membrane Science, 2010. **353**(1-2): p. 36-40.
71. Huang, A., et al., *A highly permeable and selective zeolitic imidazolate framework ZIF-95 membrane for H<sub>2</sub>/CO<sub>2</sub> separation*. Chemical Communications, 2012. **48**(89): p. 10981-10983.
72. Li, J., et al., *Zeolitic imidazolate framework-8 with high efficiency in trace arsenate adsorption and removal from water*. The Journal of Physical Chemistry C, 2014. **118**(47): p. 27382-27387.
73. Jian, M., et al., *Adsorptive removal of arsenic from aqueous solution by zeolitic imidazolate framework-8 (ZIF-8) nanoparticles*. Colloids and Surfaces A: Physicochemical and Engineering Aspects, 2015. **465**: p. 67-76.
74. Jung, B.K., et al., *Adsorptive removal of p-arsanilic acid from water using mesoporous zeolitic imidazolate framework-8*. Chemical Engineering Journal, 2015. **267**: p. 9-15.
75. Shahrak, M.N., M. Ghahramaninezhad, and M. Eydifarash, *Zeolitic imidazolate framework-8 for efficient adsorption and removal of Cr (VI) ions from aqueous solution*. Environmental Science and Pollution Research, 2017. **24**(10): p. 9624-9634.
76. Lin, K.-Y.A. and H.-A. Chang, *Efficient adsorptive removal of humic acid from water using zeolitic imidazole framework-8 (ZIF-8)*. Water, Air, & Soil Pollution, 2015. **226**(2): p. 10.
77. Khan, N.A., et al., *Adsorption and removal of phthalic acid and diethyl phthalate from water with zeolitic imidazolate and metal-organic frameworks*. Journal of hazardous materials, 2015. **282**: p. 194-200.
78. Yan, X., et al., *Surfactant-assisted synthesis of ZIF-8 nanocrystals for phthalic acid adsorption*. Journal of Sol-Gel Science and Technology, 2016. **80**(2): p. 523-530.
79. Jiang, J.-Q., C.-X. Yang, and X.-P. Yan, *Zeolitic imidazolate framework-8 for fast adsorption and removal of benzotriazoles from aqueous solution*. ACS applied materials & interfaces, 2013. **5**(19): p. 9837-9842.
80. Feng, Y., et al., *Fast adsorption of methyl blue on zeolitic imidazolate framework-8 and its adsorption mechanism*. RSC Advances, 2016. **6**(111): p. 109608-109612.
81. Thi Thanh, M., et al., *Synthesis of iron doped zeolite imidazolate framework-8 and its remazol deep black RGB dye adsorption ability*. Journal of Chemistry, 2017. **2017**.
82. Abdi, J., et al., *Synthesis of amine-modified zeolitic imidazolate framework-8, ultrasound-assisted dye removal and modeling*. Ultrasonics sonochemistry, 2017. **39**: p. 550-564.
83. Tanabe, K. and W.F. Hölderich, *Industrial application of solid acid-base catalysts*. Applied Catalysis A: General, 1999. **181**(2): p. 399-434.



84. Thallapally, P.K., et al., *Micro and mesoporous metal–organic frameworks for catalysis applications*. Dalton Transactions, 2010. **39**(7): p. 1692-1694.
85. Chizallet, C., et al., *Catalysis of transesterification by a nonfunctionalized metal–organic framework: acido-basicity at the external surface of ZIF-8 probed by FTIR and ab initio calculations*. Journal of the American Chemical Society, 2010. **132**(35): p. 12365-12377.
86. Nguyen, L.T., et al., *Metal–organic frameworks for catalysis: the Knoevenagel reaction using zeolite imidazolate framework ZIF-9 as an efficient heterogeneous catalyst*. Catalysis Science & Technology, 2012. **2**(3): p. 521-528.
87. Ammar, M., S. Jiang, and S. Ji, *Heteropoly acid encapsulated into zeolite imidazolate framework (ZIF-67) cage as an efficient heterogeneous catalyst for Friedel–Crafts acylation*. Journal of Solid State Chemistry, 2016. **233**: p. 303-310.
88. Nguyen, L.T., K.L. Ky, and T. Nam, *A zeolite imidazolate framework ZIF-8 catalyst for Friedel–Crafts acylation*. Chinese Journal of Catalysis, 2012. **33**(4-6): p. 688-696.
89. Wee, L.H., et al., *Hierarchical Zeolitic Imidazolate Framework-8 Catalyst for Monoglyceride Synthesis*. ChemCatChem, 2013. **5**(12): p. 3562-3566.
90. Kuruppathparambil, R.R., et al., *A room temperature synthesizable and environmental friendly heterogeneous ZIF-67 catalyst for the solvent less and co-catalyst free synthesis of cyclic carbonates*. Applied Catalysis B: Environmental, 2016. **182**: p. 562-569.
91. Hwang, G.-Y., et al., *A highly efficient zeolitic imidazolate framework catalyst for the co-catalyst and solvent free synthesis of cyclic carbonates from CO<sub>2</sub>*. Journal of CO<sub>2</sub> Utilization, 2016. **15**: p. 123-130.
92. Zhang, A., et al., *Epoxidation of olefins with O<sub>2</sub> and isobutyraldehyde catalyzed by cobalt (II)-containing zeolitic imidazolate framework material*. Catalysis Communications, 2011. **12**(13): p. 1183-1187.
93. i Xamena, F.L., et al., *Metal organic frameworks (MOFs) as catalysts: A combination of Cu<sup>2+</sup> and Co<sup>2+</sup> MOFs as an efficient catalyst for tetralin oxidation*. Journal of Catalysis, 2008. **255**(2): p. 220-227.
94. Zakzeski, J., et al., *Catalytic oxidation of aromatic oxygenates by the heterogeneous catalyst Co-ZIF-9*. Applied Catalysis A: General, 2011. **394**(1-2): p. 79-85.
95. Li, Q. and H. Kim, *Hydrogen production from NaBH<sub>4</sub> hydrolysis via Co-ZIF-9 catalyst*. Fuel processing technology, 2012. **100**: p. 43-48.
96. Lu, G. and J.T. Hupp, *Metal–organic frameworks as sensors: a ZIF-8 based Fabry–Pérot device as a selective sensor for chemical vapors and gases*. Journal of the American Chemical Society, 2010. **132**(23): p. 7832-7833.
97. Liu, S., et al., *Zeolitic imidazolate framework-8 as a luminescent material for the sensing of metal ions and small molecules*. Journal of Materials Chemistry, 2011. **21**(18): p. 6649-6653.
98. Liu, S., et al., *Application of Zeolitic Imidazolate Framework-8 Nanoparticles for the Fluorescence-Enhanced Detection of Nucleic Acids*. ChemPlusChem, 2012. **77**(1): p. 23-26.

99. Ma, W., et al., *Zeolitic imidazolate framework-based electrochemical biosensor for in vivo electrochemical measurements*. Analytical chemistry, 2013. **85**(15): p. 7550-7557.
100. Zhan, W.-w., et al., *Semiconductor@ metal-organic framework core-shell heterostructures: a case of ZnO@ ZIF-8 nanorods with selective photoelectrochemical response*. Journal of the American Chemical Society, 2013. **135**(5): p. 1926-1933.
101. Eslava, S., et al., *Metal-organic framework ZIF-8 films as low- $\kappa$  dielectrics in microelectronics*. Chemistry of Materials, 2012. **25**(1): p. 27-33.
102. Zhuang, J., et al., *Optimized metal-organic-framework nanospheres for drug delivery: evaluation of small-molecule encapsulation*. ACS nano, 2014. **8**(3): p. 2812-2819.
103. He, L., et al., *Carbon nanodots@ zeolitic imidazolate framework-8 nanoparticles for simultaneous pH-responsive drug delivery and fluorescence imaging*. CrystEngComm, 2014. **16**(16): p. 3259-3263.
104. Ren, H., et al., *Polyacrylic acid@ zeolitic imidazolate framework-8 nanoparticles with ultrahigh drug loading capability for pH-sensitive drug release*. Chemical Communications, 2014. **50**(8): p. 1000-1002.
105. Liédana, N., et al., *CAF@ ZIF-8: one-step encapsulation of caffeine in MOF*. ACS applied materials & interfaces, 2012. **4**(9): p. 5016-5021.
106. Donnelly, R.J., R. Herman, and I. Prigogine. *Non-equilibrium thermodynamics; Variational Techniques and Stability*. in *Non-Equilibrium Thermodynamics, Variational Techniques, and Stability*. 1966.
107. Grzybowski, B.A., *Chemistry in motion: reaction-diffusion systems for micro- and nanotechnology*. 2009: John Wiley & Sons.
108. Liesegang, R., *Chemical Reactions in Gels*. Liesegang, Dusseldorf, 1898.
109. Liesegang, R., *Lieseg. Photograph. ArchiV*. 1986. **37**: p. 321-326.
110. Badr, L. and R. Sultan, *Ring morphology and pH effects in 2D and 1D Co (OH) 2 Liesegang systems*. The Journal of Physical Chemistry A, 2009. **113**(24): p. 6581-6586.
111. Karam, T., H. El-Rassy, and R. Sultan, *Mechanism of revert spacing in a PbCrO4 Liesegang system*. The Journal of Physical Chemistry A, 2011. **115**(14): p. 2994-2998.
112. Kanniah, N., et al., *Revert and direct type Liesegang phenomenon of silver iodide*. Journal of Colloid and Interface Science, 1981. **80**(2): p. 369-376.
113. Smoukov, S.K., I. Lagzi, and B.A. Grzybowski, *Independence of primary and secondary structures in periodic precipitation patterns*. The Journal of Physical Chemistry Letters, 2011. **2**(4): p. 345-349.
114. Mandalian, L. and R. Sultan, *Fractal structures in PbF 2/Pb (NO 3) 2 precipitate systems*. Collection of Czechoslovak chemical communications, 2002. **67**(12): p. 1729-1742.
115. Dayeh, M., M. Ammar, and M. Al-Ghoul, *Transition from rings to spots in a precipitation reaction-diffusion system*. RSC Advances, 2014. **4**(104): p. 60034-60038.
116. Al-Ghoul, M., R. Issa, and M. Hmadeh, *Synthesis, size and structural evolution of metal-organic framework-199 via a reaction-diffusion process at room temperature*. CrystEngComm, 2017. **19**(4): p. 608-612.

117. Al Akhrass, G.A., et al., *Self-assembled lanthanum hydroxide microspheres within a reaction–diffusion framework: Synthesis, characterization, control and application*. RSC Advances, 2016. **6**(5): p. 3433-3439.
118. Prager, S., *Periodic precipitation*. The Journal of Chemical Physics, 1956. **25**(2): p. 279-283.
119. Dee, G., *The patterns produced by precipitation at a moving reaction front*. Physica D: Nonlinear Phenomena, 1986. **23**(1-3): p. 340-344.
120. Sultan, R., et al., *Bifurcation of the Ostwald-Liesegang supersaturation-nucleation-depletion cycle*. Earth-Science Reviews, 1990. **29**(1-4): p. 163-173.
121. Smith, D., *On Ostwald's supersaturation theory of rhythmic precipitation (Liesegang's rings)*. The Journal of chemical physics, 1984. **81**(7): p. 3102-3115.
122. Sultan, R. and P. Ortoleva, *Periodic and aperiodic macroscopic patterning in two precipitate post-nucleation systems*. Physica D: Nonlinear Phenomena, 1993. **63**(1-2): p. 202-212.
123. Antal, T., et al., *Derivation of the Matalon-Packter law for Liesegang patterns*. The Journal of chemical physics, 1998. **109**(21): p. 9479-9486.
124. Wagner, C., *Mathematical analysis of the formation of periodic precipitations*. Journal of Colloid Science, 1950. **5**(1): p. 85-97.
125. Flicker, M. and J. Ross, *Mechanism of chemical instability for periodic precipitation phenomena*. The Journal of Chemical Physics, 1974. **60**(9): p. 3458-3465.
126. Mueller, S.C., S. Kai, and J. Ross, *Periodic precipitation patterns in the presence of concentration gradients. I. Dependence on ion product and concentration difference*. The Journal of Physical Chemistry, 1982. **86**(20): p. 4078-4087.
127. Feinn, D., et al., *Spontaneous pattern formation in precipitating systems*. The Journal of Chemical Physics, 1978. **69**(1): p. 27-39.
128. Kai, S., S.C. Müller, and J. Ross, *Measurements of temporal and spatial sequences of events in periodic precipitation processes*. The Journal of Chemical Physics, 1982. **76**(3): p. 1392-1406.
129. Hedges, E.S. and R.V. Henley, *CCCLX.—The formation of liesegang rings as a periodic coagulation phenomenon*. Journal of the Chemical Society (Resumed), 1928: p. 2714-2726.
130. Al-Ghoul, M., M. Ammar, and R.O. Al-Kaysi, *Band propagation, scaling laws and phase transition in a precipitate system. I: Experimental study*. The Journal of Physical Chemistry A, 2012. **116**(18): p. 4427-4437.
131. Jablczynski, K., *La formation rythmique des précipités. Les anneaux de Liesegang*. Bull. Soc. Chim. France, 1923. **33**.
132. Müller, S.C., S. Kai, and J. Ross, *Curiosities in periodic precipitation patterns*. Science, 1982. **216**(4546): p. 635-637.
133. Droz, M., J. Magnin, and M. Zrinyi, *Liesegang patterns: Studies on the width law*. The Journal of chemical physics, 1999. **110**(19): p. 9618-9622.
134. Droz, M., *Recent theoretical developments on the formation of Liesegang patterns*. Journal of Statistical Physics, 2000. **101**(1-2): p. 509-519.
135. George, J., et al., *Rhythmic pattern formations in gels and Matalon—Packter law: A fresh perspective*. Pramana, 2003. **60**(6): p. 1259-1271.

136. Rahbani, J., et al., *Characterization of internal structure of hydrated agar and gelatin matrices by cryo-SEM*. Electrophoresis, 2013. **34**(3): p. 405-408.
137. Zhang, J., et al., *Transition from ZIF-L-Co to ZIF-67: a new insight into the structural evolution of zeolitic imidazolate frameworks (ZIFs) in aqueous systems*. CrystEngComm, 2015. **17**(43): p. 8212-8215.
138. Li, Y.S., et al., *Controllable synthesis of metal–organic frameworks: From MOF nanorods to oriented MOF membranes*. Advanced Materials, 2010. **22**(30): p. 3322-3326.
139. Du, Y., et al., *New high-and low-temperature phase changes of ZIF-7: elucidation and prediction of the thermodynamics of transitions*. Journal of the American Chemical Society, 2015. **137**(42): p. 13603-13611.
140. Perez, E.V., et al., *Origins and evolution of inorganic-based and MOF-based mixed-matrix membranes for gas separations*. Processes, 2016. **4**(3): p. 32.
141. Xie, J., et al., *CO<sub>2</sub> adsorption performance of ZIF-7 and its endurance in flue gas components*. Frontiers of Environmental Science & Engineering, 2014. **8**(2): p. 162-168.
142. Cai, W., et al., *Thermal structural transitions and carbon dioxide adsorption properties of zeolitic imidazolate framework-7 (ZIF-7)*. Journal of the American Chemical Society, 2014. **136**(22): p. 7961-7971.
143. Thompson, J.A., et al., *Hybrid zeolitic imidazolate frameworks: controlling framework porosity and functionality by mixed-linker synthesis*. Chemistry of Materials, 2012. **24**(10): p. 1930-1936.
144. Singh, A.K., S. Singh, and A. Kumar, *Hydrogen energy future with formic acid: a renewable chemical hydrogen storage system*. Catalysis Science & Technology, 2016. **6**(1): p. 12-40.
145. Johnson, T.C., D.J. Morris, and M. Wills, *Hydrogen generation from formic acid and alcohols using homogeneous catalysts*. Chemical Society Reviews, 2010. **39**(1): p. 81-88.